Precipitation Behavior of Magnesium Alloys Containing Neodymium and Yttrium

by

Ellen L.S. Solomon

A dissertation submitted in partial fulfillment
of the requirements for the degree of
Doctor of Philosophy
(Materials Science and Engineering)
in the University of Michigan
2017

Doctoral Committee:

Associate Professor Emmanuelle Marquis, Chair
Professor Amit Misra
Associate Professor Veera Sundararaghavan
Assistant Professor Liang Qi

Ellen L.S. Solomon

esitz@umich.edu

ORCID iD: 0000-0001-8426-9653

ACKNOWLEDGEMENTS

I would like to express my appreciation to many great individuals who supported and encouraged me over the past five years. First, I want to thank my advisor, Dr. Emmanuelle Marquis, for being an exceptional mentor, colleague, and friend. Her expert guidance has made this an exciting and rewarding experience. I would also like to thank my dissertation committee members, Professor Amit Misra, Professor Liang Qi, and Professor Veera Sundararaghavan for providing valuable advice and support for completing my dissertation. In addition, Professor John Allison shared in many thought-provoking discussions that helped me shape my research.

I am sincerely grateful to all of the staff at the Michigan Center for Materials Characterization for their eagerness to help me with various aspects of data collection and analysis. I would like to especially thank Dr. Kai Sun for his time and patience in teaching me TEM. This work would not have been possible without his assistance.

Many thanks go to my former and current lab mates at the University of Michigan. Many times I came to them for technical advice. I especially want to thank Vicente Araullo-Peters for his contributions and for teaching me APT sample preparation techniques.

Lastly, I would like to thank my friends and family, especially my husband John and my mom and dad. I am forever grateful for their endless support and positive encouragement throughout this journey. My success would not have been possible without their support.

TABLE OF CONTENTS

LIST OF TABLES

LIST OF FIGURES

LIST OF APPENDICES

LIST OF ABBREVIATIONS AND ACRONYMS

APT: Atom probe tomography

HAADF: High-angle annular dark-field

STEM: Scanning transmission electron microscopy

TEM: Transmission electron microscopy

HREM: High-resolution electron microscopy

SEM: Scanning electron microscopy

BF: Bright field

EBSD: Electron backscatter diffraction

EELS: Electron energy loss spectroscopy

FIB: Focused ion beam

ICP-MS: Inductively coupled plasma mass spectrometry

IVAS Integrated visualization and analysis software

DFT: Density functional theory

DSC: Differential scanning calorimetry

HPT: High pressure torsion

RE: Rare earth

GP zones: Guinier-Preston zones

HCP: Hexagonal close-packed

FCC: Face-centered cubic

BCT: Body-centered tetragonal

XRD: X-ray diffraction

EPMA: Electron probe micro-analysis

SSSS: Super-saturated solid solution

EDM: Electrical discharge machining

PRISMS: PRedicticve Integrated Structural Materials Science

ICME: Integrated Computational Materials Engineering

ABSTRACT

Magnesium is the lightest of the structural metals and has great potential for reducing the weight of transportation systems, which in turn reduces harmful emissions and improves fuel economy. Due to the inherent softness of Mg, other elements are typically added in order to form a fine distribution of precipitates during aging, which improves the strength by acting as barriers to moving dislocations. Mg-RE alloys are unique among other Mg alloys because they form precipitates that lie parallel to the prismatic planes of the Mg matrix, which is an ideal orientation to hinder dislocation slip. However, RE elements are expensive and impractical for many commercial applications, motivating the rapid design of alternative alloy compositions with comparable mechanical properties. Yet in order to design new alloys reproducing some of the beneficial properties of Mg-RE alloys, we must first fully understand precipitation in these systems. Therefore, the main objectives of this thesis are to identify the roles of specific RE elements (Nd and Y) on precipitation and to relate the precipitate microstructure to the alloy strength.

The alloys investigated in this thesis are the Mg-Nd, Mg-Y, and Mg-Y-Nd systems, which contain the main alloying elements of commercial WE series alloys (Y and Nd). In all three alloy systems, a sequence of metastable phases forms upon aging. Precipitate composition, atomic structure, morphology, and spatial distribution are strongly controlled by the elastic strain energy originating from the misfitting coherent precipitates. The dominating role that strain

energy plays in these alloy systems gives rise to very unique microstructures. The evolution of the hardness and precipitate microstructure with aging revealed that metastable phases are the primary strengthening phases of these alloys, and interact with dislocations by shearing. Our understanding of precipitation mechanisms and commonalities among the Mg-RE alloys provide future avenues to apply more efficient and targeted alloy design.

CHAPTER 1:

Introduction

1.1 Motivation and background

The need to develop lightweight materials for reducing the weight of transportation systems has motivated industrial research on magnesium alloys. However, state-of-the-art research on Mg alloys is relatively immature compared to other metals, such as aluminum or nickel alloys. In particular, our fundamental understanding of the physical metallurgy principles relevant to Mg alloys are not sufficiently developed to enable rapid alloy design required to implement these materials in modern vehicles.

Mg is an inherently soft material and in order to be used as a structural material, it needs to be strengthened. One common way to strengthen alloys is by precipitation hardening, which is an especially effective strengthening method for Mg alloys containing rare earth (RE) elements. RE elements have relatively high solubility in Mg in high temperatures allowing a fine distribution of metastable precipitates upon aging at lower temperatures. These precipitates are unique because their habit planes lie parallel to the prismatic planes of the Mg matrix, which is much more effective in impeding dislocation motion than precipitates lying parallel to the basal plane [1]. However, RE elements are costly, limiting the use of these materials in a broad range of applications. Understanding what makes RE-based precipitation unique and applying this knowledge to the design of less expensive alloys with fewer or no rare earth elements is a

relevant and timely challenge. A significant amount of research on Mg-RE alloys has focused on the precipitation sequence in complex alloys such as WE43 and WE54 [2-13]. However, these alloys contain many different alloying elements that make it difficult to fully understand the role of each alloying element on precipitation. Quantitative analysis of the precipitation processes in simpler alloys containing only one or two of the major alloying elements of WE43 is a more meaningful approach to identifying the effect of alloy composition on the precipitation mechanisms and kinetics as well as the precipitate size, structure, and morphology.

The important questions that this thesis addresses are the following:

1. What are the precipitation mechanisms (including nucleation paths for β''', β', and β_1 in Mg-Nd, Mg-Y, Mg-Nd-Y, and WE43)?
2. What controls precipitate shapes and evolution in Mg-Nd, Mg-Y, Mg-Nd-Y, and WE43?
3. What are the roles of Nd and Y in the precipitation process?
4. What is the relationship between the precipitate microstructure and hardness? And what are the strengthening mechanisms of the β''' and β' phases?

The results from this work contribute to our fundamental understanding of the chemical and microstructural factors important in controlling precipitation in Mg-RE alloys and contribute to the development of computational tools for predicting material behavior. This work was performed as part of the PRedictive Integrated Structural Materials Science Center (PRISMS Center), which involves collaboration between several experimental and computational research groups implementing Integrated Computational Materials Engineering (ICME) principles for rapidly designing new alloys. Experimental quantification and observation are necessary for developing reliable and quantitative models which predict the actual material behavior.

1.2 Thesis structure

The dissertation is broken up into seven main chapters. Following the introduction is Chapter 2 that provides a review of the literature on precipitation in Mg-RE alloys containing Nd and Y and highlights current knowledge gaps. Chapter 3 investigates the evolution of the early stage precipitates in Mg-Nd while Chapter 4 examines the precipitation behavior in the Mg-Y system. The strengthening mechanisms of the β''' phase in Mg-Nd and β' phase in Mg-Y are discussed in Chapter 5. Chapter 6 covers the aging behavior of the ternary Mg-Y-Nd and WE43 alloys and discusses the relationship between the phases in these alloys and the binary Mg-Nd and Mg-Y alloys. The conclusions and summary of the work are provided in Chapter 7 in addition to suggestions for future work.

CHAPTER 2:

Precipitation in Mg-Rare Earth Alloys: Literature Review

This chapter reviews the literature on precipitation in Mg-Nd, Mg-Y, and Mg-Y-Nd alloys. The phase diagrams for each system are presented and each of the precipitate phases that form in these alloys are reviewed individually and are related to the reported hardness curves. Other relevant topics such as the effect of external stress and processing on precipitation as well as the precipitate strengthening mechanisms and the presence of stacking faults are discussed for certain alloy systems. Other alloys such as Mg-Gd, Mg-Dy, etc., which experience similar precipitation behavior to the alloys examined in this chapter, will not be discussed but details can be found in Refs. [14-18].

2.1 Mg-Nd alloys

2.1.1 Phase diagram

The most recent Mg-Nd phase diagram is shown in **Figure 1**. The phase diagram includes five binary intermetallic compounds: $MgNd$, Mg_2Nd, Mg_3Nd, $Mg_{41}Nd_5$, and the metastable compound $Mg_{12}Nd$ (**Figure 1a**). The β_e ($Mg_{41}Nd_5$) phase is near the Mg-rich side of the phase diagram and is involved in two reactions, a peritectic decomposition into the liquid and Mg_3Nd phases at 558°C and a eutectic reaction with the Mg-rich solid solution and the liquid phase at 548°C [19]. According to the current phase diagram (**Figure 1**), the maximum solubility at 548

4

°C is about 4.6 wt. % Nd and rapidly decreases with decreasing temperature, making precipitation hardening an important strengthening mechanism in Mg-Nd alloys. During aging of a supersaturated solid solution of Nd in Mg however, a succession of the metastable phases that do not appear on this equilibrium phase diagram is observed: solute clusters, GP zones/$D0_{19}$ β'' (Mg_3Nd), orthorhombic β' (Mg_7Nd), fcc β_1 (Mg_3Nd), tetragonal β ($Mg_{12}Nd$), and tetragonal β_e ($Mg_{41}Nd_5$) [2, 20-22]. The structural and morphological details of each phase are reviewed in the following few sections.
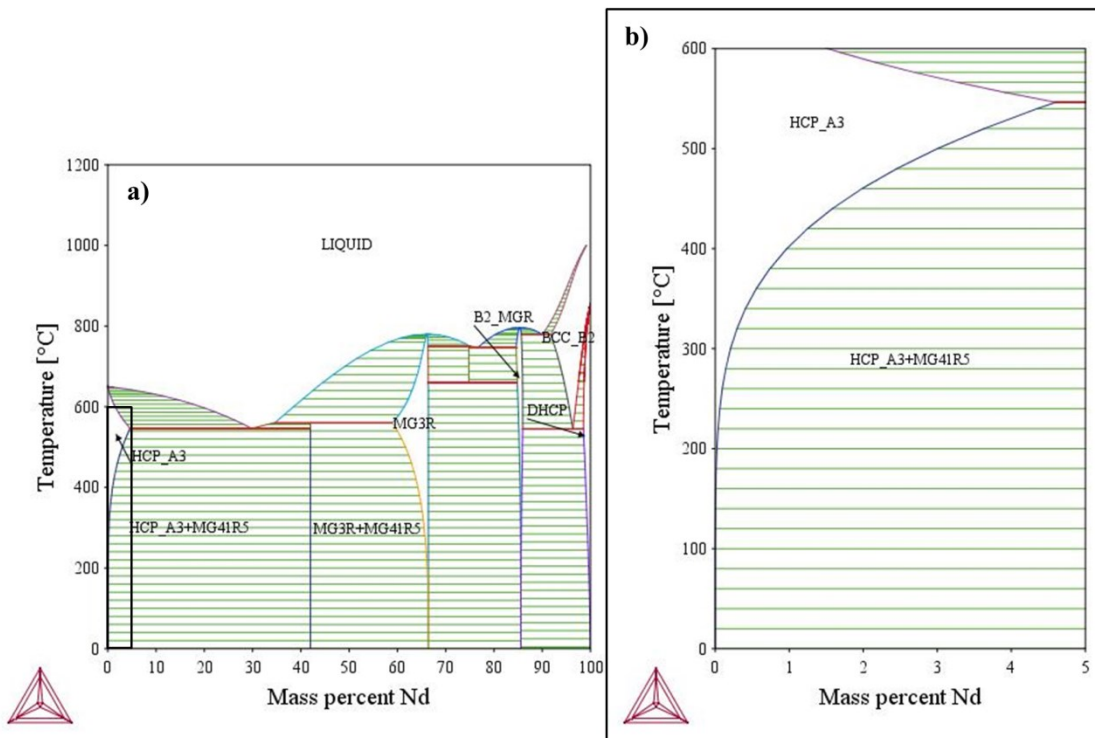
Figure 1: a) & b) Binary Mg-Nd phase diagram. b) Magnified view of the Mg-rich side of the phase diagram [23].

2.1.2 Solute clusters and GP zones (β" phase)

During aging, solute clusters and GP zones have been reported as the first phases in the precipitation sequence for Mg-Nd alloys. The solute clusters are irregular, short-ranged ordered structures that contain Nd-rich columns arranged on Mg lattice sites [24]. With longer aging,

5

these solute clusters are gradually replaced by GP zones. Until more recently, the presence of GP zones in Mg-Nd have only been observed from diffraction patterns and were reported to have a $D0_{19}$ structure [2, 20]. Later, high resolution STEM imaging revealed GP zones forming as thin plates on prismatic $\{10\bar{1}0\}_{Mg}$ planes and containing Nd-rich columns arranged on the Mg lattice sites in the form of different triangular shaped patterns [22, 24], as shown schematically in **Figure 2**. Although GP zones having a short-range ordered structure are observed, it remains unclear whether the $D0_{19}$ structure exists in these alloys.
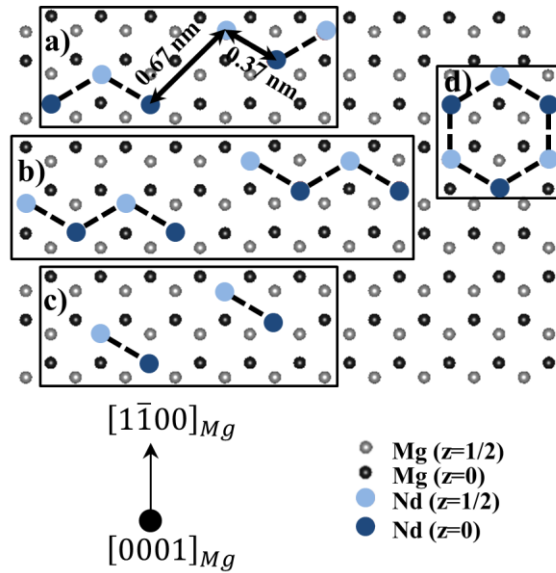
Figure 2: a-d) Atomic structure models showing the atomic structure of the b) V, c) N, d) two-column unit, and e) hexagonal ring arrangements of the GP zones in Mg-Nd alloys. The Mg structure was created using VESTA [25].

2.1.3 β' phase

The β' phase is the next phase to form in the precipitation sequence and has been shown to nucleate from pre-existing GP zones as plates elongated along $\langle 1\bar{1}00 \rangle_{Mg}$ directions [22, 26], as shown in **Figure 3**. The β' has an orthorhombic unit cell with lattice parameters equal to $a=a_o=0.64$ nm, $b=2\sqrt{3}a_o=1.14$ nm, $c=c_o=0.52$ nm with an orientation relationship with respect to

the matrix such that $[001]_{\beta'}//[0001]_{Mg}$ and $(100)_{\beta'}//(11\bar{2}0)_{Mg}$ [22], however a recent study showed the structure of β' to be slightly distorted such that it is longer along $[11\bar{2}0]_{Mg}$ (0.70 nm) and shorter along $[1\bar{1}00]_{Mg}$ (1.1 nm) [27]. The β' structure consists of Nd-rich columns arranged into either rows of parallel zigzag chains or rows of hexagonal rings stacked along $\langle1\bar{1}00\rangle_{Mg}$-type directions [22]. Why the structure contains two different structural features has yet to be determined. Based on the atomic structure of the β' phase containing only zigzag chains, the composition was calculated to be Mg_7Nd [22].

The shape of coherent β' precipitates appears to be controlled by a combination of interfacial energy and elastic strain energy. A previous phase field study modeled the shape of β' using different combinations of interfacial and elastic strain energies [28]. When using only interfacial energy the precipitates had habit planes lying parallel to the basal plane, while using only elastic strain energy resulted in plates lying parallel to the $\{11\bar{2}0\}_{Mg}$-type planes with equal lengths along $[0001]_{Mg}$ and $\langle1\bar{1}00\rangle_{Mg}$ directions. Using contributions from both interfacial and elastic strain energies resulted in plate-shaped precipitates with the longest dimension along the $\langle1\bar{1}00\rangle_{Mg}$ directions [28]. Despite one report [22], there is little experimental information available about the size of the β' phase and how it evolves with aging, leaving the phase field predictions inconclusive due to the lack of experimental evidence of the β' morphology.
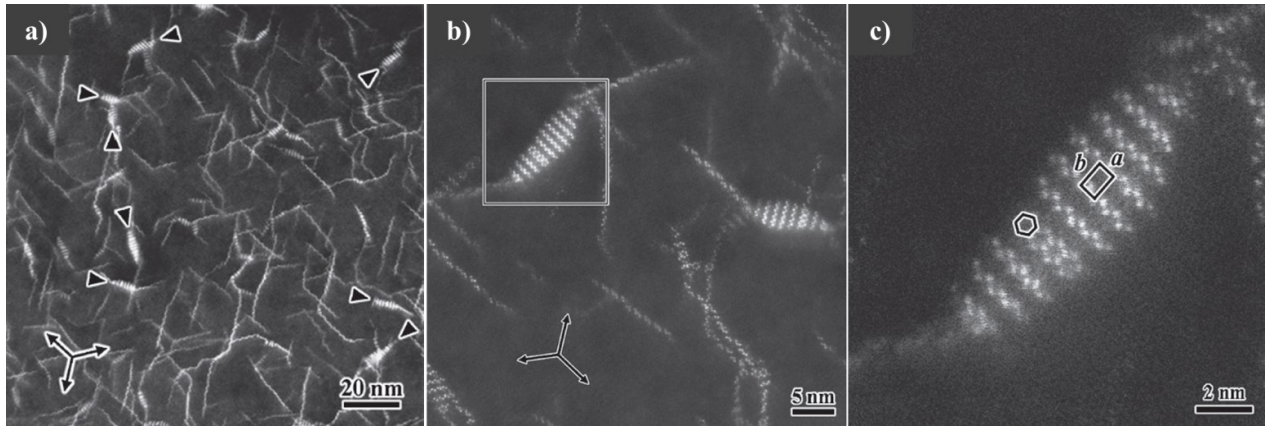
Figure 3: a)-c) HAADF-STEM images of a Mg-0.5 at. % Nd alloy aged at 170 ^{o}C for 100 hours, taken with the incident beam parallel to [0001]$_{Mg}$. Black arrows indicate β' precipitates. c) high mag image of the β' precipitate [22].

2.1.4 β$_1$ phase

The β$_1$ phase is also a metastable phase in the binary Mg-Nd system and forms as plates parallel to any of the $\{10\bar{1}0\}_{Mg}$-type planes [22]. **Figure 4a** and **b** shows a typical arrangement of β$_1$ platelets arranged into a triangular pattern where each platelet is separated by 120°. The β$_1$ platelets have a face-centered cubic structure with an orientation relationship with respect to the matrix such that $(\bar{1}12)_{\beta_1}//(10\bar{1}0)_{Mg}$ and $[110]_{\beta_1}//[0001]_{Mg}$ [2, 22]. Based on its structure the composition of the β$_1$ phase was calculated to be Mg$_3$Nd [22].

The β$_1$ phase has an apparent relationship with the β' phase such that the β' phase is attached to both ends of the β$_1$ plates (shown in **Figure 4c**). The attachment of β' particles at the ends of β$_1$ platelets was originally reported to occur in WE alloys, where it was suggested that the formation of the β$_1$ involves significant shearing of the Mg matrix, causing the globular β' particles to nucleate at the ends of the plates in order to minimize the strain energy [6]. A recent study using DFT, phase field, and HAADF-STEM examined the relationship between β' and β$_1$ in Mg-Nd alloys and rationalized the attachment of these two phases in terms of stress minimization [27].

They also suggested that β_1 may form from pre-existing β' [27], however experimental results are needed to confirm this hypothesis.
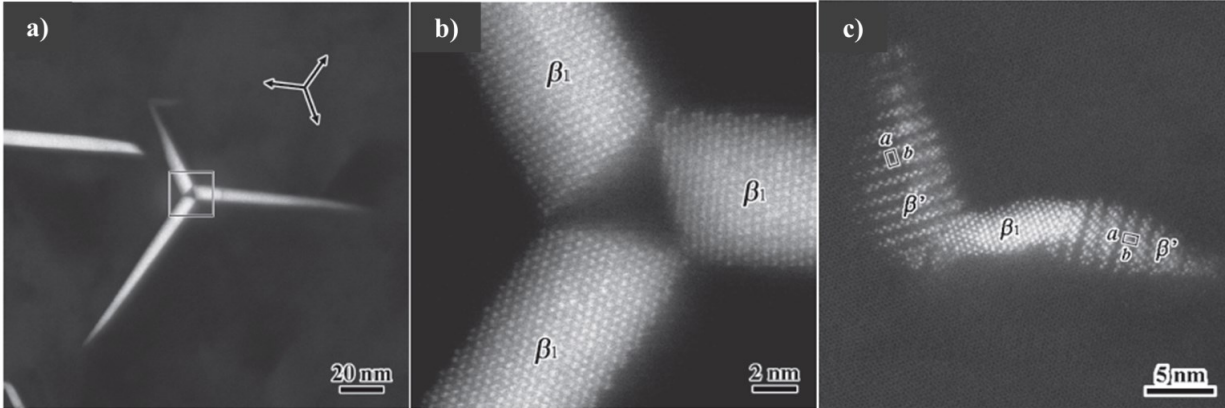
Figure 4: HAADF-STEM images of a Mg-0.5at. % Nd alloy showing a) and b) a triad structure of β_1 plates and c) a β_1 plate with two β' precipitates attached to both ends. b) high magnification image of a). The incident beam is parallel to the $[0001]_{Mg}$ zone axis [22].

2.1.5 β_2 phase

A new metastable phase referred to as the β_2 phase was introduced in a recent study on a Mg-3 wt.% Nd alloy and has only been observed at the connection point between multiple β_1 plates [29]. The β_2 phase has a hexagonal (space group $P\bar{6}$) crystal structure with lattice parameters of a=0.523 nm and c=0.963 nm and orientation relationship with respect to the Mg matrix such that $[11\bar{2}0]_{\beta_2}//[0001]_{Mg}$ and $(\bar{1}100)_{\beta_2}//(1\bar{1}00)_{Mg}$. Therefore, the orientation relationship between β_2 and β_1 is such that $[11\bar{2}0]_{\beta_2}//[110]_{\beta_1}$ and $(0001)_{\beta_2}//(1\bar{1}1)_{\beta_1}$. It was reported that the stacking of the β_2 unit cells between the β_1 platelets depends on whether the β_1 platelets are of the same variant.

2.1.6 β and β_e phases

The β phase has an irregular-shaped morphology [2] and a body-centered tetragonal crystal structure [30, 31]. The orientation relationship of the β phase with respect to the matrix is such that $(0\bar{1}1)_\beta//(11\bar{2}0)_{Mg}$ and $[100]_\beta//[0001]_{Mg}$ [32] with lattice parameters a=1.03 nm and c=0.59 nm [30]. The β phase has a reported composition of $Mg_{12}Nd$ [2]. The equilibrium β_e phase has a tetragonal crystal structure with lattice parameters a=1.47 nm and c=1.04 nm and a composition of $Mg_{41}Nd_5$ (**Figure 1**) [33, 34].

2.1.7 Aging behavior

The aging behavior has been indirectly assessed using micro hardness [21, 22, 35] and electrical resistivity measurements [20]. From the hardness curves in Refs. [21, 22, 35], it appears precipitation occurs more rapidly with increasing temperature as the peak hardness is reached after gradually shorter aging times. When aged at 200 °C [35], nucleation of a hardening phase starts at about 5-10 minutes with a fast growth stage up to 16 hours immediately followed by a significant decrease in strength. At 170 °C [22], the curve suggests at least two transformations: the continuous nucleation and growth of a first phase up to 10 hours and the formation of a second phase from 10 to 100 hours. However, as detailed above, while much work has been done to determine the structures and morphologies of the different phases that form in the binary Mg-Nd system [2, 20-22, 29], little is known about nucleation, growth, and dissolution mechanisms and kinetics of the different metastable phases. At 150 °C [21], the hardness increases upon aging due to the formation of a hardening phase, however the hardness at longer aging times is not provided and it is unclear when the alloy reaches peak hardness.

2.1.8 Effect of stress and deformation on precipitation

Precipitation in Mg-Nd alloys has been most commonly studied from material that has been cast, solution treated, and then aged and limited information is available on the effect of stress and mechanical processing on the precipitation behavior. It was reported that aging of a high pressure die cast Mg-0.5 at. % Nd alloy while being stressed resulted in accelerated growth of β' and the formation of β_1 plates at dislocations having a preferred orientation along a specific set of planes [36]. A recent study used X-ray diffraction and DSC to examine the evolution of the precipitate microstructure in a Mg-1.43 wt. % Nd alloy following high-pressure torsion (HPT) processing [37]. They reported an increase in the amount of β_1 (Mg_3Nd) and β ($Mg_{12}Nd$) phases and a decrease in the activation energies for the β''', β_1, and β phases, suggesting that a high density of defects promotes faster diffusion and precipitation.

2.2 Mg-Y alloys

2.2.1 Phase diagram

The Mg-Y phase diagram has been investigated extensively using experimental techniques and thermodynamic assessments [38-43]. According to the phase diagram obtained from Thermo-Calc 2016b software (**Figure 5**), the maximum solubility of Y in α-Mg is 11.9 mass % Y at 572 ^{o}C and decreases to 5 mass % Y at 250 ^{o}C [23]. The equilibrium intermetallic phase near the Mg-rich side of the phase diagram is the β phase with a composition of $Mg_{24}Y_5$ [2, 44]. During aging of a supersaturated solid solution of Y in Mg, a sequence of metastable phases that do not appear on this equilibrium phase diagram is observed: solute clusters, GP zones (single monolayers), orthorhombic β' (Mg_7Y), and bcc β ($Mg_{24}Y_5$) [2, 44, 45]. The next few sections

review what is currently known about these phases and reveal that there is quite a bit of work still needed to describe how the precipitate microstructure evolves with aging.
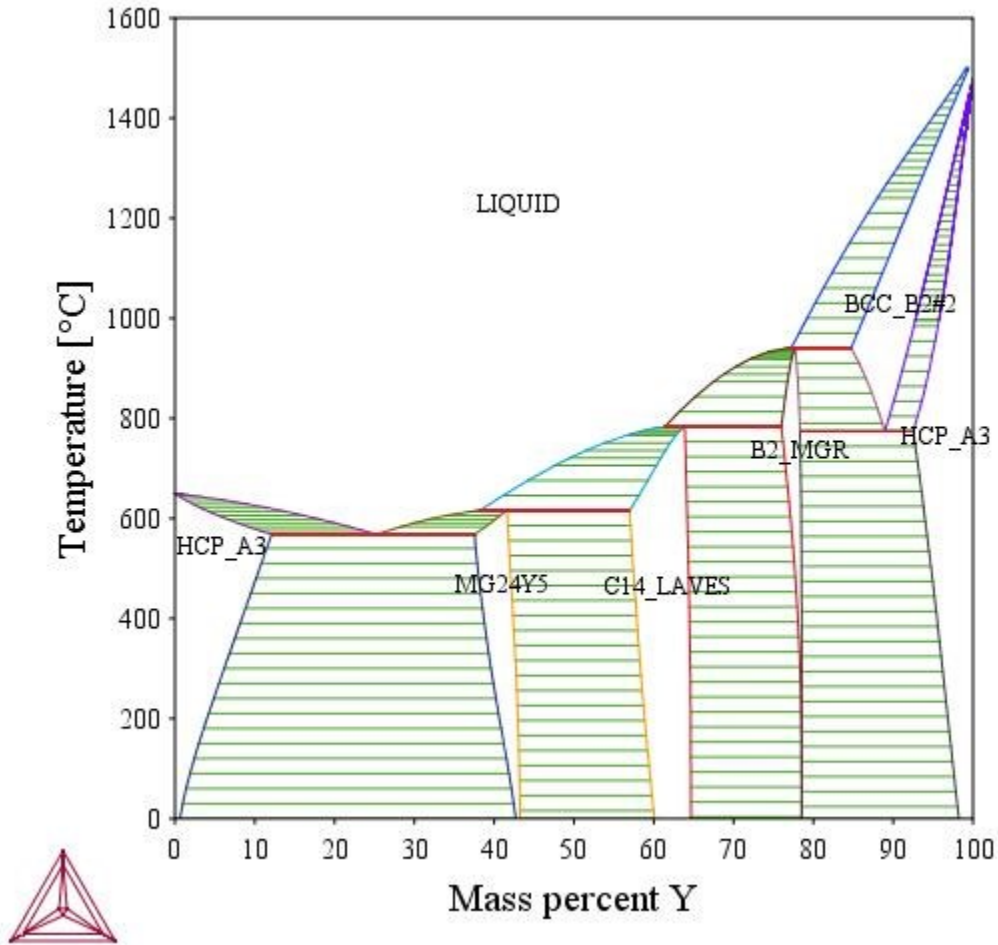
Figure 5: Binary Mg-Y phase diagram [23]

2.2.2 Solute clusters and GP zones

The early stages of precipitation involve the formation of solute clusters and GP zones. Forming first are the solute clusters which have an irregular, short-range ordered structure consisting of Y-rich columns sitting on Mg lattice sites [24]. With longer aging, these solute clusters were reported to evolve into GP zones appearing as single zigzag monolayers lying parallel to

$\{1\bar{1}00\}_{Mg}$ planes. The GP zones were suggested to act as precursors to the β' phase [24] described in the next section, however sufficient evidence illustrating the role of the monolayers on the precipitation process is lacking. A previous report showed the presence of thin strand-like features attached to the β' precipitates [46] that appear similar to the zigzag monolayers, however the details of these features could not be resolved from the reported images and no discussion was provided.

2.2.3 β' phase

The β' phase is the last metastable phase to form in the precipitation sequence. It has a base-centered orthorhombic crystal structure with lattice parameters a=0.64 nm, b=2.223 nm, and c=0.521 nm (**Figure 6**) [2]. The orientation relationship of the β' phase with respect to the matrix is such that $[001]_{\beta'}//[0001]_{Mg}$, $[100]_{\beta'}//[\bar{2}110]_{Mg}$, and $[010]_{\beta'}//[01\bar{1}0]_{Mg}$ [2]. The shape of the β' phase has been the focus of multiple studies showing that the precipitates are approximately square-shaped in the basal plane [45, 46]. A previous phase field study modeled square shapes in the basal plane when contributions from both interfacial energy and elastic strain energy were considered [46], however their models only show the shape in two dimensions. Despite one report (**Figure 6**) [45], there is little information about the size of β' along all three principal axes, therefore further investigation of the shape evolution is necessary for quantitative predictions of the precipitate behavior.
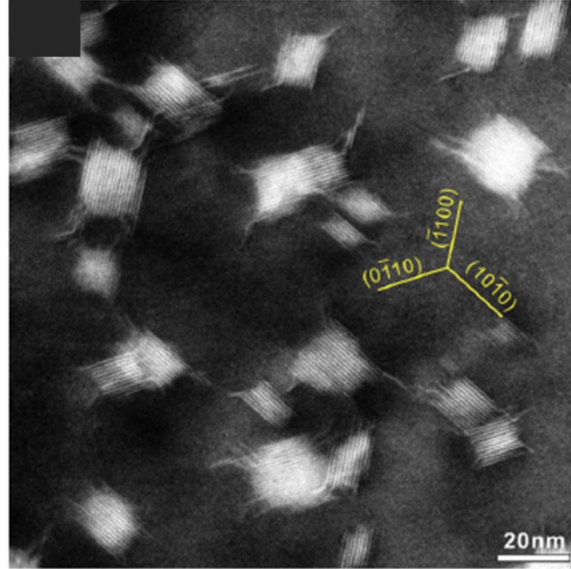
Figure 6: HAADF-STEM image of a Mg-2.32 at. % Y alloy in the peak-aged condition when viewed along the [0001]$_{Mg}$ zone axis [46].

The formation mechanism of the β' phase in Mg-Y alloys varies in the literature. An experimental report suggests heterogeneous nucleation of the β' phase from pre-existing zigzag monolayers [24], although evidence to illustrate this mechanism was not provided. Another study using DFT computation proposed the β' to form by interactions between individual zigzag monolayers [47]. Systematic investigation of the microstructure at various aging times can help confirm the nucleation mechanism of β'.

2.2.4 β phase

The equilibrium β phase forms as plates lying parallel to the $\{10\bar{1}0\}_{Mg}$ or $\{31\bar{4}0\}_{Mg}$ planes [44]. The β phase was reported to have a body-centered cubic structure (space group $I\bar{4}3m$) with lattice parameter of 1.126 nm [2, 44] and orientation relationship with respect to the matrix such that $(011)_{Mg}//(0001)_{Mg}$ and $(1\bar{1}1)_{\beta}//(\bar{1}2\bar{1}0)_{Mg}$ [44]. The composition of the β phase is reported to be $Mg_{24}Y_5$ [48].

2.2.5 Aging behavior

Hardness curves provide useful information about the effect of solute content and aging condition on precipitation behavior. The hardness of Mg-Y alloys containing different solute concentrations were measured at various aging conditions in Ref. [49]. The Mg-5 wt. % Y alloy only exhibits a slight increase in hardness at temperatures between 150 ^{o}C and 250 ^{o}C, which is not too surprising considering the close proximity to the solubility limit at the aging temperatures. On the other hand, the Mg-10 wt. % Y alloy undergoes significant age hardening at temperatures between 150 ^{o}C and 225 ^{o}C, and only limited hardening above 250 ^{o}C. Overall, precipitation occurs faster with increasing temperature within the range of 175 to 225 ^{o}C, and the shapes of the curves are similar, suggesting that the same phases form at each stage of aging. However, the alloy experiences little or no age hardening between 250 and 300 ^{o}C, indicating that either different phase(s) or fewer of the low temperature phase(s) form.

2.2.6 Stacking faults and non-basal deformation

In addition to the precipitates, stacking faults have also been reported in the microstructure of binary Mg-Y alloys [2]. Stacking faults form quite easily in Mg-Y alloys because Y is said to decrease the stacking fault energy [50]. Further adding Zn to Mg-Y has been shown to decrease the stacking fault energy even more [51]. The ease at which these stacking faults form in Mg-Y alloys has been related to the improved room temperature ductility of Mg-Y alloys compared to Mg due to the activation of multiple deformation mechanisms (basal and non-basal slip) [52]. While basal slip is a common deformation mode observed in Mg [52, 53], Mg-Y alloys have been shown to undergo pyramidal <c+a> slip as a result of heterogeneous nucleation of <c+a>

dislocations from the intrinsic stacking fault I_1 [50]. The activation of <c+a> slip provides at least five independent slip systems [53-55], resulting in homogeneous deformation [52].

2.3 Mg-Y-Nd alloys

2.3.1 Phase diagram

There is surprisingly little information about the Mg-Y-Nd phase diagram. More recently, Meng et al. focused on the Mg-rich side of the Mg-Y-Nd phase diagram at 480°C using SEM, XRD, and EPMA techniques [56] and reported six phases; α-Mg, β, $Mg_{41}Nd_5$, Mg_3Nd, $Mg_{24}Y_5$, and Mg_2Y [56]. The ternary phase diagrams for the Mg-Y-Nd system drawn at 480°C and 250°C [56] are shown in **Figure 7**. During age hardening, a sequence of metastable phases form from the supersaturated solid solution of Nd and Y in Mg that do not appear on this equilibrium phase diagram: GP zones, hcp $D0_{19}$ β'' (Mg_3Nd), orthorhombic β' ($Mg_{12}YNd$), fcc $β_1$ ($Mg_3(Nd,Y)$) and fcc β ($Mg_{14}Nd_2Y$) [2-6]. The structural and morphological details of each phase are reviewed in the following sections.
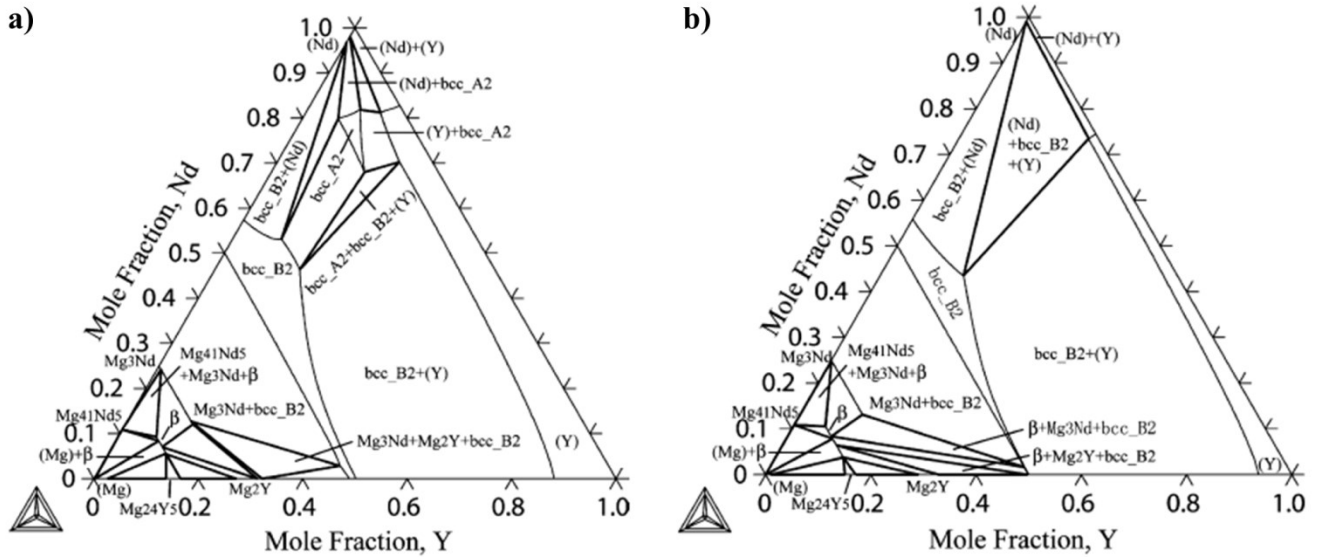
Figure 7: Calculated isothermal sections of the Mg-Y-Nd phase diagram at a) 480°C and b) 250°C [56].

2.3.2 β" phase

The β" phase forms as fine precipitate plates lying parallel to the $\{11\bar{2}0\}_{Mg}$ planes [7]. It is reported to have a $D0_{19}$ structure and orientation relationship with respect to the matrix such that $[0001]_{\beta"}//[0001]_{Mg}$ and $[01\bar{1}0]_{\beta"}//[01\bar{1}0]_{Mg}$. The composition of β" was measured using in situ energy dispersive X-ray analysis to be $Mg_3(Y_{0.85}Nd_{0.15})$ [57]. It was suggested that longer aging results in an in-situ transformation of the β" platelets to the β' phase discussed in the next section [7].

2.3.3 β' phase

The β' phase forms as equiaxed shaped particles in the basal plane. It has a base-centered orthorhombic crystal structure (point group is mmm) [2, 5, 6, 58] with lattice parameters $a_{\beta'}$=0.64 nm, $b_{\beta'}$=2.23 nm, and $c_{\beta'}$=0.52 nm and orientation relationship with respect to the matrix such that $[001]_{\beta'}//[0001]_{Mg}$ and $(100)_{\beta'}//(1\bar{2}10)_{Mg}$ [2, 4, 59]. Depending on the

aging stage, the globular β' precipitates have been reported to be invariably attached to at least two platelets of either the β'', β', or β_1 platelet phases on either side of the precipitates [5, 7], as shown in **Figure 8**.

The reported composition of the β' phase varies in the literature. It has been suggested to be either $Mg_{12}YNd$ [2-4] or $Mg_{24}Y_2Nd_3$ [57], however, Nie and Muddle showed the β' phase to have a higher Y content than Nd in a WE54 alloy [6]. Choudhuri et al. also reported a higher Y content than Nd in the globular β' phase for a WE43 alloy, but their atom probe results showed that Zr was the main solute element [60]. Therefore, the composition of β' remains to be unambiguously determined.
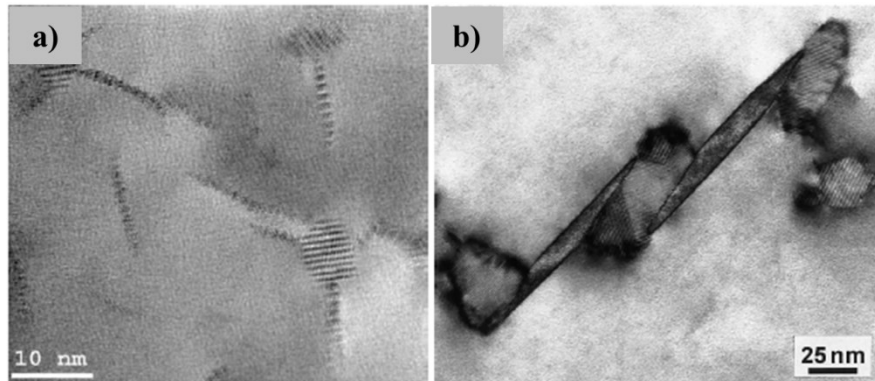
Figure 8: HREM and TEM images of a) a WE43 sample aged for 2 hours at 250°C [7] and b) a WE54 sample in the T6 condition [6].

2.3.4 β_1 phase

The β_1 phase forms as plates lying parallel to $\{01\bar{1}0\}_{Mg}$ planes [5, 6]. The plates have a face-centered cubic crystal structure (Fm$\bar{3}$m, lattice parameter of 0.74 nm) which is isomorphous with Mg_3X (X=Nd, Ce, La, Pr, Dy, Sm [5]. The β_1 phase has an orientation relationship with respect to the matrix such that $[110]_{\beta_1}//[0001]_{Mg}$ and $(\bar{1}12)_{\beta_1}//(1\bar{1}00)_{Mg}$ [6]. There are three sets of

β_1 plates that share a common habit plane and are twin related, resulting in six possible orientation variants.

The formation mechanism of the β_1 phase has been debated in the literature. Nie and Muddle proposed that the β_1 plates form by an invariant plane strain transformation of the Mg lattice in which the globular β' particles form at the ends of the plates in order to accommodate the shear strain [6]. Apps et al., suggested that the β_1 phase forms by an in situ transformation of the β'' phase [58]. Due to the lack of experimental evidence, how the β_1 phase forms remains unclear.

2.3.5 β phase

The equilibrium β phase forms heterogeneously on dislocations, pre-existing precipitates within grains, and at grain boundaries as plates parallel to $\{01\bar{1}0\}_{Mg}$ planes [2-5]. The habit plane of the equilibrium β phase has been suggested to deviate from $(1\bar{1}2)_\beta/(10\bar{1}0)_{Mg}$ by about 3° to minimize interfacial energy [61]. The β plates have a face-centered cubic crystal structure ($F\bar{4}3m$) with a lattice parameter a_β=2.223 nm and orientation relationship with respect to the matrix such that $[110]_{\beta_1}//[0001]_{Mg}$ and $(\bar{1}12)_{\beta_1}//(1\bar{1}00)_{Mg}$ [2]. The composition of the β phase varies in the literature. It has been reported to be either $Mg_{14}Nd_2Y$ [3, 4] or $Mg_{12}NdY$ [4].

The β phase forms by a transformation from the β_1 phase, resulting in distinct domains of β phase within the β_1 plates [5, 6, 58]. Even after a single β_1 plate has completely transformed to β, the plate may contain several different domains of β [6]. The orientation relationship between the β and β_1 phases is such that their principal axes are parallel to one another [6].

2.3.6 Aging behavior

The overall kinetics and temperature dependence of these phase transformations has mainly been studied using Vickers hardness and differential scanning calorimetry (DSC). Both WE43 and WE54 experience similar aging behavior at each aging temperature, as shown in Refs. [3, 4]. However, the absolute value of hardness for the WE54 alloy [4] is greater than the WE43 alloy [3], which suggests that a larger amount of Y leads to a higher strengthening effect.

According to DSC, hardness measurements, and microstructural analysis, the hardness increase at low temperatures (150 ^{o}C) is due to the formation of β" and β' phases [3, 4, 7]. At 210 and 250 ^{o}C the phases present at peak hardness are the globular β'and platelet β_1 precipitates [5, 6, 8]. Aging at higher temperatures bypasses the formation of β" and β' phases and only the β_1 and β phases form [8, 62].

2.3.7 Effect of double heat treatments on precipitation sequence

Secondary aging occurs at lower aging temperatures (i.e. below 200°C) after the alloy has undergone a primary aging treatment (250°C to peak hardness) and has been associated with a decrease in ductility [3]. A recent study showed the presence of small precipitates in the form of either zigzag monolayers lying parallel to $\{10\overline{1}0\}_{Mg}$ planes or hexagonal rings scattered homogeneously in the matrix in between large pre-secondary aged precipitates [13]. Plates lying parallel to $\{11\overline{2}0\}_{Mg}$ planes and having a primitive orthorhombic crystal structure similar to that of β' in Mg-Nd alloys [22] have also been reported in secondary aged WE54 [13].

2.3.8 Effect of processing on precipitation

Most studies on precipitation have focused on cast, solutionized, and aged alloys [4, 6, 7], while engineering alloys for commercial applications are typically mechanically processed prior to aging. Some studies have examined the effect of hot-rolling and tri-axial forging on precipitation [60, 63]. In both cases, precipitation was aided by dislocations introduced during processing.

During aging of a hot-rolled WE43 alloy an interesting honeycomb structure consisting of β_1 precipitates lying parallel to $\{1\bar{1}00\}_{Mg}$ planes with globular β' particles located between these plates was observed in the microstructure [60]. It was suggested that dislocations arrange into hexagonal-shaped networks on the close-packed $\{0001\}_{Mg}$ planes during hot-rolling and that Nd diffuses to these regions resulting in the eventual formation of the honeycomb network of β_1 plates during aging. This honeycomb structure is an ideal precipitate arrangement for strengthening [1].

A study investigating the effect of tri-axial forging on the precipitation behavior in a WE43 alloy showed that dynamic precipitation occurs during deformation at 390°C [63]. Precipitation was reported to occur more rapidly during deformation compared to the undeformed alloy. Although there are multiple factors that influence dynamic precipitation, the early formation of β_1 platelets during deformation was attributed to the high density of dislocations.

2.4 Strengthening mechanisms

The precipitate phases that form in Mg-RE alloys are unique because they form with habit planes parallel to the prismatic planes of the Mg matrix and are therefore more efficient at blocking

moving dislocations [1, 64]. In addition to the precipitate orientation, other factors such as the precipitate shape, number density, size, and dislocation interaction mechanism affect precipitation strengthening. Many of the studies to date have focused on developing models that describe the strengthening behavior of β_1 precipitates and assumed an Orowan mechanism operates [1, 64, 65]. However, these models are inconclusive due to the lack of experimental evidence showing the strengthening mechanism of the phases that form in Mg-RE alloys.

2.5 Summary

This chapter reviewed the different precipitate phases that form in Mg-Nd, Mg-Y, and Mg-Y-Nd alloys during aging and related the phases to previously reported hardness curves. The general atomic structures and shapes of the precipitates in the basal plane have been reported, however experimental quantification of the evolution of these precipitate structures is still needed in order to determine the thermodynamic and kinetic driving forces controlling their behavior. There is also a lack of understanding on the effect of alloying element on precipitation. For instance, the different atomic arrangements and shapes of the β' phases in Mg-Nd and Mg-Y and their role in the precipitation process remain unclear. In addition, these phases are commonly observed in peak-aged microstructures, and their strengthening mechanisms still need to be determined in order to accurately quantify the strengthening contribution from the precipitates on the alloy strength. Thus, this thesis provides a quantitative analysis of the aging behavior of the early precipitate phases in Mg-RE alloys containing Nd and Y and identifies the formation mechanisms of these phases. In addition, the strengthening mechanisms of the globular and platelet β' phases will be identified. Overall, this work will provide a more comprehensive

understanding of the precipitation behavior that is needed when designing alloys with specific properties.

CHAPTER 3:

The evolution of the early precipitate phases in Mg-Nd-(Zr) alloys[1]

3.1 Introduction

As described in Chapter 2, the precipitation sequence in Mg-Nd alloys is generally assumed to involve the successive formation of the following metastable phases from the supersaturated solid solution: GP zones or β'' (Mg_3Nd), orthorhombic β' (Mg_7Nd), hcp β_2, fcc β_1 (Mg_3Nd), bct β ($Mg_{12}Nd$), and tetragonal β_e ($Mg_{41}Nd_5$) [2, 20-22, 29]. These studies have revealed important information about the general atomic structures and morphologies of the main precipitating phases when viewed along the c-axis, yet much work remains to quantify the precipitation mechanisms and kinetics as well as the precipitate characteristics. Most of the images of the precipitates presented in the literature have only shown snapshots of individual precipitates at select aging conditions along the c-axis and do not provide sufficient information about the evolution of the precipitate microstructure and the morphology with aging. In order to accurately interpret the complex precipitate structures, analysis of the precipitates in multiple orientations is necessary. Additionally, the nucleation mechanisms for the different precipitates have yet to be identified and are critical in the design of high strength alloys. Some arguments

---

[1] The content of this chapter is adapted from the following published articles:
[1] E.L.S. Solomon, E.A. Marquis, Magnesium Technology, TMS, Nashville, TN, 2016.
[2] A.R. Natarajan, E.L.S. Solomon, B. Puchala, E.A. Marquis, A. Van der Ven, Acta Materialia 108 (2016) 367.
[3] E.L.S. Solomon, V. Araullo-Peters, J.E. Allison, E.A. Marquis, Scripta Materialia 128 (2017) 14.

have been made about the formation mechanism of the β_1 phase [6, 27, 58], however sufficient experimental evidence to support these arguments is lacking.

In this chapter, the evolution of the precipitate microstructure is characterized at different aging conditions along all three principal axes ($\langle 1\bar{1}00 \rangle_{Mg}$, $\langle 11\bar{2}0 \rangle_{Mg}$, and $[0001]_{Mg}$) using HAADF-STEM and APT. A detailed analysis of the precipitate atomic structure and quantitative description of the precipitate morphologies are presented. Evidence of the relationships between the different phases that indicate their formation mechanisms are also identified.

For this chapter, the β'' and β' phases reported previously in Mg-Nd alloys will be referred to as GP zones and β''' throughout this chapter based on results from Ref. [66]. The APT data in this chapter was obtained by Vicente Araullo-Peters to provide a comprehensive analysis of the precipitation behavior in Mg-Nd-(Zr) alloys. APT revealed that precipitation is not affected by the presence of Zr thereby allowing the analysis of the Mg-Nd and Mg-Nd-Zr alloys to be combined into one chapter.

3.2 Experimental

The alloys examined in this work were provided by Magnesium Elektron North America Inc. The compositions of the two alloys were measured by inductively coupled plasma mass spectrometry (ICP-MS) and found to be Mg-2.35 wt.% (0.40 at.%) Nd and Mg-2.18 Nd-0.32 Zr (Mg-0.38 Nd-0.09 Zr at. %). Results from APT were collected from the Mg-Nd-Zr alloy while results from HAADF-STEM were obtained from the binary Mg-Nd alloy. Since precipitation is not affected by the presence of Zr direct comparisons can be made between these two alloys. The alloys were encapsulated in quartz tubes under an argon and sulfur hexafluoride atmosphere

and solution treated at 560 ^{o}C for 24 hours followed by water quenching. Samples were then aged in an oil bath at either 200 ^{o}C or 250 ^{o}C for times ranging between 3 min and 128 hours. Hardness measurements were obtained using a Vickers microhardness indenter with a load of 100 grams and dwell time of 15 seconds. The APT specimens were electropolished with a solution of 25% perchloric acid in acetic acid using 14-20 V and then fine polished with a solution of 2% perchloric acid in butoxyethoanol with 5-10 V. The APT data was collected on a Cameca LEAP XHR4000 instrument operated in voltage mode with a specimen temperature of 50 K. The data was collected at detection rates varying between 0.005 and 0.01 atoms per pulse on average using a voltage pulse fraction of 20% and a repetition rate of 200 kHz. The data was then reconstructed using the Integrated Visualization and Analysis Software (IVAS 3.6.12) package. The reconstruction parameters, geometric factor, and image compression factor were chosen to ensure that the planar spacings observed at identified poles and the angles between such planes match that of the hexagonal magnesium matrix. The evaporation field was selected to be that of Mg at 21 V/nm [67]. Crystallographic analysis methods developed for APT [68] were used to determine the orientation of the APT data. Specimens for transmission electron microscopy were prepared by punching 3 mm discs from heat treated foils, ground to a thickness of 0.10 mm and twin-jelectropolished in a solution of 10.6 g lithium chloride, 22.32 g magnesium perchlorate, 1000 ml methanol and 200 ml 2-butoxyethanol at -55 ^{o}C based on Ref. [5]. High-angle annular dark field (HAADF)- scanning transmission electron microscopy (STEM) images were obtained using a JEOL 2100F microscope operated at 200 kV with a collection angle of 52 mrad and a double-corrected JEOL 3100 microscope operated at 300 kV with a collection angle of 74 mrad.

3.3 Results

3.3.1 Aging behavior

The aging response of a Mg-2.35 wt. % Nd (Mg-0.40 at. % Nd) alloy at 200 $^{\circ}$C and 250 $^{\circ}$C is presented in **Figure 9**. When aged at 200 $^{\circ}$C the alloy reaches its peak hardness between 1 and 4 hours of aging. Longer aging results in a decrease in the hardness as the alloy is overaged. Aging at 250 $^{\circ}$C occurs a bit faster as the peak hardness is reached between 7 and 15 minutes of aging, where after the hardness gradually decreases. Using conventional and scanning transmission electron microscopy, the phases present at the different stages of aging at each temperature were determined.
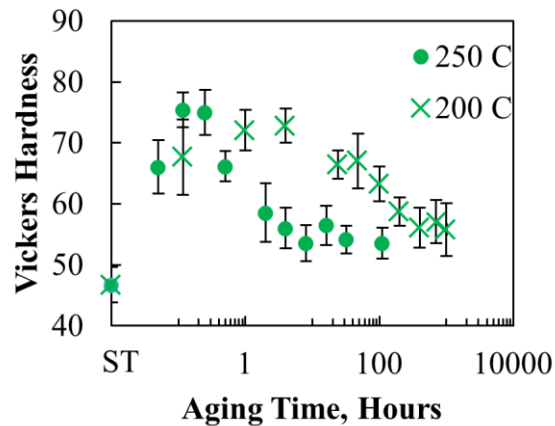
Figure 9: Hardness curves for the Mg-0.40 at. % Nd alloy. ST represents the solution treated condition. Reprinted from Ref. [69] and [70]

At 200 $^{\circ}$C the GP zones and β''' phase appear to be the hardening phases in this alloy. The microstructure contains similar amounts of these two phases at peak hardness (**Figure 10a**), and after 16 hours when the hardness has decreased, the microstructure contains noticeably less GP zones and β''' precipitates as their sizes have increased (**Figure 10b**). When aged at 250 $^{\circ}$C the

β''' phase continues to be the main hardening phase. Indeed, the microstructures after aging for 3 min at 250 ^{o}C contains GP zones and β''' (**Figure 11a**), while the microstructure at the hardness peak (15 minutes of aging) contains primarily larger β''' with residual GP zones (**Figure 11b**). At 1 hour the microstructure contains primarily β''' and by 2 hours the hardness has dropped significantly as the GP zones have completely dissolved and both the β''' and β$_1$ phases are present, as shown in **Figure 11c** and **d**.
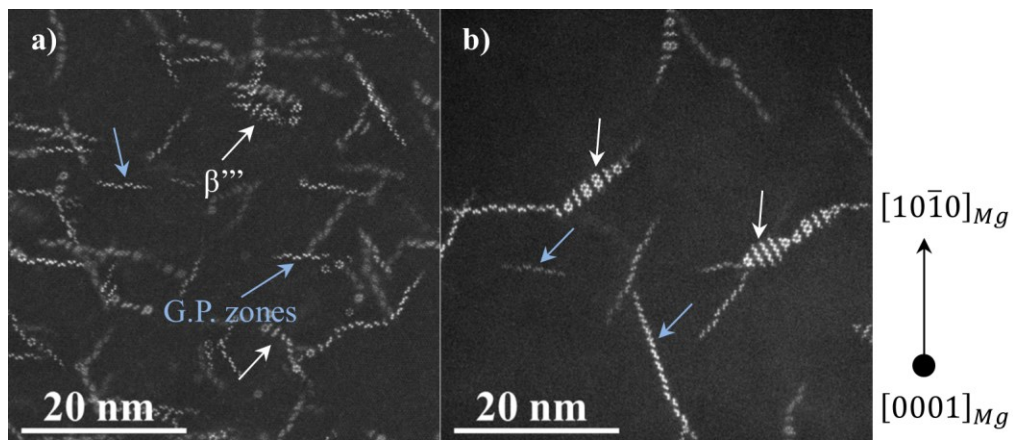
Figure 10: HAADF-STEM images of the Mg-0.40 at. % Nd alloy age treated for a) 1 hour and b) 16 hours at 200 ^{o}C with the incident beam parallel to the [0001]$_{Mg}$ zone axis. GP zones and β''' phases are identified with white and blue arrows. The crystallographic orientations for each image are provided to the right of the figure.

28
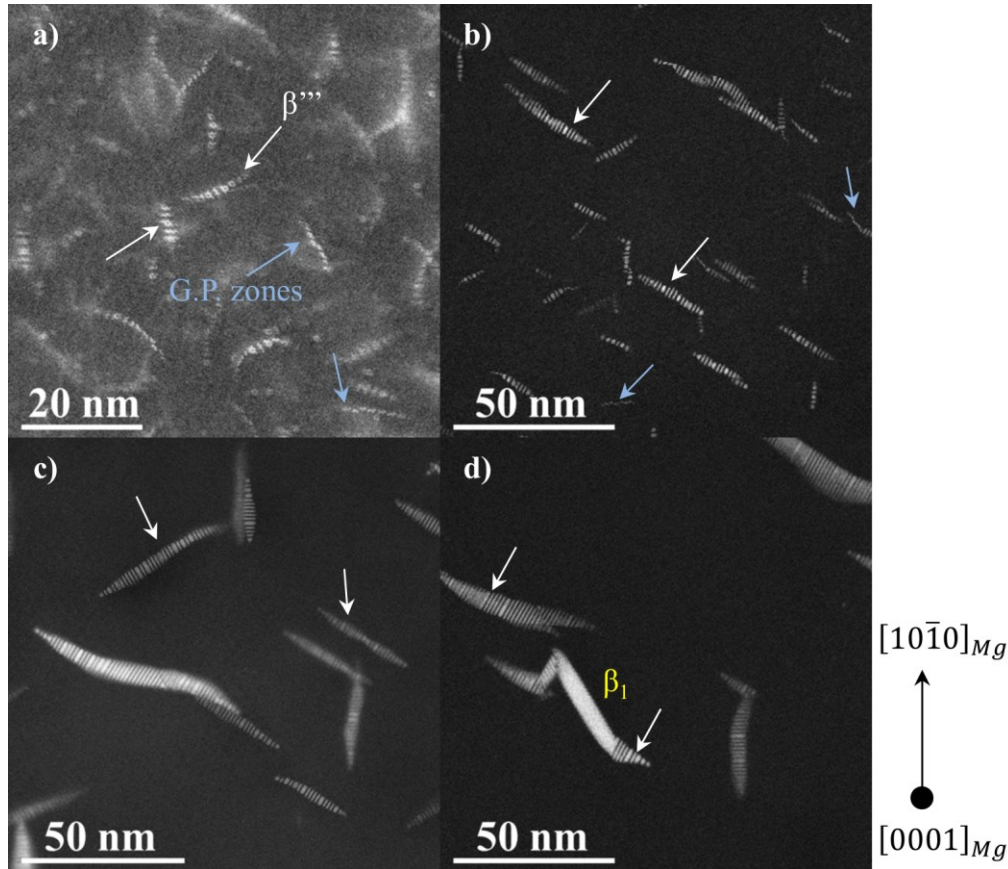
Figure 11: HAADF-STEM images of the Mg-0.40 at. % Nd alloy age treated for a) 3 minutes, b) 15 minutes, c) 1 hour, and d) 2 hours at 250 °C with the incident beam parallel to the [0001]$_{Mg}$ zone axis. The crystallographic orientations for each image are provided to the right of the figure. Reprinted from Ref. [69]

3.3.2 Atomic structure of GP zones

The atomic structures of the GP zones and β''' phase consist of (0001) columns of Nd atoms arranged on Mg lattice positions in variations of a triangular pattern, as illustrated in **Figure 2** and **Figure 12**-**Figure 14**. The GP zones exist as either individual hexagonal rings, V or N shapes, or two-column units with a D0$_{19}$-type ordering (**Figure 2** and **Figure 12**), as was previously reported [22, 24]. The V and N shapes are arranged in chains extending in the $\langle 11\bar{2}0 \rangle_{Mg}$-type directions and have a slight difference in habit plane that is related to the staggering of the N and V units. The V units (**Figure 2a** and **Figure 12a**) alternate such that their apex is pointing up in one unit and down in the neighboring unit. Each matching unit lies

on the same $\{1\bar{1}00\}_{Mg}$ plane. Conversely, the N units (**Figure 2b** and **Figure 12b**) have identical atomic arrangements and each subsequent N unit sits on different but parallel $\{1\bar{1}00\}_{Mg}$ planes creating an angle of 10.9° from the $\{1\bar{1}00\}_{Mg}$ plane. The two-column units (**Figure 2c** and **Figure 12c**) are also apart of chain-like structures yet they are typically observed within chains containing the V and N shapes rather than forming long chains of only two-column units.
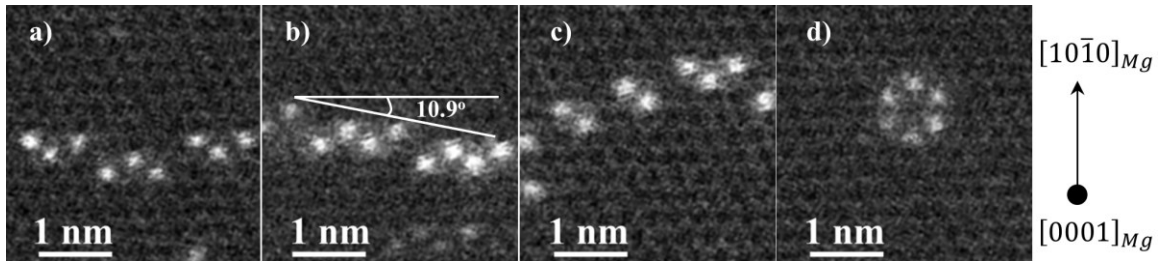
Figure 12: HAADF-STEM images of the Mg-0.40 at. % Nd alloy age treated for 1 hour at 200 °C with the incident beam parallel to the $[0001]_{Mg}$ zone axis showing the a) V-shaped, b) N-shaped, c) two-column unit, and d) hexagonal ring arrangements of the GP zones. The crystallographic orientations for each image are provided to the right of the figure.

3.3.3 Atomic structure of β'''

The β''' phase is also made up of these triangular units yet arranged in a different pattern (**Figure 13** and **Figure 14**). The triangular units of β' form long chains that are aligned in parallel rows of zigzag chains extending along the $\langle 10\bar{1}0 \rangle_{Mg}$-type directions, consistent with the Mg_7Nd stoichiometry. The interface between the β''' precipitates and the matrix is coherent and no interfacial dislocation was observed. The average spacing between the Nd columns along the $[11\bar{2}0]_{Mg}$ direction measured from five β''' precipitates similar in size to that shown in **Figure 14** is 0.72±0.02 nm yielding an estimated strain between 9 and 15% between the β''' phase and matrix. The average spacing between the $\{010\}_{β'}$ and $\{001\}_{β'}$ planes along the $\langle 10\bar{1}0 \rangle_{Mg}$ and $[0001]_{Mg}$ directions were measured at 1.1±0.01 nm and 0.51±0.01 nm, which match closely to four $\{1\bar{1}00\}_{Mg}$ plane spacings ($\{1\bar{1}00\}_{Mg}$ plane spacing = 0.278 nm) and one $(0001)_{Mg}$ plane

30

spacing (0.521 nm), resulting in little (<2%) to no strain in these directions. This would suggest that the morphology of these β''' precipitates is controlled by strain minimization as they are longest along the $[0001]_{Mg}$ direction and shortest along a $\langle 11\bar{2}0 \rangle_{Mg}$ direction and is discussed in more detail in **Section 3.3.4**.
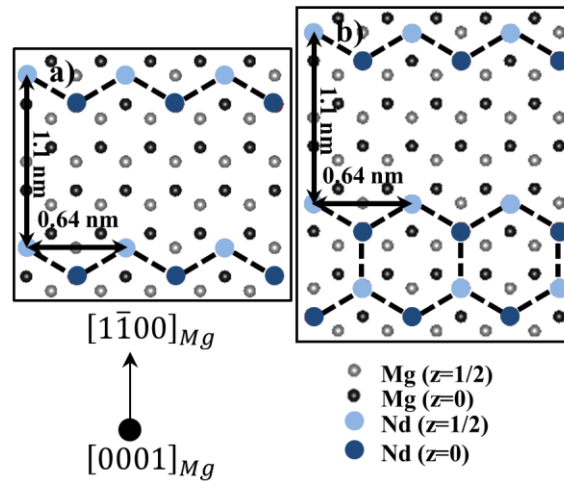
Figure 13: Atomic structure model of the β''' phase containing a) only zigzag chains and b) a zigzag chain and row of hexagonal rings. The Mg matrix was created using VESTA [25].

On closer inspection, it appears that the structure of β''' is more complex than previously reported. In addition to the rows of zigzag chains, the β''' phase contains rows of hexagonal rings (**Figure 13b** and **Figure 14**), as reported previously [22], however it has been unclear why β''' contains hexagonal rings and whether they form in specific patterns. As illustrated in **Figure 14a** and **b**, the number of rows of hexagonal rings to the number of zigzag chains varies from precipitate to precipitate. The numbers of hexagonal rings and zigzag chains locally determines the concentration of the β''' precipitates. The composition of precipitates containing only chains would be 12.5 at. % Nd (Mg_7Nd) while the composition of precipitates containing only rings would be 16.7 at. % Nd. Most precipitates, small and large, exhibit both structures in different proportions. Therefore, the Nd concentration varies between 12.5 and 16.7 at. % Nd

31

from precipitate to precipitate and locally within a single precipitate, as shown in **Figure 14b** where the structures inside the red, green, and grey boxes have different Nd concentrations.

The stability of β''' precipitates containing various amounts of hexagonal rings and zigzag chains were calculated using density function theory in Ref. [66]. To summarize, β''' precipitates containing any combination of hexagonal rings and zigzag chains are equally stable in Mg-Nd alloys, however only the structures containing between 12.5 and 16.7 at. % Nd are observed experimentally. This is because there is a strong composition dependence of the misfit strain along the $\langle 10\bar{1}0 \rangle_{Mg}$ directions. Increasing the Nd concentration in the β''' precipitates above 16.7 at. % Nd results in an increase in the misfit strain along $\langle 10\bar{1}0 \rangle_{Mg}$ directions, therefore structures containing a higher concentration of Nd are not likely to form.
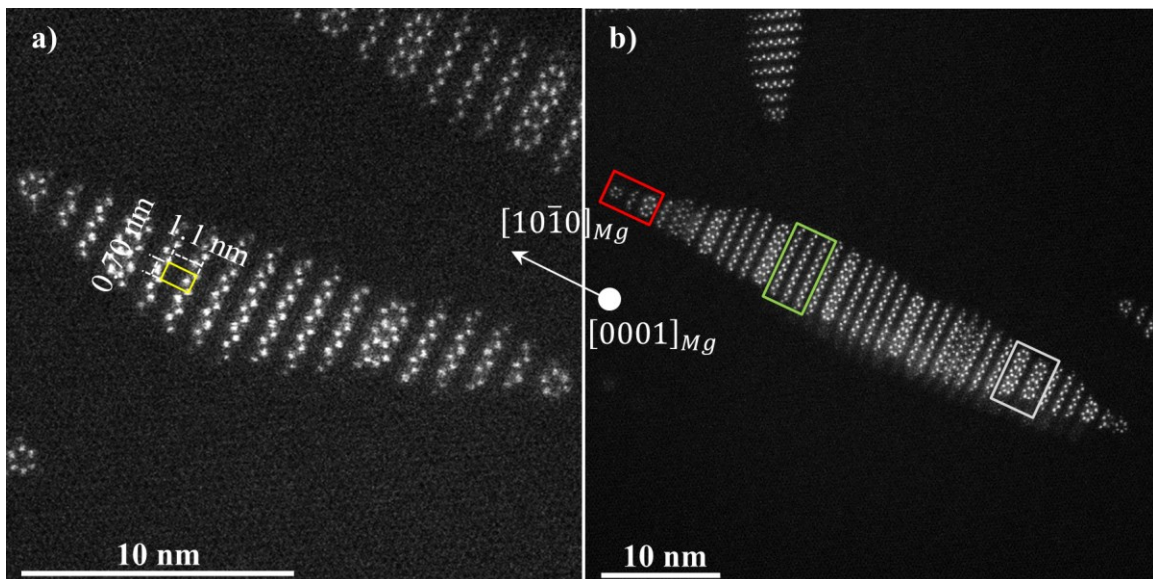
Figure 14: HAADF-STEM image of the Mg-0.40 at. % Nd alloy aged for 2 hr at 250 °C with the incident beam parallel to the [0001]$_{Mg}$ zone axis. Reprinted from Ref. [69] and [71]

Besides the hexagonal rings and zigzag chains, Nd arrangements consistent with the D0$_{19}$ structure were also observed within some β''' precipitates (**Figure 15**). These regions are often "blurry" or have low contrast, suggesting that parts of these structures may be located at a

different depth within the sample compared to the other regions of the precipitate. Stacking errors leading to shifts in the positions of the chains are also observed in many β''' precipitates (**Figure 15**).
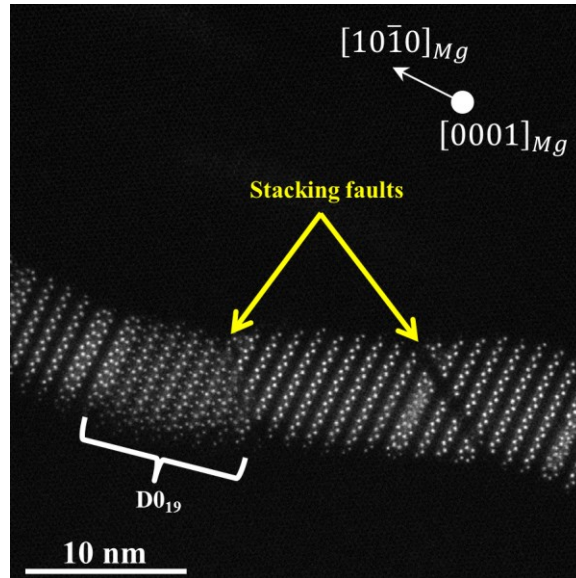
Figure 15: HAADF-STEM image of a Mg-0.40 at. % Nd alloy aged for 2 hr at 250 °C with the incident beam parallel to the $[0001]_{Mg}$ zone axis showing a region of the $D0_{19}$ structure and stacking faults. Reprinted from Ref. [69]

To elucidate the nature of the "blurry" regions, imaging of β''' precipitates was performed along the $[11\bar{2}0]_{Mg}$ zone axis. In this orientation, the hexagonal rings appear as two zigzag chains spaced 0.55 ± 0.02 nm apart. The β''' precipitate shown in **Figure 16a** shows that a single hexagonal ring does not necessarily extend the entire depth along the $[0001]_{Mg}$ direction. For instance, there are three segments of hexagonal rings shown in **Figure 16a** (individual hexagonal rings are shown in the yellow boxes) and where one segment ends as a hexagonal ring another segment is shifted by 0.55 ± 0.02 nm along a $\langle10\bar{1}0\rangle_{Mg}$ direction. The discontinuity of hexagonal ring segments results in the appearance of a $D0_{19}$-like structure that contains blurry contrast when viewed along the $[0001]_{Mg}$ direction. **Figure 16b** also illustrates stacking errors on zigzag chains, which may be consistent with the stacking faults shown in **Figure 15** when viewed along

a $\langle 11\bar{2}0 \rangle_{Mg}$ zone axis. The absence of the $D0_{19}$ structure is consistent with DFT calculations presented in Ref. [66] that shows the misfit strain to be highest at 25 at. % Nd. The complexity and high density of stacking defects present in β''' precipitates makes it difficult to interpret the STEM images. Therefore, it is important when studying these complex structures with TEM to consider their appearance in multiple orientations.
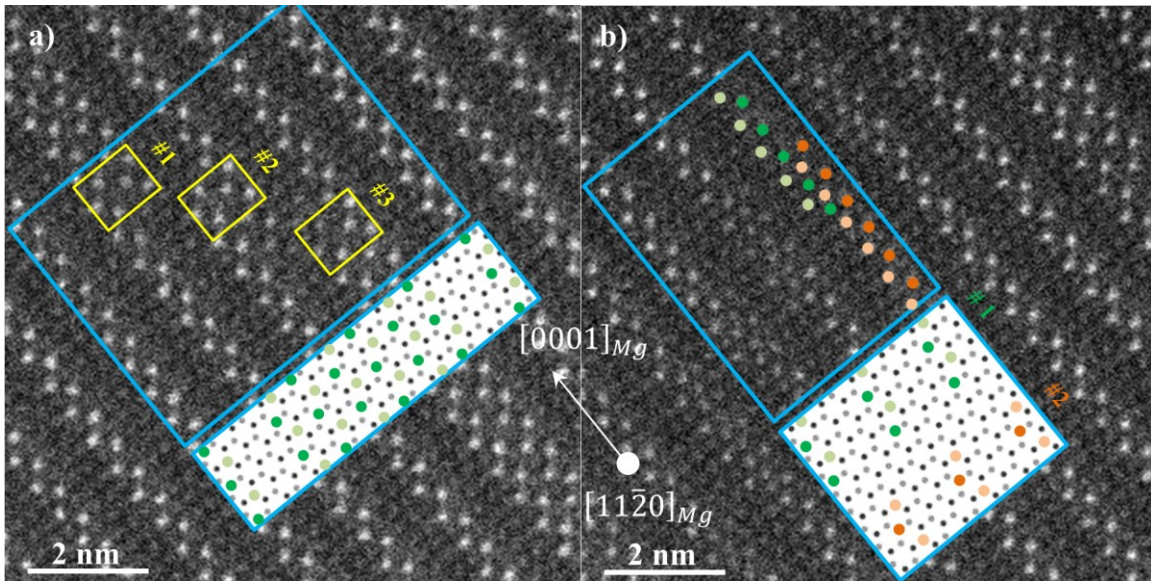
Figure 16: a) & b) HAADF-STEM images of the Mg-0.40 at. % Nd alloy aged for 2 hours at 250 °C with the incident beam parallel to the $[11\bar{2}0]_{Mg}$ zone axis. The insets show the expected 2D projection along the $[0001]_{Mg}$ zone axis of the structure enclosed in the blue box. Hexagonal rings #1-3 in each segment are labeled in a). Precipitates #1 and #2 are labeled in b). The Mg lattice was created using VESTA [25]. Reprinted from Ref. [69]

3.3.4 Size and morphology of GP zones and β'''

The 3D morphology of GP zones using APT and HAADF-STEM are shown in **Figure 12** and **Figure 17**. Since APT cannot always resolve the atomic structure of the precipitates, the precipitate phases were distinguished by their crystallographic orientations. As mentioned previously, the GP zones are thin platelets of Nd atoms with their habit plane parallel to $\{1\bar{1}00\}_{Mg}$ planes. The N and V arrangements observed by STEM are not recognizable by APT, despite the slight difference in habit plane orientation that is described in **Section 3.3.2** (**Figure**

34

12b). Size distributions and aspect ratios of the GP platelets were measured independently by APT and STEM and are presented in **Figure 18,** revealing comparable dimensions from the two techniques.   Most of the GP platelets are slightly longer in the $[0001]_{Mg}$ directions and occasionally in the $\langle 11\bar{2}0 \rangle_{Mg}$ directions. The dimension along $\langle 1\bar{1}00 \rangle_{Mg}$ directions is fixed by the atomic structure and therefore not plotted. The linear correlation between the dimensions along the $[0001]_{Mg}$ and the $\langle 11\bar{2}0 \rangle_{Mg}$ directions suggests that GP zones are thin plates with a constant aspect ratio that is independent of size.
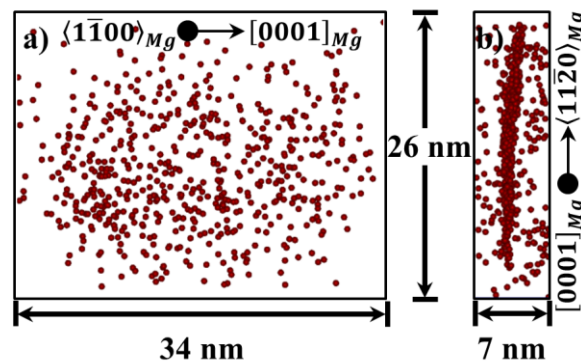
Figure 17: a) and b) APT data of a GP variant after aging at 250 °C for 15 minutes. Precipitates are viewed along the c) <1̄100>$_{Mg}$ and d) [0001]$_{Mg}$ directions. Nd atoms are shown in red. Reprinted from Ref. [72]
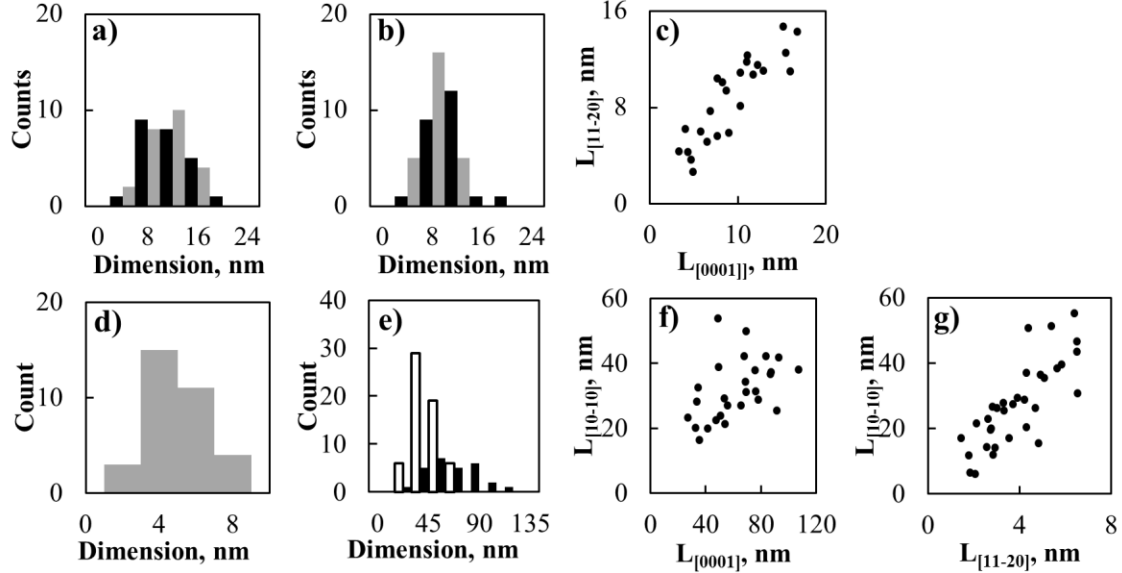
Figure 18: Size distributions and aspect ratios of a-c) GP zones and d-g) β''' precipitates after aging at 200 °C (for GP zones) or 250 °C (for β''') for 1 hour. Dimensions along $\langle 11\bar{2}0 \rangle_{Mg}$ are in grey, $\langle 1\bar{1}00 \rangle_{Mg}$ in white, and along $[0001]_{Mg}$ are in black. The data was obtained from a) APT, b) HAADF-STEM, c) APT, and d-g) HAADF-STEM. Reprinted from Ref. [72]

The 3D size distributions and morphology of β''' precipitates obtained from APT and HAADF-STEM observations are presented in **Figure 18** and **Figure 19**. Isolated β''' precipitates are longest in the $[0001]_{Mg}$ direction, shortest in the $\langle 11\bar{2}0 \rangle_{Mg}$ directions, and intermediate in the $\langle 1\bar{1}00 \rangle_{Mg}$ directions. The thickness along $\langle 11\bar{2}0 \rangle_{Mg}$ directions more strongly correlates with the length along the $\langle 1\bar{1}00 \rangle_{Mg}$ directions.

The $\{010\}_{\beta'''}$ planes have two possible arrangements of Nd atoms, which are zigzag chains or rows of hexagonal rings, as previously discussed [22]. Interestingly the thickness along $\langle 11\bar{2}0 \rangle_{Mg}$ directions is related to the atomic structure such that the platelets are thinnest when the ratio of the rows of hexagonal rings to zigzag chains is largest and vice versa. Also, when viewed along the $\langle 11\bar{2}0 \rangle_{Mg}$ zone axes, the edges of the precipitates appear facetted, as shown in **Figure 19c**. The facetted morphology observed with APT is illustrated in **Figure 19d** where the facets are parallel to the $\langle 1\bar{1}01 \rangle_{Mg}$ and $\langle 1\bar{1}02 \rangle_{Mg}$ directions. In some cases, the presence of

36

neighboring precipitates and associated strain fields might influence faceting, as shown in **Figure 19e** and **f**, where the two precipitates have matching facets along the $[0001]_{Mg}$ direction.
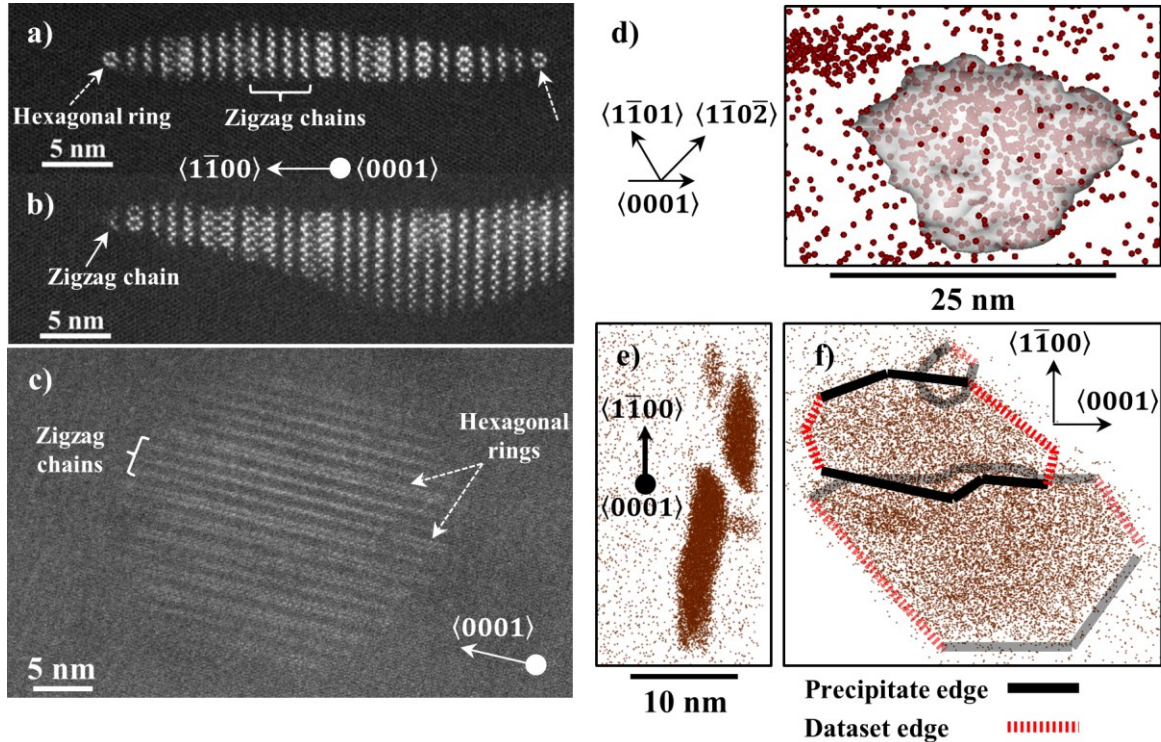
Figure 19: a-c) HAADF-STEM images and d-f) APT reconstructions of β''' precipitates after aging at 250 °C for a-c) 1 hour and d) 3 minutes. Precipitates are viewed along the a), b), and e) [0001]$_{Mg}$ and c), d), and f) <11$\bar{2}$0>$_{Mg}$ zone axes. Reprinted from Ref. [72]

Assuming thermodynamic equilibrium, coherent precipitate shapes minimize the sum of the interfacial and elastic strain energies. In general, when the precipitates are small, the interfacial energy would contribute more to the overall shape because the area to volume ratio is large. Here however, the plate-like morphologies of the GP zones and β''' are the result of a strong elastic strain energy contribution as explained in the next paragraphs. Despite their different habit planes, the GP zones and β''' precipitates are both platelets lying on prismatic planes and therefore, the same argument used to explain the shape of β''' can be extended to describe the shape of the GP zones.

Previous computational work showed that the interfacial energies for β''' are very small [28] and would therefore have a negligible contribution to the precipitate shape. In fact, previous phase field models of the β''' precipitates based only on interfacial energy values and neglecting any contribution from strains created precipitates with relative dimensions such that $l_{\langle 1\bar{1}00 \rangle_{Mg}} > l_{\langle 0001 \rangle_{Mg}} > l_{\langle 11\bar{2}0 \rangle_{Mg}}$ [28], which are inconsistent with the present experimental observations.   Alternatively, the previously calculated misfit strains [66] agree with the experimental observations of plate-shaped precipitates having relative dimensions such that the platelets are longest along $[0001]_{Mg}$, shortest along $\langle 11\bar{2}0 \rangle_{Mg}$ directions, and intermediate along $\langle 1\bar{1}00 \rangle_{Mg}$ directions. A more recent phase field study using the calculated misfit strain from Ref. [66] modeled the shape of β''' taking into consideration the variation in Nd concentration [71].   The precipitates lied parallel to $\{11\bar{2}0\}_{Mg}$ planes and were thinnest along $\langle 11\bar{2}0 \rangle_{Mg}$ directions and similar in length along $\langle 10\bar{1}0 \rangle_{Mg}$ and $[0001]_{Mg}$ directions, as shown in **Figure 20**. Although some of the more isolated β''' precipitates were equiaxed in the $\{11\bar{2}0\}_{Mg}$ planes, many of the precipitates extended noticeably further along the c-axis, which disagrees with the modeled shape. Muliparticle simulations showed that the precipitate shapes are strongly affected by neighboring precipitates such that growth of one β''' variant along $\langle 10\bar{1}0 \rangle_{Mg}$ directions was impeded by another β''' variant. This type of interaction resulted in the β''' precipitates being slightly more elongated along $[0001]_{Mg}$ directions than along $\langle 10\bar{1}0 \rangle_{Mg}$ directions, as illustrated in **Figure 21**.
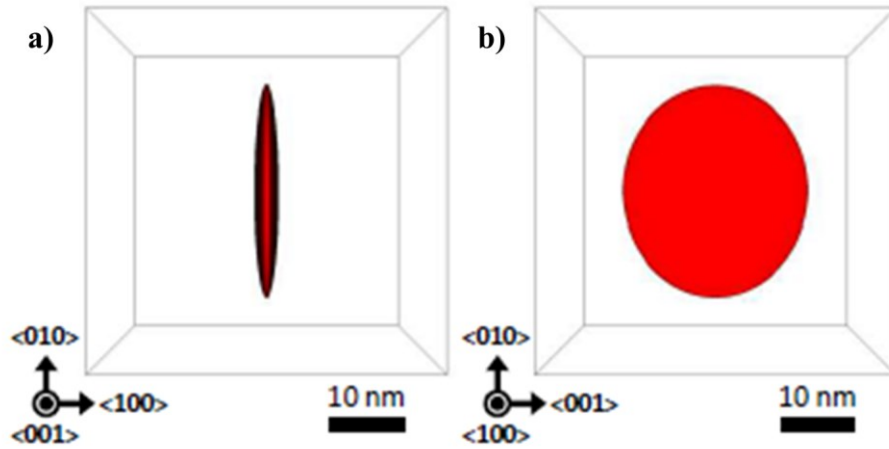
Figure 20: The final simulated morphology of β''' viewed along the a) $[0001]_{Mg}$ and b) $\langle 11\bar{2}0 \rangle_{Mg}$ zone axes. Reprinted from Ref. [71]
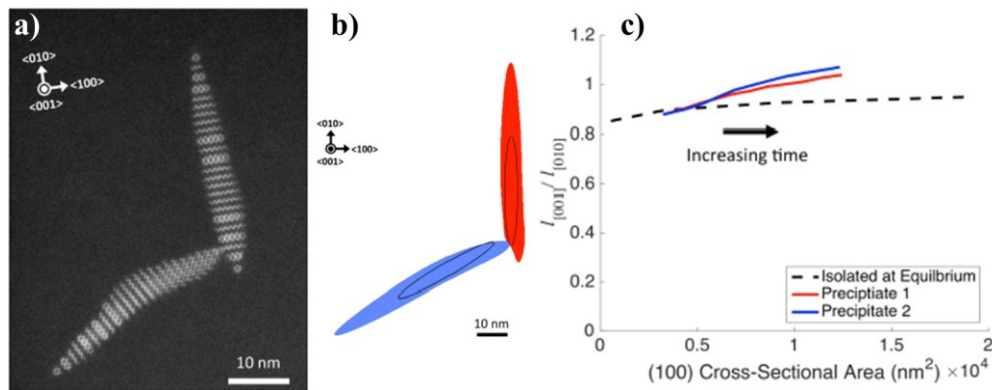
Figure 21: a) HAADF-STEM image of two β''' variants. b) Cross section of the simulated precipitates viewed in the (001) plane. The final morphology of precipitates 1 and 2 are in red and blue. The black line represents the initial morphology. c) The evolution of the $l_{[001]}/l_{[010]}$ ratio for precipitate 1 (red) and 2 (blue) shown in b) compared to the equilibrium values for isolated precipitates. The (100) cross-sectional area is approximately an ellipsoid with semi-axes $l_{[001]}/2$ and $l_{[010]}/2$. Reprinted from Ref. [71]

While elastic strain energy explains the overall dimensions along the three principle axes, it does not currently reflect the presence of facets that are visible when viewed along the $\langle 11\bar{2}0 \rangle_{Mg}$ zone axes. Further modeling may be required to explain these facets and determine whether these features are equilibrium or transient growth features. The interpretation of the observed shapes is further complicated when considering possible interactions between strain fields from

neighboring precipitates. Precipitates located within close proximity to one another causes their strain fields to interact and alter the precipitate morphologies.

Figure 18 suggests that the overall shapes for both GP and β''' precipitates are independent of size for the aging condition selected. However, the question remains whether the observed shapes are equilibrium shapes or transient morphologies that could change during the aging process due to kinetics limitations. Growth kinetics depends on the ability for solute atoms to diffuse to the growing precipitate and to attach at the interface. Considering the roughness and microfaceting visible along the precipitate interfaces (**Figure 19a-c**), it seems reasonable to expect the precipitates to grow along the $\langle 11\overline{2}0 \rangle_{Mg}$ and $[0001]_{Mg}$ directions by atoms attaching randomly to the ends of existing $\{010\}_{\beta'''}$ planes, while growth along the $\langle 1\overline{1}00 \rangle_{Mg}$ directions would require a new $\{010\}_{\beta'''}$ row to nucleate on the surface and possibly grow by the so-called ledge mechanism. As a result, when ignoring the energetic constraints, growth would be expected to be faster along the $\langle 11\overline{2}0 \rangle_{Mg}$ and $[0001]_{Mg}$ directions compared with growth along the $\langle 1\overline{1}00 \rangle_{Mg}$ directions. Growth along the $[0001]_{Mg}$ direction will be more favorable than growth along $\langle 11\overline{2}0 \rangle_{Mg}$ directions because of the high misfit strains [66]. The slowest growth rate is expected along $\langle 1\overline{1}00 \rangle_{Mg}$ directions due to the required nucleation event. As an illustration, although most of the β''' precipitates have hexagonal rings located at the ends of the precipitates (**Figure 19a**), occasionally there is a small segment of a new zigzag chain that has formed at the end, as shown in **Figure 19b**. Finally, the ledge mechanism may contribute to the observed facets (**Figure 19c** and **d**), however their presence in the majority of the observed precipitates and orientation along low index directions would rather suggest that they are characteristic of an equilibrium configuration.

3.3.5 Nucleation mechanisms of β''' and β_1 phases

Microstructural analyses revealed the β''' and β_1 phases to be important strengthening phases in Mg-Nd (see Chapter 2) and WE alloys [73], therefore it is necessary to identify how these phases nucleate in order to design high strength microstructures. Observations of the microstructures at earlier times show that some of the β''' precipitates are connected to GP chains (**Figure 10** and **Figure 11**) and contain features such as hexagonal rings, which are also seen in the GP zones. It is speculated that the β''' phase forms from the preexisting GP zones by nucleating at the ends of the GP chains. Interestingly, there is a hexagonal ring consistently located at the connection point between the GP zones and β''' phases (**Figure 22a**), which may facilitate the formation of β''', as suggested previously [26]. Due to the two-dimensional nature of the HAADF-STEM images, it is unclear how the two phases are connected along the $[0001]_{Mg}$ zone axis. The APT data in **Figure 22b** and **c** shows a GP zone and β''' precipitate connected edge to edge. These phases are connected along the $[0001]_{Mg}$ direction, and the GP zone in this figure extends farther along this direction than the β''' precipitate, as illustrated in **Figure 22c**.

The nucleation of β''' can be inferred from its relationship to the GP zones. It is clear that β''' nucleates heterogeneously on the GP zones at hexagonal rings, as shown in **Figure 22**. The hexagonal rings exist in both the GP zones and the β''' and are consistently located where the two phases connect, suggesting that the strain field at the rings makes it easier for β''' to form. The β''' precipitates might then grow by the so-called ledge mechanism through the nucleation of new $\{010\}_{\beta'''}$ planes.
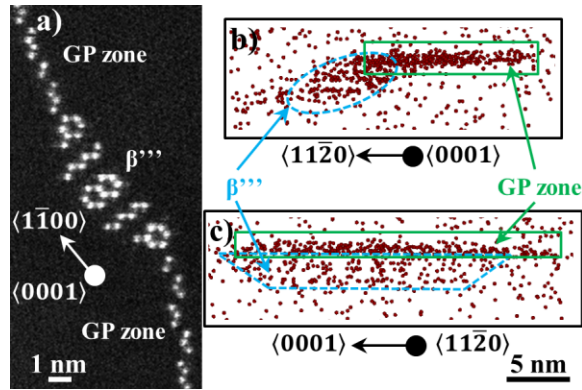
Figure 22: a) HAADF-STEM image of the Mg-0.40 at. % Nd alloy alloy age treated for 16 hours at 200 °C. b) and c) APT data after aging at 250 °C for 3 minutes. Precipitates are viewed along the a) and b) [0001]$_{Mg}$ and <11$\bar{2}$0>$_{Mg}$ zone axes. Reprinted from Ref. [72]

As described in Chapter 2, the β_1 phase has a face-centered cubic crystal structure and forms as plates with habit planes lying parallel to the $\{10\bar{1}0\}_{Mg}$ planes [22]. It was first reported to form in WE alloys and contains particles of β' attached to both ends [5]. The β_1 plates in Mg-Nd are similar to those in WE alloys except instead of having β' particles attached to the ends of the platelets, the β''' phase is attached at those locations [22], as shown in **Figure 23**. How β_1 nucleates has been debated in the literature [6, 27, 58], yet sufficient evidence to support these arguments is still needed.
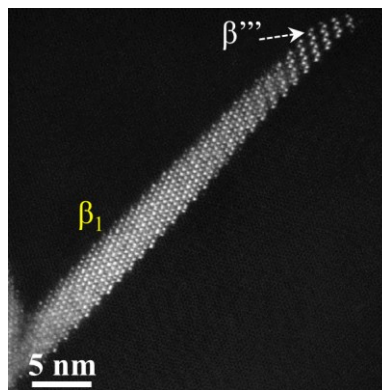
Figure 23: HAADF-STEM image of the Mg-0.40 at. % Nd alloy age treated for 168 minutes at 250 °C with the incident beam parallel to the [0001]$_{Mg}$ direction.
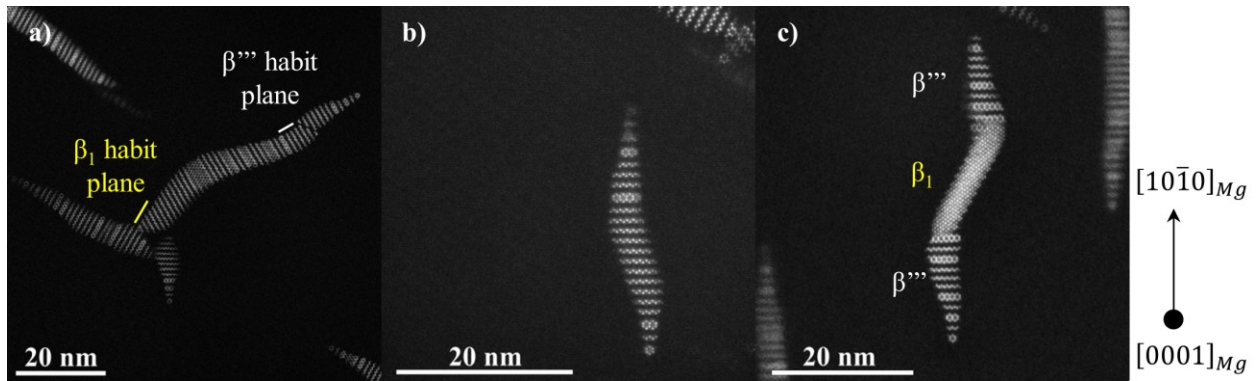
Figure 24: a-c) HAADF-STEM images of the Mg-0.40 at. % Nd alloy age treated for 2 hours at 250 °C with the incident beam parallel to the [0001]$_{Mg}$ direction.

The β''' to β$_1$ transformation is evident from the precipitate shapes and atomic structures observed in the HAADF-STEM images shown in **Figure 24-Figure 26**. Many of the β''' precipitates observed at 1 and 2 hours of aging have noticeably curvy shapes (**Figure 24**) that are not detectable in the size measurements in **Figure 18**. In fact, they are so curvy that one precipitate is often observed to have segments that are on both the β''' and β$_1$ habit planes, as illustrated with one of the arms of the triad arrangement in **Figure 24a**. The structures in **Figure 24b** and **c** are both very curvy, but the structure in **Figure 24b** is all β''' while the structure in **Figure 24c** has a region of β$_1$ in between two β''' precipitates of the same variant. It seems that the cluster in **Figure 24c** was once a single β''' precipitate like the one in **Figure 24b**, but the center region has transformed to β$_1$.
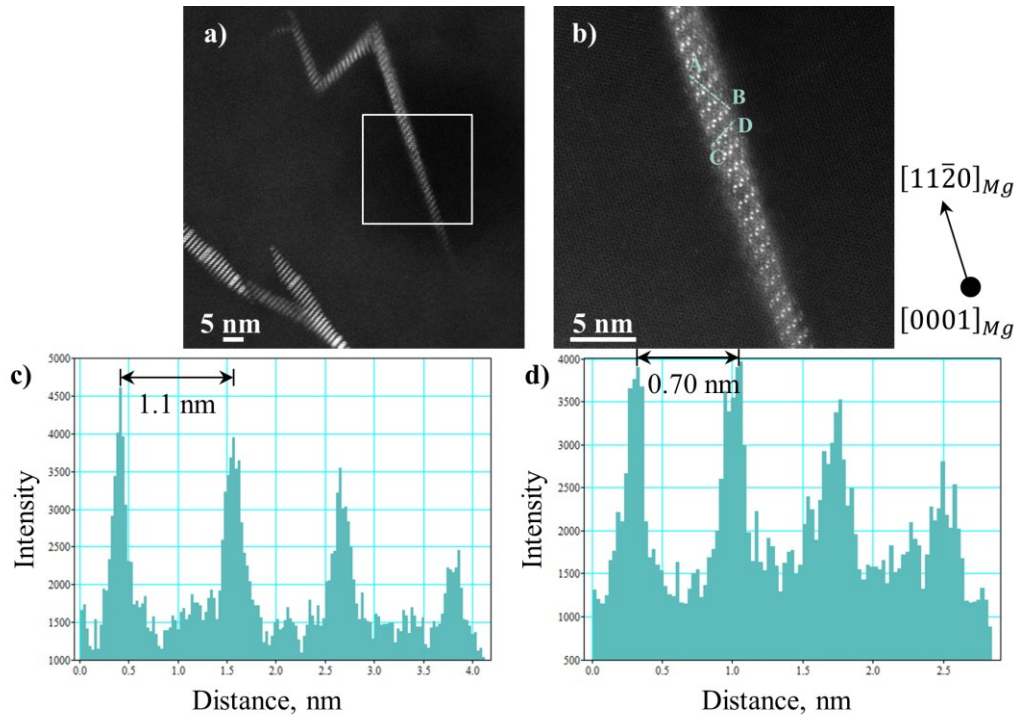
Figure 25: a) and b) HAADF-STEM images of the Mg-0.40 at. % Nd alloy age treated for 168 minutes at 250 °C with the incident beam parallel to the [0001]$_{Mg}$ direction. b) High magnification image of the region within the white box in a). c) and d) Atomic column intensity profiles measured along lines c) AB and d) CD labeled in b)

The microstructure aged for 168 minutes at 250 °C contain many precipitates such as the ones shown in **Figure 25a**. These precipitate platelets lie parallel to $\{1\bar{1}00\}_{Mg}$ planes and are facetted along the $\{1\bar{1}00\}_{Mg}$ planar edges, which are characteristics of the β_1 phase. The main difference between these platelets and the β_1 phase is that the atomic structure of these plates resembles that of β''', where the atomic structure consists of zigzag chains that are each parallel to the neighboring chains and are spaced 1.1 nm apart (**Figure 25b-d**), as expected for the atomic structure of β'''. Interestingly, the platelets typically do not contain the hexagonal rings that are commonly seen in β''', suggesting that the Nd concentration in the plates is 12.5 at. %. Close inspection of the atomic structure of these plates reveal bright and blurry contrast between the zigzag chains (**Figure 25b**), which could indicate that the plates contain another structural feature along the depth of the foil or the lattice is highly strained and could not be focused.
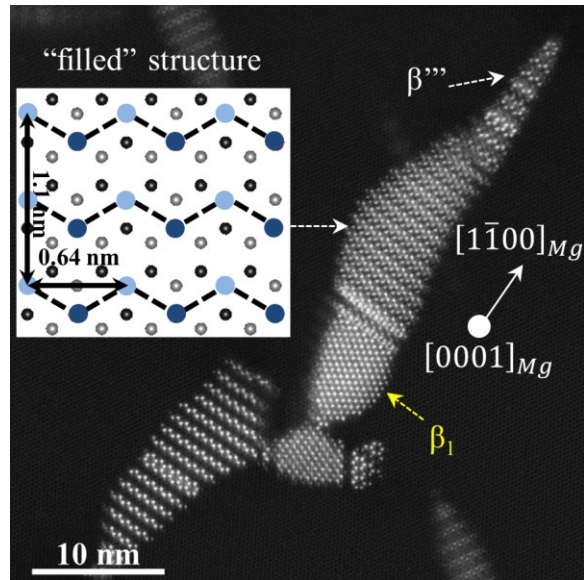
Figure 26: HAADF-STEM image of the Mg-0.40 at. % Nd alloy age treated for 2 hours at 250 °C with the incident beam parallel to the [0001]$_{Mg}$ direction.

In order for the β''' to transform to the β$_1$ phase as suggested in Ref. [27], an extra plane of Nd atoms needs to diffuse between the {010}$_{β'''}$ planes of the β''' phase. **Figure 26** is showing a β''' precipitate with a region containing extra rows of solute elements in between the brighter {010}$_{β'''}$ planes of the β''' phase. A schematic diagram of the atomic structure of the "partially filled" β''' structure is shown in **Figure 26**. Similar to the case of the D0$_{19}$ structure described in **Section 3.3.3**, the partially filled β''' structure (**Figure 26**) is likely a result of stacking defects along the c-axis, however even so, it may indicate how the β$_1$ phase starts to form. For instance, solute atoms can diffuse and attach to the {010}$_{β'''}$ planes at the faulted region, allowing the planes to grow along the [0001]$_{Mg}$ direction. The growth and relaxation of these planes would result in the formation of β$_1$, as suggested in Ref. [27]. The β''' to β$_1$ structural transformation is expected to occur very rapidly; therefore as soon as the filled structure is completed the structure immediately forms into the β$_1$ phase.

Although the nucleation mechanism of β_1 is difficult to identify due to the rate at which it would occur, it is speculated to form from pre-existing β''' plates by an HCP to FCC transformation. Based on the curvy shape of some β''' precipitates and the presence of the β''' atomic structure in plates shaped like β_1 there appears to be a relationship between these two phases. Additionally, β''' precipitates containing regions with a "filled" β''' structure and regions of β_1 are consistent with the structural requirement of having an additional row of zigzag chains within the β''' structure suggested in Ref. [27].

3.4 Conclusions

- The β''' has a non-stoichiometric atomic structure that varies in Nd concentration due to the amount of rows of hexagonal rings and zigzag chains.

- The so-called $D0_{19}$ phase was initially observed along the c-axis and appeared to contain varying contrast that suggested the presence of stacking defects along the c-axis. Analysis of the structure along the $\langle 11\bar{2}0 \rangle_{Mg}$ zones axes confirmed the initial hypothesis that the $D0_{19}$ phase is simply an artifact of stacking defects along the c-axis and does not exist in Mg-Nd alloys. This is in agreement with computational work as reported in [66].

- Quantification of the precipitate shape showed that the overall dimensions of both GP zones and β''' precipitates are in general agreement with elastic strain energy minimization. While the oblong shape in the $[0001]_{Mg}$ direction has been shown to correlate with interacting precipitates, the presence of facets in the $\langle 1\bar{1}01 \rangle_{Mg}$ and $\langle 1\bar{1}02 \rangle_{Mg}$ directions of the β''' precipitates require further work to determine whether these are equilibrium features, the result of overlapping strain fields from neighboring precipitates, or transient characteristics from the growth mechanism. Future models

taking into account the growth mechanism are needed to understand the kinetic effects on the precipitate shape.

- Analysis of the microstructure in the early stages of aging identified heterogeneous nucleation of β''' at the ends of GP zones where both phases are connected along their entire lengths along the c-axis.

- Based on the precipitate shapes and atomic structures, it was speculated that the β_1 phase nucleates from β''' by an HCP to FCC transformation, although direct evidence of the transformation was not observed, presumably due to the rapid rate at which the transformation would occur.

CHAPTER 4:

Precipitation behavior of a Mg-Y alloy during aging at 200 $^{\text{o}}$C

4.1 Introduction

Magnesium rare earth alloys, such as WE43 and WE54, can achieve exceptional strength when age-hardened, making them very attractive for structural applications where weight is an important factor. The primary alloying elements in WE alloys are Y and Nd, however their influence on the precipitation behavior remains unclear, which limits our ability to improve these alloys and design new alloy compositions. Therefore, the analysis of simple binary Mg-Y and Mg-Nd alloys is an effective approach to understanding the chemical and microstructural factors responsible for the formation and evolution of the different phases in complex Mg-RE alloys.

As discussed in the previous chapter, precipitation in binary Mg-Nd alloys has already been well characterized. In the early stages of aging, solute clusters consisting of RE-rich columns of Nd located on Mg lattice sites as short-range ordered arrangements form first [24]. With continued aging, solute clusters are replaced by GP zones that form either chain-like structures or individual hexagonal rings [24, 70]. The β''' phase then forms heterogeneously from GP zones [69] as plates with habit planes lying parallel to the $\{11\bar{2}0\}_{Mg}$ planes and have a varying Nd concentration that depends on the amount of hexagonal rings and zigzag chains in the structure [66, 69]. The β$_1$ phase, which is present in the overaged condition, forms as plates lying parallel to the $\{10\bar{1}0\}_{Mg}$ planes.

48

Compared to Mg-Nd alloys, precipitation in binary Mg-Y alloys is less understood. While Y is excellent for solid solution strengthening [74], it has also been shown to undergo significant precipitation hardening [70]. The precipitation sequence in Mg-Y is currently reported as follows [24, 44, 45, 59]:

Mg-Y: SSSS→solute clusters→GP zones (single monolayers)→β'→β

The early phases in the precipitation sequence of Mg-Y alloys are similar to those found in the Mg-Nd system [22, 24, 26]. Solute clusters consisting of irregular arrangements of Y-rich columns have been observed during initial aging [24]. Continuous monolayer chains aligned parallel to $\{10\bar{1}0\}_{Mg}$ planes, identified as GP zones, were suggested to act as precursors to the β' phase [24]. The shape and atomic structure of the orthorhombic β' phase has been the focus of several studies showing that the precipitates are square-shaped in the basal plane [46, 70] and maintain a stoichiometric configuration controlled by elastic strain energy [75]. An earlier study showed the presence of strand-like features consisting of individual chains of RE elements attached to the corners of β' precipitates, however the details of these features could not be resolved from the image and no discussion was provided. Aside from snapshots of the precipitate microstructure [45], there is also limited information about the evolution of the precipitates with aging. Therefore, in this chapter, APT and HAADF-STEM are used to quantify the evolution of the precipitate microstructure.

4.2 Experimental

The alloy examined in this paper was provided by Magnesium Elektron North America Inc. The composition was measured to be Mg-7.47 wt.% Y (Mg-2.16 at.% Y) by inductively coupled

plasma mass spectrometry. Samples were sectioned, encapsulated in quartz tubes in an argon atmosphere, and solution treated at 560 °C for 24 hours followed by water quenching. Samples were then aged in an oil bath at 200 °C for times ranging between 7 minutes and 5000 hours followed by water quenching. Samples for Vicker's microhardness measurements were mounted in epoxy and ground flat with SiC paper in the following order: 400, 600, 800, and 1200 grit. Mirror finish surfaces were achieved after final polishing with 3 μm and 1 μm diamond suspensions and 0.05 μm colloidal silica. Vickers microhardness measurements were carried out at a load of 100 g and dwell time of 15 seconds. Samples for TEM analysis were prepared either by twin-jet electropolishing using the method described in Ref. [13] or using focused-ion beam (FIB). Micrographs were taken using a JEOL 2100F operated at 200 kV with a collection angle of 52 mrad and a double-corrected JEOL 3100R05 microscope operated at 300 kV with a collection angle of 74 mrad. The thickness of the TEM foils were measured from electron energy loss spectra using a JEOL 3100R05 microscope in STEM mode with a convergence semiangle of 22 mrad and a collection semiangle of 11 mrad. APT specimens were prepared by electropolishing with a solution of 25% perchloric acid in acetic acid using 14-20 V for rough polishing and 2% perchloric acid in butoxyethanol with 5-10 V for fine polishing. APT experiments were performed using a Cameca LEAP 5000 instrument operated in voltage pulsing mode at 200 kHz with voltage pulse amplitude equal to 20% of the applied DC voltage. Specimens were maintained at a temperature of 50 K and the voltage was automatically increased to maintain a constant evaporation rate of 0.01 atoms/pulse. Data reconstructions and analyses were carried out using the Integrated Visualization and Analysis Software (IVAS 3.6.12) package. The reconstruction parameters (geometric factor and image compression factor) were chosen to ensure that the planar spacings observed at identified poles and the angles

between such planes match that of the hexagonal magnesium matrix. The evaporation field was selected to be that of Mg at 21 V/nm [67].

The β' precipitates were measured from STEM images using ImageJ [76]. The length along $[0001]_{Mg}$ and $\langle 10\bar{1}0 \rangle_{Mg}$ directions were measured directly while the dimension along $\langle 11\bar{2}0 \rangle_{Mg}$ directions was measured by taking the area of each β' precipitate in the basal plane and dividing it by the length along the $\langle 10\bar{1}0 \rangle_{Mg}$-type direction to get an effective width. The area measurements did not take into consideration the few long Y-rich zigzag chains that extended much longer than the other $\{010\}_{\beta'}$ planes.

A major concern in the quantitative analysis of precipitate dimensions is the possible sectioning due to the limited TEM foil thickness. The TEM samples were made so that minimal tilt would be required to reach the desired zone axis. Since the sizes of the precipitates in the basal plane are much smaller than the foil thicknesses, the lengths along $\langle 11\bar{2}0 \rangle_{Mg}$ and $\langle 10\bar{1}0 \rangle_{Mg}$-type directions are not significantly affected by the tilting of the sample. In addition, the β' precipitates in Mg-Y are rectangular prisms when viewed down the c-axis, therefore, as long as the edge of the foil cuts perpendicular to the dimension being measured then the measurements from the projected precipitate will match the size of the uncut precipitate. The length along the c-axis is more likely to be affected by the finite thickness of the TEM sample. Using the foil thickness and tilting angle needed to reach the desired zone axis, the longest possible length the precipitates could have along the $[0001]_{Mg}$ direction was calculated for each sample and compared to the longest measured precipitate length along $[0001]_{Mg}$ for each aging time. Since these were much less than the longest possible length, it was assumed that the size of the precipitates along the c-axis was not limited by the finite thickness of the TEM foil.

51

Regarding the number density of precipitates, a probability factor needed to be taken into account to correct for the finite thickness of the foil. The following expression was used to calculate the corrected number density of precipitates at each aging time:

$$\text{Equation 1 } N_C = N_M \frac{t}{t+L}$$

where, N_C =corrected number density of precipitates, N_M =measured number density of precipitates, t=foil thickness (measured from EELS), and L=average length of precipitates along the $[0001]_{Mg}$ direction. The uncertainty in N_C was calculated using error propagation rules and is given by the following expression:

$$\text{Equation 2 } \Delta N_C = N_C \sqrt{\left(\frac{\Delta N_M}{N_M}\right)^2 + \left(\frac{\Delta z}{\frac{1}{1+\frac{L}{t}}}\right)^2}$$

$$\text{Where, } \Delta z = \frac{1}{1+\frac{L}{t}}\left(\frac{\Delta y}{1+\frac{L}{t}}\right) \text{ and } \Delta y = \sqrt{1 + \left(\frac{L}{t}\sqrt{\left(\frac{\Delta L}{L}\right)^2 + \left(\frac{\Delta t}{t}\right)^2}\right)^2}$$

The Δ(N_C, N_M, L, and t) terms are the standard deviations for each measurement. The values of N_C and the associated measurement error are provided in **Table 1**.

A two-dimensional model of a square-shaped inclusion in a matrix was simulated using the COMSOL Multiphysics 5.2a software package [77] to understand the strain energy distribution in and around a single β' precipitate in Mg-Y alloys. A plane stress condition was assumed and the boundary edges were fixed. The values used for the matrix elastic constants were reported in Ref. [46] and are C_{11}=63.5, C_{12}=24.85, C_{13}=20.0, C_{33}=66, and C_{44}=19.3 (GPa). The elastic constants used for the β' precipitate are C_{1111}=78.8, C_{2222}=62.9, C_{3333}=65.6, C_{1122}=24.6,

C_{2233}=19.9, C_{3311}=23.1, C_{1212}=11.9, C_{2323}=11.6, and C_{3131}=8.46 (GPa) (unpublished data by Anirudh Natarajan, UCSB). The following strain was also obtained from Ref. [46] and was applied to the inclusion.

$$\varepsilon = \begin{pmatrix} 0.0299 & 0 & 0 \\ 0 & 0.0183 & 0 \\ 0 & 0 & -0.00273 \end{pmatrix}$$

4.3 Results

4.3.1 Hardness and microstructural evolution

The Mg-Y alloy experienced significant age hardening during aging at 200 $^{\circ}$C. The microhardness increased immediately upon aging and remained stable until about 100 hours at which point hardness abruptly increased again and reached a maximum after about 2500 hours. Further aging for 5000 hours resulted in a decrease in hardness as the alloy was overaged (**Figure 27**).
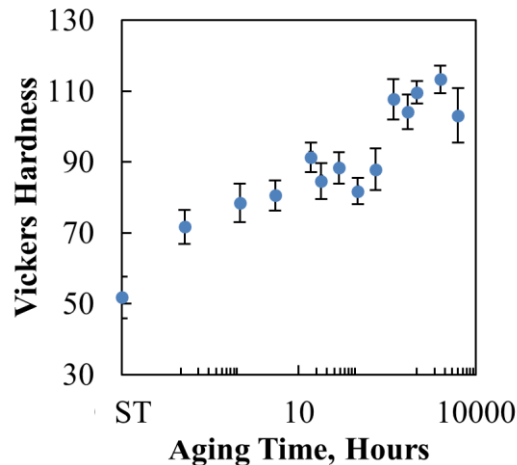
Figure 27: Hardness curve for a Mg-2.16 at. % Y alloy aged at 200 $^{\circ}$C. ST represents the solution treated condition. Reprinted from [70]

Concomitantly with hardness, the microstructure was characterized in detail. The Y spatial distribution in the alloy after aging for 24 hours at 200 ^{o}C was characterized using APT, while the microstructures after aging for 200, 400, 1000, 2500, and 5000 hours were analyzed using HAADF-STEM. When aged for 24 hours, the APT reconstruction showed a uniform distribution of Y and no secondary phases were detected, as shown in **Figure 28**, yet the alloy experienced an increase in hardness. Small solute clusters are expected to have formed based on previous HAADF-STEM observations [24], however these clusters were indistinguishable within the APT data. Between 200 and 400 hours of aging, the alloy underwent a second increase in hardness, which appeared to correspond to an increasing number density of β' precipitates (**Figure 29a, b**). Initially, the precipitates were isolated and uniformly distributed. By 1000 hours, the individual precipitates began to connect, either directly to other β' precipitates or by the strands, forming a cellular-like network of β' precipitates (**Figure 29c-e**). The average diameter of these cells increased from 124±5 nm at 2500 hours to 147±9 nm at 5000 hours of aging, while the individual β' precipitates within the cells did not noticeably change size. The average diameter of the cell structures at 2500 hours and 5000 hours were measured using the line intercept method [78] on STEM images at magnifications of 80-150K.

Another phase that had not been previously reported in the Mg-Y system was observed between 200 and 5000 hours. This phase formed as thin plates on the basal plane and its identification is further discussed in **Section 7.2.2**.
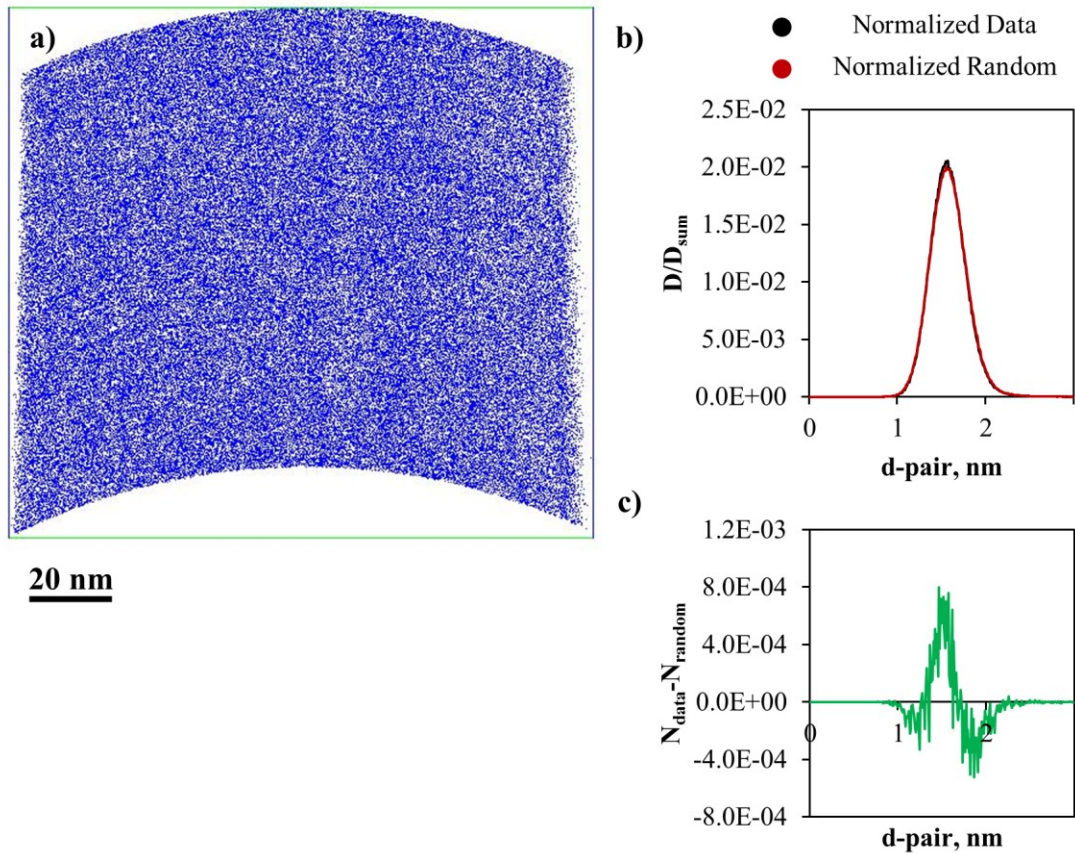
Figure 28: a) Slice from larger three-dimensional APT reconstruction from a Mg-2.16 at. % Y alloy aged for 24 hours at 200 °C with only the Y atoms being shown (slice thickness is 20 nm). b) Nearest neighbor distribution created using Y, maximum d-pair=3 nm, sample width d-pair=0.01 nm, and order=10 ions. The y-axis (D/D$_{sum}$) is normalized by dividing the data by the total sum of the data for both the reconstructed and randomized data. c) Plot of the normalized reconstructed data minus the normalized random data.
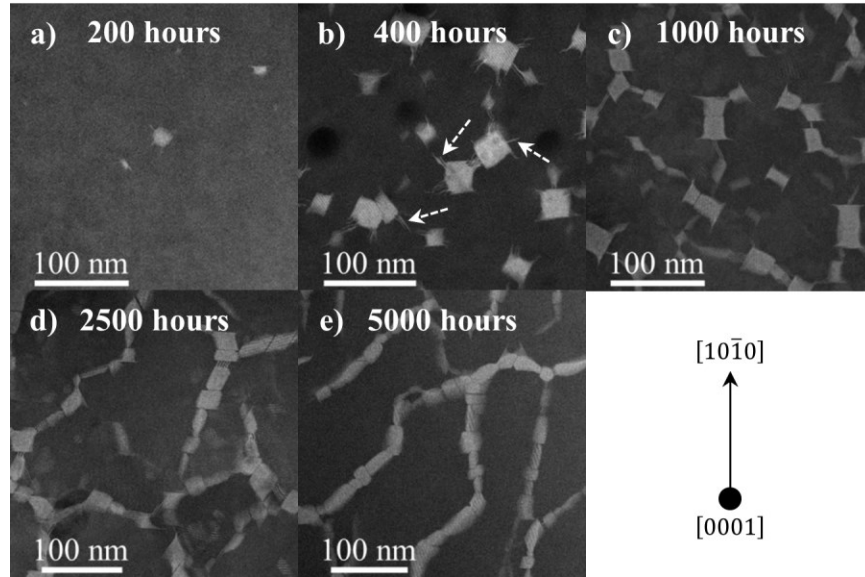
Figure 29: HAADF-STEM images of the microstructure of the Mg-2.16 at. % Y alloy after being aged at 200 °C for different aging times with the incident beam parallel to the [0001]$_{Mg}$ zone axis. The crystallographic orientations for each image are shown in the bottom right corner of the image.

Some of the β' precipitates were decorated with Y strands attached mainly at the corners and some $\{1\bar{1}00\}_{Mg}$ planar edges, as indicated with arrows in **Figure 29b**, and were present at all aging conditions analyzed (200-5000 hours). The strands consisted of three main atomic structures, as shown in the STEM images in **Figure 30** and **Figure 31**. **Figure 31** shows high magnification images of the different strands labeled in **Figure 30**. Each one consists of individual zigzag chains of Y-rich columns lying parallel to $\{10\bar{1}0\}_{Mg}$ planes. They appeared to be identical to the individual $\{010\}_{\beta'}$ planes of the β' phase such that the Y-rich columns sit on Mg lattice sites in a triangular pattern. The first structure was simply a single zigzag chain connected to one of the $\{010\}_{\beta'}$ planes of a β' precipitate and is labeled "b" in **Figure 30**. The second structure could be thought of as the β' structure missing the middle, inverted $\{010\}_{\beta'}$ planes so that the structure contains two or more parallel zigzag chains separated by eight Mg lattice spacings along the $\langle 1\bar{1}00 \rangle_{Mg}$-type directions (labeled "c" in **Figure 30**). The third structure consisted of two or more zigzag chains that were each separated by one Mg lattice

56

spacing along a $\langle 1\bar{1}00\rangle_{Mg}$ direction and were staggered with respect to the adjacent chains when viewing the basal plane (labeled "d" in **Figure 30**). Each chain was out-of-phase or inverted with respect to the adjacent chains, creating a hexagonal ring where these two chains "connect". Due to the two-dimensional nature of TEM, it was unclear how these two chains are connected along the c-axis. The structures of the strands in the isolated β' precipitates (**Figure 30)** were the same as those attached to the β' precipitates in the cell structure (**Figure 31**), however the presence and location of these strands was different. In general, isolated β' precipitates had strands attached to all four corners (**Figure 29b**), whereas the β' precipitates in the cell structure only contained strands that connect two β' precipitates (**Figure 29d** and **e**).
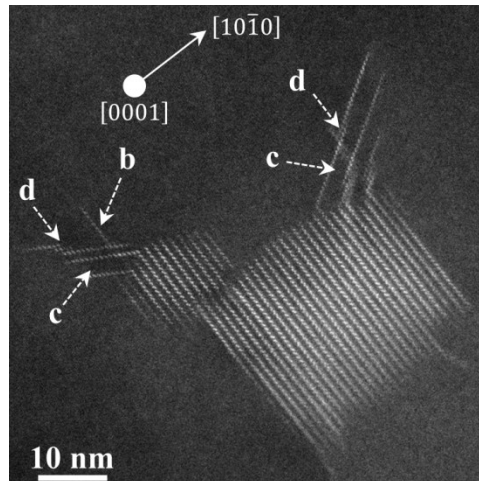
Figure 30: HAADF-STEM image showing the strand structures. The structures labeled b-c correspond to similar structures as those shown in Figure 31b-c. The incident beam is parallel to the [0001]$_{Mg}$ zone axis.
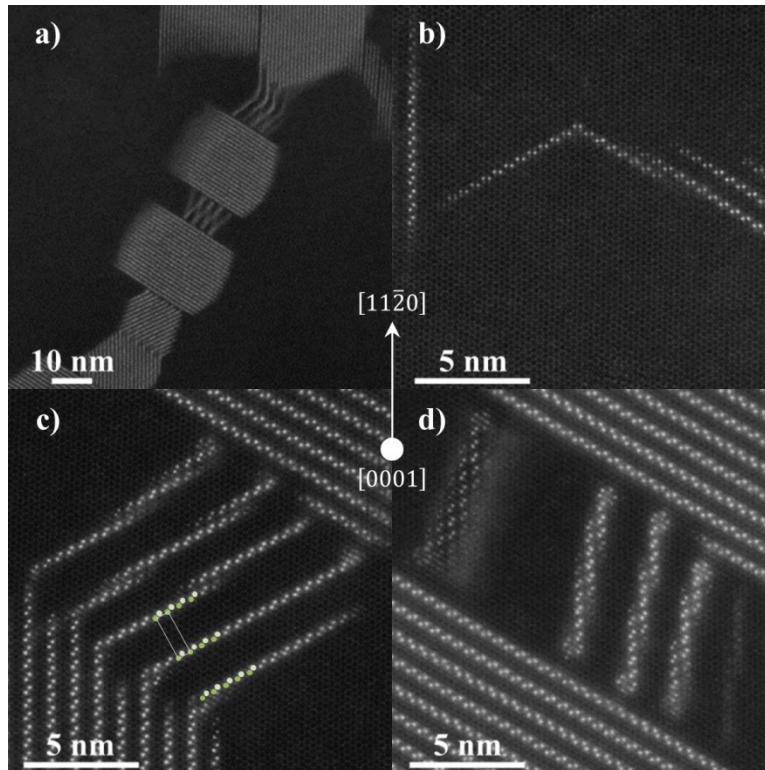
Figure 31: HAADF-STEM images showing the a) strand structures connecting β' precipitates in the cell structure and b-d) low mag images of the different strand structures. The box in c) outlines a single unit cell of the second strand structure. Green circles are overlaid on the Y-rich columns of the structure in c). The incident beam is parallel to the [0001]$_{Mg}$ zone axis.

4.3.2 β' characteristics and evolution

4.3.2.1 β' morphology

The shape of the β' precipitates in the basal plane underwent subtle changes with aging time while the shape in the $\{11\bar{2}0\}_{Mg}$-type planes is independent of aging time. Between 200 and 400 hours of aging at 200 °C, the majority of the β' precipitates had equiaxed shapes in the basal plane such that their dimensions along $\langle 11\bar{2}0\rangle_{Mg}$ and $\langle 10\bar{1}0\rangle_{Mg}$ directions were equivalent. In general, the precipitates were square-shaped with all four edges being relatively flat (**Figure 29b**), although few precipitates appeared rounded (**Figure 32a**). By 1000 hours, many of the precipitates had developed slightly concave $\{11\bar{2}0\}_{Mg}$ planar edges, resulting in bell- and

58

hourglass-shaped precipitates (**Figure 32b**). After aging for 2500 hours when the microstructure contained primarily the cellular-like structure, many precipitates had irregular shapes such that they were noticeably longer along $\langle 10\bar{1}0 \rangle_{Mg}$ directions than along $\langle 11\bar{2}0 \rangle_{Mg}$ directions (**Figure 29c-e**). When viewed along the $\langle 11\bar{2}0 \rangle_{Mg}$ zone axes the β' precipitates appeared elongated and facetted along the c-axis **Figure 32c**. They also contained irregular facets at the ends that did not consistently lie on a certain set of planes.
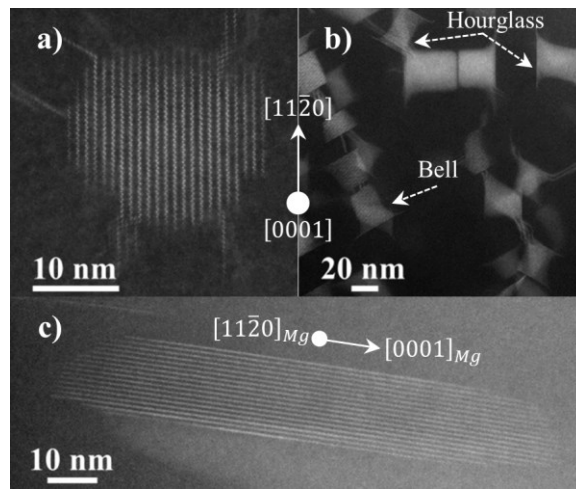
Figure 32: HAADF-STEM images of β' precipitates obtained along a) and b) [0001]$_{Mg}$ and c) <11$\bar{2}$0>$_{Mg}$ zone axes.

The shape evolution of the β' precipitates was quantified using HAADF-STEM by measuring their size along $[0001]_{Mg}$, $\langle 11\bar{2}0 \rangle_{Mg}$, and $\langle 10\bar{1}0 \rangle_{Mg}$ directions after aging for 200, 400, and 1000 hours at 200 °C and the results are presented in **Figure 33**. The size of the β' precipitates between 200 and 400 hours of aging increased along all three dimensions (**Figure 33a-c**) with the length along the $[0001]_{Mg}$ direction being the longest. After 400 hours, the size does not noticeably change. As a first approximation, the precipitates at 200 and 400 hours of aging were square-shaped. The precipitates at 1000 hours showed a slight elongation along $\langle 10\bar{1}0 \rangle_{Mg}$ directions. The aspect ratio in the $\langle 11\bar{2}0 \rangle_{Mg}$ view seemed to change between 200 and 400 hours

with precipitates growing faster along the c-axis than in the $\langle 10\bar{1}0\rangle_{Mg}$ directions. However, we note that there was significant scatter in the data of **Figure 33**, therefore, more data would be needed in order to derive a quantitative description of the shape change.
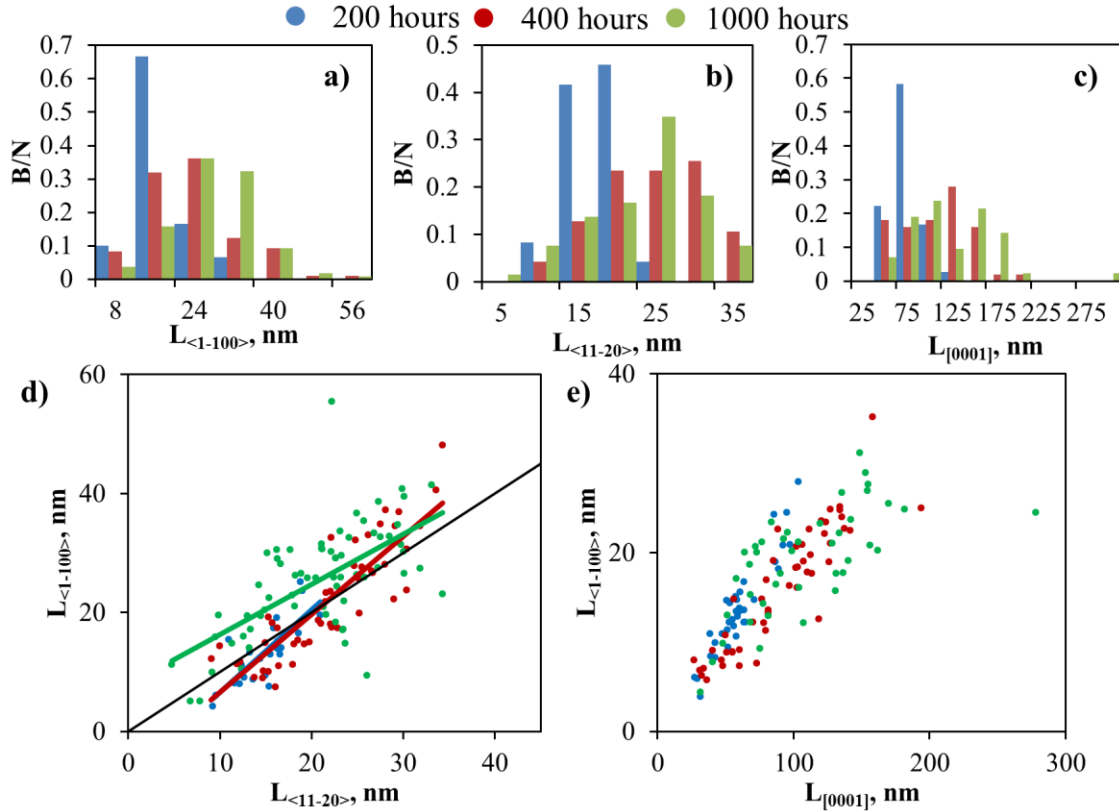
Figure 33: a)-c) Size distribution plots of β' along the three principle axes and d) & e) plots of the $L_{<1\bar{1}00>}/L_{<11\bar{2}0>}$ and $L_{<1\bar{1}00>}/L_{[0001]}$ aspect ratios of β' at 200 (blue), 400 (red), and 1000 (green) hours of aging. B/N is the number of precipitates in each bin (B) divided by the total number of precipitates in the distribution (N). The black line in d) indicates precipitates with a square shape.

4.3.2.2 Number density of β'

The number density of β' was measured at 200, 400, 1000, 2500, and 5000 hours of aging at 200 °C (**Table 1**). The number density of β' increased sharply from 200-400 hours, translating into a sharp increase in hardness (**Figure 27**). Concomitantly, precipitate size also increased. From 400-1000 hours, while the number density increased slightly and average size did not change, the

most significant change was the spatial rearrangement of the precipitates into a cell structure. From 1000 to 5000 hours, the number density of β' precipitates remained constant. Note that the number density measurements plotted in **Table 1** were averaged over two to eight images for each aging condition and were only measured from images taken along the $[0001]_{Mg}$ zone axis.

Table 1: Average precipitate size along the three principal axes and number density of β' with aging.

Aging time (hours)	200	400	1000	2500	5000
Number density (/m^3)	(6.9±3.3)x10^{20}	(3.3±1.2)x10^{21}	(4.5±1.2)x10^{21}	(5.6±2.6)x10^{21}	(4.8±1.4)x10^{21}
$L_{<10-10>}$ (nm)	14±5.2	19±8.8	23±8.6	19±6.8	20±6.1
$L_{<11-20>}$ (nm)	15±3.0	22±6.4	21±6.8	-	-
$L_{[0001]}$ (nm)	60±19	91±38	109±47	-	-

The error on the number density was measured using error propagation rules as described in the experimental section. The error on the size measurements is the standard deviation for each measurement.

4.4 Discussion

The aging behavior of the binary Mg-Y alloy exhibits a number of similarities with previously studied Mg-Nd or Mg-Gd alloys. In all three alloy systems, β' or β''' precipitate composition, structure, morphology, and spatial distribution are controlled by elastic strain energy that develops as a result of the formation of misfitting coherent precipitates. The dominance of strain energy in these systems leads to non-classical aging behavior.

The atomic structure of the β' phase observed in the Mg-Y alloy is the same as the β' phase forming in Mg-Gd alloys [14], but differs from the β''' structure in Mg-Nd alloys [22]. These differences were previously rationalized in terms of transformation strains that strongly depend on precipitate composition [66, 75]. The β''' phase can have a Nd concentration between 12.5 at. % and 16.7 at. % Nd that is consistent with the overall misfit strain being lowest within this range. Increasing the Nd concentration above this range would result in a corresponding

increase in the misfit strain along $\langle 10\bar{1}0 \rangle_{Mg}$ (or y-axis) directions. Similarly, the stoichiometric β' phase has a single Y concentration of 12.5 at. % and any increase in the Y concentration through the formation of rings would result in an overall increase in the misfit strain along both $\langle 10\bar{1}0 \rangle_{Mg}$ (or y-axis) and $\langle 11\bar{2}0 \rangle_{Mg}$ (or x-axis) directions.

Prior to 200 hours, only fine clustering of Y is observed without any obvious long-range ordering [24]. Rather than heterogeneous nucleation on strands as previously suggested [24], we argue that β' nucleates from small Y-rich clusters. The significant density of clusters could certainly give rise to apparent homogeneous nucleation of β'. This is in contrast with the Mg-Nd system where distinct GP zone structures with heterogeneous nucleation of β''' were observed [22, 26]. The lack of isolated strands in the Mg-Y alloy supports the proposed hypothesis. The presence of strands connected to the β' precipitates is rationalized in terms of the strain energy that concentrates around the coherent β' precipitates particularly at the corners where strands are most often observed. In support of this argument, the elastic strain energy distribution in and around a β' precipitate was modeled using Finite Element Analysis, as shown in **Figure 34**. The parameters used for the calculation are reported in **Section 4.2**. This behavior is similar to that observed in other alloys that contain β' precipitates such as Mg-Gd [15] and Mg-Y-Nd [70], which tend to form long chains consisting of β' precipitates connected to β''' platelets in alternating order. Their presence is also believed to be the result of elastic strains developing at the precipitate corners [15].
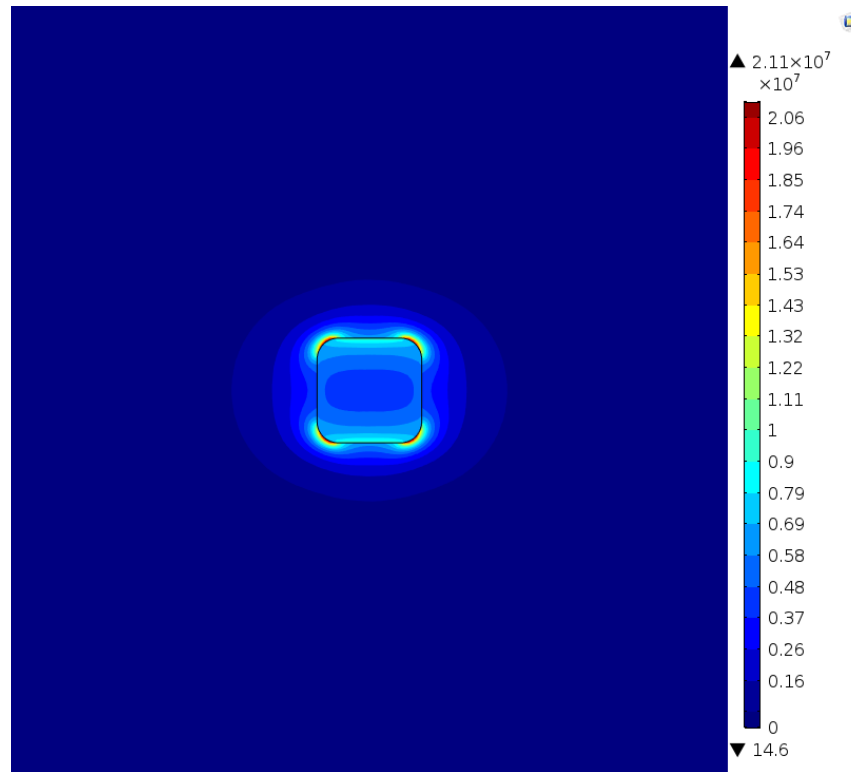
Figure 34: Elastic strain energy distribution around a square-shaped inclusion

Assuming thermodynamic equilibrium, the morphology of coherent precipitates is controlled by a combination of interfacial and elastic strain energies. A previous phase field study used different combinations of interfacial and elastic strain energies to model the two-dimensional shape of β' in Mg-Y in the basal plane [46]. The modeled shape was most representative of the actual shape of β' when both interfacial and elastic strain energies were used, but since the interfacial energy values were low, a negligible effect from the interfacial energy is expected. Instead, the relative dimensions of the needle-shaped β' precipitates (**Figure 33**) are consistent with previously calculated misfit strains [75]. The transformation strains are highest and similar in magnitude along $\langle 10\bar{1}0 \rangle_{Mg}$ and $\langle 11\bar{2}0 \rangle_{Mg}$ directions and lowest along the $[0001]_{Mg}$ direction, which agrees with the precipitates being equiaxed in the basal plane and elongated along the c-axis. Although the previously calculated misfit strains are consistent with the general

shape of the β' phase in Mg-Y alloys, they do not explain the concave and irregular shapes also observed, leaving to question whether these shapes are characteristic of the equilibrium shape or transient growth features. The shapes of β' transition from being primarily squares (with sharp and rounded corners) to a combination of squares, concave squares/rectangles, and irregular shapes. Like the β''' phase in Mg-Nd alloys [71, 72], it is reasonable to expect interacting strain fields from neighboring precipitates to alter the morphology of β' as these precipitates are often close in proximity or even contacting neighboring precipitates. The effect of neighboring precipitates on precipitate shape is illustrated in **Figure 35** where growth of the β' precipitate labeled "A" along $\langle 10\bar{1}0\rangle_{Mg}$ directions is blocked by precipitates labeled "B" and "C" that have $\{010\}_{\beta'}$ planes that are out-of-phase with those in precipitate A, while growth along a $\langle 11\bar{2}0\rangle_{Mg}$ direction is limited due to elastic strain energy constraints. On the other hand, the β' precipitate labeled "D" shown in **Figure 35** seems to have either grown preferentially along a $\langle 10\bar{1}0\rangle_{Mg}$ direction or coalesced with multiple in-phase β' precipitates in order to reduce the elastic strain energy. This type of multiparticle interaction driven by minimizing elastic strain energy is reminiscent of that observed in Ni-based superalloys where the evolution of the γ' morphology strongly depends on the amount and proximity of precipitates in the microstructure [79]. In addition to irregular shapes, some β' precipitates develop concave $\{11\bar{2}0\}_{Mg}$ planar edges, resulting in bell- and hourglass-shaped precipitates that are also similar to those previously observed for the γ' phase in Ni-based alloys [80]. In the case of γ' precipitates in Ni-based superalloys, the concavity was shown to form as a result of faster growth kinetics at the corners than along the edges [80]. Therefore, it seems that the strands attached to the corners of the β' provide additional solute to the growth at the corners, which agrees with the concave shapes having fewer strands. Nonetheless, further analysis of the microstructure at longer aging times

and modeling of the shape evolution may be necessary to confirm the equilibrium structure, the role of strain field interactions, and the stability of concave interfaces.
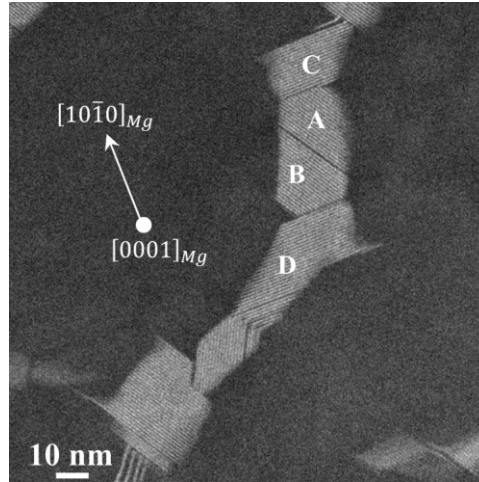
Figure 35: HAADF-STEM micrograph of the Mg-2.16 at. % Y alloy aged for 5000 hours at 200 °C. The incident beam is parallel to the [0001]$_{Mg}$ zone axis.

In addition to the precipitate shapes, the rearrangement of precipitates into a cell structure is also driven by minimizing elastic strain energy. Unlike the precipitates of the cell structures in Mg-Gd alloys [15], the evolution of β' in Mg-Y does not follow normal Ostwald ripening driven by the minimization of interfacial energy. Rather it seems to undergo strain-induced patterning that maintains significant interfacial area, similar to the γ' phase in Ni-based superalloys [79] where the formation of the cell structure is a result of multiparticle interactions. In contrast to alloys that contain the β' phase, Mg-Nd alloys do not form the cellular structure of precipitates. Given the difference in shape between β''' and β', elongated plates versus squares, we hypothesize that the strain distribution created around the square-shaped precipitates is more conducive for developing a cell structure, and future continuum models of the precipitate shapes will confirm this idea. Due to the increase in aspect ratio associated with the connected precipitates, the cell structure is expected to improve the mechanical properties of these alloys by acting as better

barriers to moving dislocations compared to isolated precipitates. Finally, further analysis of the microstructure at longer aging times is necessary to determine whether the β' precipitates will eventually coarsen, dissolve into the matrix, or transform to another phase.

4.5 Conclusions

The aging and precipitation behavior of a Mg-Y alloy at 200 °C was characterized using scanning transmission electron microscopy and atom probe tomography. The following conclusions were reached:

- Precipitation strengthening during aging at 200 °C is obtained by forming a high density of β' precipitates.

- The β' phase appears to nucleate homogeneously in the Mg matrix.

- The strain distribution around β' precipitates favors the formation of strands attached to the precipitate corners. These strands are made up of different arrangements of single zigzag monolayers of Y-rich columns.

- The shape of the β' precipitates is consistent with minimizing elastic strain energy that leads to precipitates that are square-shaped in the basal plane and elongated along the c-axis. The basal cross section is affected by neighboring precipitates and can become more elongated in the basal plane. The concave β' precipitates are likely a result of faster growth kinetics at the corners.

- The evolution of β' precipitates does not initially follow classical aging behavior driven by interfacial energy minimization, but rather is controlled by strain energy minimization, leading to a cellular arrangement of interconnected β' precipitates that do not appear to increase in size with aging.

CHAPTER 5:

Deformation behavior of β' and β''' in Mg-RE alloys[2]

5.1 Introduction

During low temperature aging, magnesium rare earth (RE) alloys form a high density of nanoscale precipitates that increase alloy strength. In Mg-Nd alloys, the precipitation sequence follows [2, 20-22, 26, 29]: SSSS→GP zones→β''' (see Chapter 3)→β_1→β_2→β→β_e, where the coherent β''' phase nucleates heterogeneously from the GP zones and β_1 forms as plates with habit planes parallel to the $\{10\bar{1}0\}_{Mg}$ planes. In Mg-Y, the precipitation sequence follows [2, 24, 45, 59]: SSSS→solute clusters→single zigzag monolayers→β'→β, where the metastable β' phase has an equiaxed shape in the basal plane [81]. Microstructure observations concomitant with hardness measurements show that the β''' phase in Mg-Nd (see Chapter 3) and β' phase in Mg-Y [2, 82] (see Chapter 4) were responsible for the hardness increase up to peak aging, while β_1 formed during overaging. Alternatively, a previous report on a WE54 alloy attributed the increase in hardness to β_1 [73]. While β_1 precipitates may contribute to strengthening WE alloys, the β''' and β' phases also have a significant strengthening effect and must be considered when developing strengthening models and designing optimal alloy microstructures.

Interest in Mg-RE alloys comes from the fact that β''', β', and β_1 all lie parallel to prismatic planes, and as such, they are thought to be more efficient in blocking dislocation motion than basal plane precipitates [1, 64]. However, precipitation strengthening is controlled by a number of other factors, including precipitate shape, number density, size, and dislocation interaction mechanism. Theoretical evaluations of the strengthening behavior of β_1 precipitates interacting with basal [1] and non-basal [64, 65] slip were developed based on the assumption that an Orowan mechanism operates. In the case of β''' and β' however, considering their high degree of interface coherency and hcp-based crystal structures, a shearing mechanism is highly likely. In fact, whether the precipitates in Mg-RE alloys are shearable has not been experimentally determined, weakening the validity of quantitative predictions of the strengthening behavior based solely on an Orowan strengthening model. Consequently, the present study uses high-angle annular dark-field (HAADF) scanning transmission electron microscopy (STEM) to determine the behavior of β''' and β' phases in Mg-Nd and Mg-Y during deformation by analyzing precipitate structures before and after deformation.

5.2 Experimental

The alloys examined in this work were provided by Magnesium Elektron North America Inc. The compositions were measured using inductively coupled plasma mass spectrometry and determined to be Mg-0.40 at. % Nd and Mg-2.16 at. % Y. Samples were sectioned, encapsulated in an argon atmosphere, and solution treated at 560 °C for 24 hours followed by water quenching. Samples were then aged in an oil bath at either 200 °C for 400 hours (Mg-Y) or 250 °C for 2 hours (Mg-Nd) followed by water quenching. Compression tests using an Instron testing system were performed on 3x3x6 mm samples with an applied stress of 220 MPa.

Samples for STEM imaging were prepared by using either the method described in Ref. [13] or using a liftout method and focused-ion beam (FIB) milling. STEM images were taken using a JEOL 2100F operated at 200 kV with a collection angle of 52 mrad and a double-corrected JEOL 3100R05 microscope operated at 300 kV with a collection angle of 74 mrad.

5.3 Results and Discussion

Upon aging Mg-Nd alloys at temperatures between 150 and 250 $^{\circ}$C, β''' precipitates form as elongated platelets with the shortest dimension along $\langle 11\bar{2}0 \rangle_{Mg}$-type directions and longest dimension along $[0001]_{Mg}$ directions, resulting in plate-shaped precipitates with $\{11\bar{2}0\}_{Mg}$ habit planes (see Chapter 3). STEM images obtained along $[0001]_{Mg}$ (**Figure 36a**) and $\langle 11\bar{2}0 \rangle_{Mg}$ (**Figure 36b** and **c**) zone axes show typical β''' precipitates formed in the aged Mg-Nd alloy. The β''' phase has a primitive orthorhombic crystal structure with the Nd atoms of the phase lying on Mg lattice positions such that its interface is coherent with the Mg matrix. The atomic structure contains zigzag chains and rows of hexagonal rings that lie parallel to $\{10\bar{1}0\}_{Mg}$ planes [22]. Oftentimes precipitates in undeformed alloys contain stacking defects consisting of individual hexagonal rings that are staggered along the c-axis, causing the defected region of the precipitate to have an apparent $D0_{19}$ structure when viewed along the c-axis (**Figure 36a**), as described in **Section 3.3.3**.
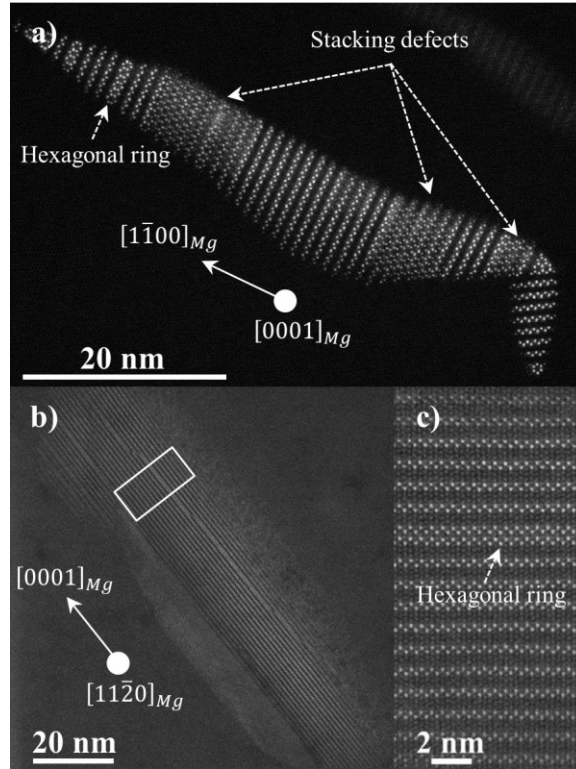
Figure 36: HAADF-STEM images of the Mg-0.4 at. % Nd alloy aged for 2 hours at 250 °C with the incident beam parallel to the a) $[0001]_{Mg}$ and b) $<11\bar{2}0>_{Mg}$ zone axes. c) High magnification image of the region within the white box in b).

STEM images of β''' precipitates after compression of the aged Mg-Nd alloy are shown in **Figure 37**. The precipitate in **Figure 37a** has been sheared multiple times by dislocations as multiple portions of the precipitate were displaced along $\langle 11\bar{2}0 \rangle_{Mg}$ directions with respect to each other. The above mentioned stacking defects (**Figure 36a**) are clearly different from the defects caused by dislocation shearing that cuts an entire precipitate into two halves. The displacement shown in **Figure 37a** involved multiple dislocations with a Burger's vector component along one of the $\langle 11\bar{2}0 \rangle_{Mg}$ directions. Another precipitate along a $\langle 11\bar{2}0 \rangle_{Mg}$ zone axis shows clear deformation lines extending across the length of the precipitate along a $\langle 10\bar{1}0 \rangle_{Mg}$ direction (**Figure 37b** and **c**). Images from both views are evidence for β''' precipitates shearing by basal plane dislocations along $\langle 11\bar{2}0 \rangle_{Mg}$ directions.

70
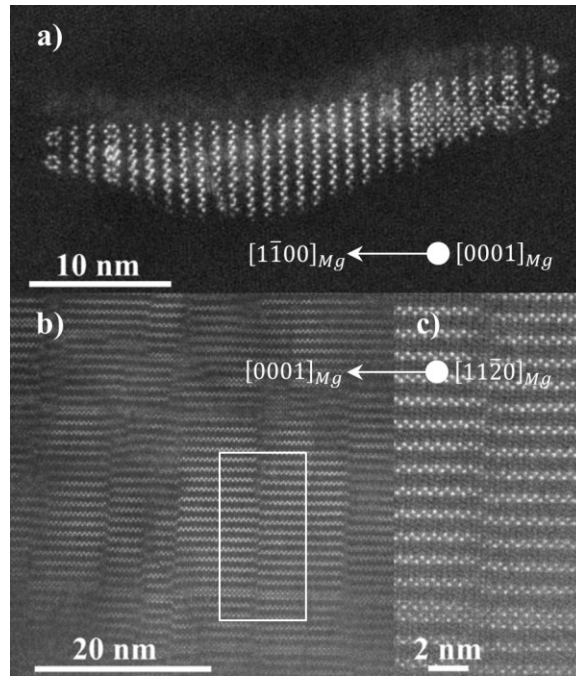
Figure 37: HAADF-STEM images of the Mg-0.4 at. % Nd alloy aged for 2 hours at 250 °C and deformed with the incident beam parallel to the a) [0001]$_{Mg}$ and b) <11$\bar{2}$0>$_{Mg}$ zone axes. c) High magnification image of the region within the white box in b).

In the Mg-Y alloy, the β' phase has a different atomic structure and shape than the β''' phase in Mg-Nd. STEM images of β' precipitates were obtained after aging for 400 hours at 200 °C (**Figure 38**). As previously determined, the β' phase has a stoichiometric, base-centered orthorhombic crystal structure containing only zigzag chains that are each out of phase with the neighboring chains and its interface is perfectly coherent with the Mg matrix [2, 45]. The β' phase has a square-shaped cross section in the basal plane, and are elongated in the [0001]$_{Mg}$ direction, resulting in needle-shaped precipitates [45]. There is no evidence of stacking defects in the pre-deformed precipitates (**Figure 38**).

71

$[11\bar{2}0]_{Mg}$←●$[0001]_{Mg}$ $[0001]_{Mg}$←●$[11\bar{2}0]_{Mg}$
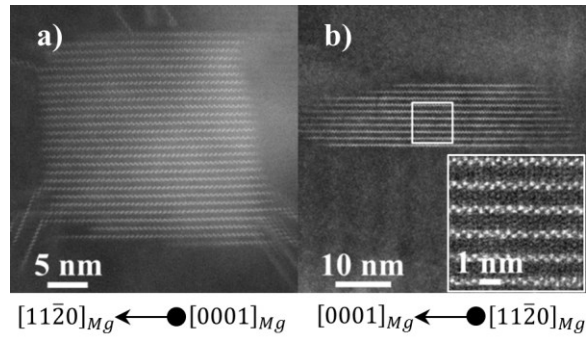
Figure 38: HAADF-STEM images of the Mg-2.16 at. % Y alloy aged for 400 hours at 200 °C with the incident beam parallel to the a) [0001]$_{Mg}$ and b) <11$\bar{2}$0>$_{Mg}$ zone axes. The inset in b) is a high magnification image of the region within the white box.

After deformation of the aged Mg-Y alloy, STEM images reveal that precipitates are sheared along two different sets of planes. The resulting projections along the $\langle 0001 \rangle_{Mg}$ and $\langle 11\bar{2}0 \rangle_{Mg}$ zone axes of the precipitates in **Figure 39a** and **b** are evidence that they were sheared by at least one <a> dislocation on the basal plane, giving rise to stacking faults that are orthogonal to the $[0001]_{Mg}$ direction and extended across the length of a β' precipitate. In the view shown in **Figure 39c**, the β' precipitates were sheared along multiple $\langle 11\bar{2}0 \rangle_{Mg}$ lines, which were interpreted as evidence of <a> dislocation prismatic or <c+a> dislocation pyramidal slip that would account for the translation of the Y rows along the $[11\bar{2}0]_{Mg}$ direction.
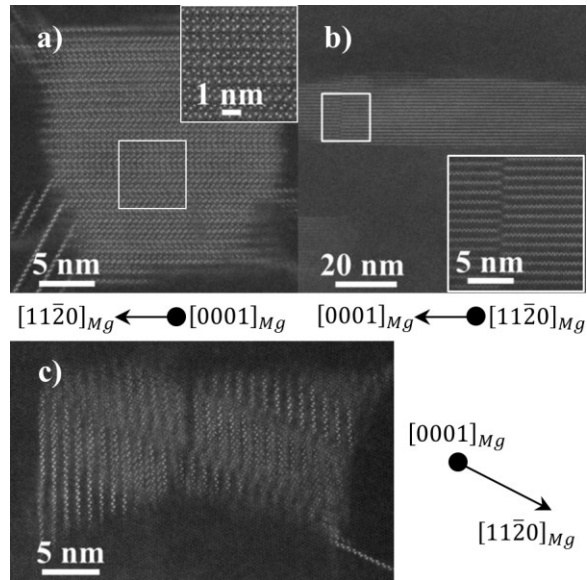
Figure 39: HAADF-STEM images of the Mg-2.16 at. % Y alloy aged for 400 hours at 200 ºC and deformed with the incident beam parallel to the a) and c) [0001]$_{Mg}$ and b) <11$\bar{2}$0>$_{Mg}$ zone axes. The insets in a) and b) are high magnification images of the regions within the white boxes.

Both the β''' precipitates in Mg-Nd and the β' precipitates in Mg-Y are sheared by basal slip, which is the common deformation mode observed in Mg [52, 53]. Non-basal shearing of β' precipitates with an <a> component is consistent with previous observations of pyramidal <c+a> dislocations slip in comparable Mg-Y alloys [52, 83]. Although the ease at which β''' and β' are sheared could not be quantified, their inherent atomic structures provide insight into their relative shear resistance. The β''' phase easily accommodates stacking defects (**Figure 36a**), and is to be contrasted with the β' phase for which no defects were observed prior to deformation. We hypothesize that the high density of defects observed in the undeformed β''' phase reflects a relatively lower staking fault energy and therefore lower shearing resistance compared to the β' phase. During aging at 200 ºC, the hardness gain during aging of Mg-Nd is indeed modest (73±3 HV in **Figure 9**) despite a β''' phase volume fraction estimate of 1.6 volume %. The hardness increase is more significant in Mg-Y alloys (**Figure 27**), which reflects both a higher precipitate volume fraction and the presumed higher shear resistance. Finally, the β''' precipitates observed

73

here would not grow significantly upon continued aging based on the results in Chapter 3. The size of β' precipitates would also not significantly change with further aging, as suggested from the results in Chapter 4. Therefore, a switch to an Orowan mechanism in either alloy is highly unlikely.

5.4 Conclusions

HAADF-STEM imaging before and after deformation of aged alloys revealed that the β''' precipitates in Mg-Nd alloys and β' precipitates in Mg-Y alloys are sheared by dislocations during deformation. The β''' phase was sheared along the basal plane while the β' phase was sheared by both basal <a> slip and non-basal <a> or <c+a> slip.

CHAPTER 6:

Evolution of the precipitate structures and composition in Mg-Y-Nd and WE43 alloys

6.1 Introduction

Precipitation in commercial WE (WE43 and WE54) alloys has been covered extensively in the literature [2-12]. At peak aging (16 hours at 250 $^{\circ}$C), the primary precipitates present are the globular β', platelet β''' (referred to as platelet β' in previous literature [7]), β_1, and β phases [13]. The strength of the alloy at this stage has been attributed to β_1 [73], although the microstructure contains a fair amount of β''' and β' phases that also have been shown to increase hardness in Mg-Nd and Mg-Y alloys (see Chapters 3 and 4). The β''' and β' phases in WE alloys form invariably as clusters where at least two β''' precipitates are attached to either side of the β' [7]. The β''' has a platelet morphology and primitive orthorhombic crystal structure made up of rows of hexagonal rings and zigzag chains [13], similar to the β''' phase in Mg-Nd alloys (see Chapter 3). The β' phase is similar to that of the β' in Mg-Y alloys where the precipitates have equiaxed shapes in the basal plane and a base-centered orthorhombic crystal structure [45]. Precipitates with similar structures and arrangements have been reported for Mg-Gd alloys that contain long chains of alternating β''' and β' precipitates [15, 84]. Precipitate networks are also observed in Mg-Y alloys, as discussed in Chapter 4, and seem to be associated with the presence of β'.

The composition of the β' phase varies in the literature while the composition of β''' has yet to be analyzed. The β' composition has been suggested to be either $Mg_{12}YNd$ [3, 4] or $Mg_{24}Y_2Nd_3$ [57], neither of which match with the atomic structure of the β' phase (32 atoms/unit cell). Another study using APT also reported a higher Y content than Nd, however their results showed the β' precipitates to contain more Zr than Nd or Y [60]. Yet, it was mentioned in Chapter 3 that Zr did not play a role in the precipitation process.

Understanding the structure of the different phases, the role of Y and Nd in controlling which phases form, and their effect on alloy strength would bring clarity to the properties of WE alloys. This work uses HAADF-STEM to characterize the evolution of the precipitate microstructure with aging and a combination of APT and EDS to quantify the composition of β''' and β' phases in a model Mg-Y-Nd alloy and commercial WE43 alloy.

6.2 Experimental

The alloys examined in this work were provided by Magnesium Elektron North America Inc. The compositions of the two alloys were measured by inductively coupled plasma mass spectrometry and found to be Mg-1.06Y-0.29Nd (at. %) and Mg-1.22Y-0.39Nd-0.13Zr-0.01-Zn-0.08RE (at. %). The alloys were encapsulated in quartz tubes in an argon atmosphere and solution treated at 560 ^{o}C for 24 hours (for Mg-Y-Nd) or 525 ^{o}C for 8 hours (for WE43) followed by water quenching. Samples were then aged in an oil bath at either 200 ^{o}C for times ranging between 7 minutes and 1000 hours or at 250 ^{o}C for times ranging between 3 minutes and 110 hours (WE43 only) followed by water quenching. TEM specimens were prepared using the method described in Ref. [13]. Micrographs were taken using a JEOL 2100F operated at 200 kV with a collection angle of 52 mrad and a double-corrected JEOL 3100R05 microscope operated

at 300 kV with a collection angle of 74 mrad. EDS data and STEM images were obtained using a FEI Titan microscope operated at 80 kV with a beam current of 240 pA or 290 pA, inner collection angle of 50 mrad, and convergence semi-angle of 10 mrad at the National Center for Electron Microscopy, Molecular Foundry, Lawrence Berkeley National Laboratory. The EDS detector is an FEI Super-X Quad windowless detector based on silicon drift technology. Analysis of the EDS data was performed using the Bruker Esprit Software which has been calibrated against mineral standards for quantitative accuracy.   The APT specimens were electropolished with a solution of 25% perchloric acid in acetic acid using 14-20 V and then fine polished with a solution of 2% perchloric acid in butoxyethanol with 5-10 V. The APT data was collected on a Cameca LEAP XHR4000 instrument operated in voltage mode at 200 kHz with voltage pulse amplitude equal to 20% of the applied DC voltage. Specimens were maintained at a temperature of either 25 K (for WE43) or 50 K (for Mg-Y-Nd) and the voltage was automatically increased to maintain a constant evaporation rate varied between 0.002 and 0.01 atoms per pulse on average.   Data reconstructions and analyses were carried out using the Integrated Visualization and Analysis Software (IVAS 3.6.12) package.   The reconstruction parameters, geometric factor, and image compression factor were chosen to ensure that the planar spacings observed at identified poles and the angles between such planes match that of the hexagonal magnesium matrix. The evaporation field was selected to be that of Mg at 21 V/nm [67]. Crystallographic analysis methods developed for APT [68] were used to determine the orientation of the APT data.   Representative mass spectra showing the different chemical species detected during field evaporation of the Mg-Y-Nd and WE43 alloys investigated in this chapter are further discussed in **Appendix II**.

The alloys examined in this chapter are affected by evaporation artifacts including local magnification effects [85] at the precipitates and chromatic aberrations caused by crystallographic poles [86]. Local magnification effects are caused by differences in evaporation field between two phases. In the case of RE-rich precipitates in Mg-Y-Nd and WE43 alloys, the precipitate phases have higher evaporation fields than the matrix phase [85, 87]. Therefore the matrix atoms evaporate more easily than the atoms in the precipitate, causing the precipitate to gradually protrude from the surface of the tip. The protruding precipitate has a smaller local radius at the tip leading to a magnified footprint on the detector. As a result, the reconstructed density of atoms inside the precipitates appears lower than the surrounding matrix. To illustrate local magnification effects on the reconstruction, **Figure 40** is a profile of the total number of atoms (Mg, Nd, and Y) taken across the precipitate circled in **Figure 41a**. The density decreases inside the precipitate, indicating that the precipitates have a higher evaporation field than the matrix.
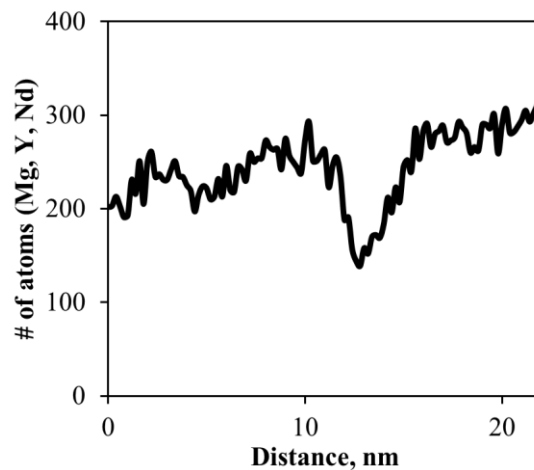
Figure 40: Density profile taken across the platelet precipitate and in the same direction as the arrow indicated in Figure 41a. The density is equal to the total number of Mg, Nd, and Y atoms.

Chromatic aberration introduced by crystallographic poles is also observed in Mg-Y-Nd/WE43 alloys. The RE (Y and Nd) atoms are shifted away from the low index poles (**Figure 41**). A previous report showed a similar effect in Al-Ag alloys where the solute elements shifted towards low index poles [86]. Two-dimensional density contour plots showing the density of Mg and Nd were taken perpendicular to the $[10\bar{1}0]_{Mg}$ direction in the region of the platelet circled in **Figure 41a**. The Nd and Mg plots are overlapped on top of each other and made partially transparent in order to visualize the displacement between the density of Nd and Mg shown in the white box in **Figure 41b**. If there were no trajectory artifacts, the low density region of the platelet from the Mg contour plot would overlap perfectly on top of the high density region from the Nd. A profile of the number of Mg, Nd, and Y atoms across the platelet circled in **Figure 41a** and along the direction indicated by the black arrow is shown in **Figure 41c**. A dotted black line is drawn vertically through the profiles at a distance of 10 nm in each profile. The Y and Nd curves are shifted towards the left of the line while the Mg curve is shifted towards the right. Also, the Y (red) profile is consistently wider than the Nd (green) profile. Both the shift of RE atoms and the broad Y peak are related to variations in the evaporation field between the atoms in the matrix and precipitate [86-88]. Another example illustrating the effect of differences in evaporation field on the ion trajectories can be visualized from the distribution of Mg^{1+}, Mg^{2+}, Mg^{1+} hydrides, and Mg^{2+} hydrides in **Figure 56** in **Appendix II**. The Mg^{1+} and Mg^{1+} hydrides are correlated with the precipitates, indicating the precipitates have a higher evaporation field than the matrix which causes the low field species (Mg^{1+} and Mg^{1+} hydrides) to evaporate with the high field precipitates.
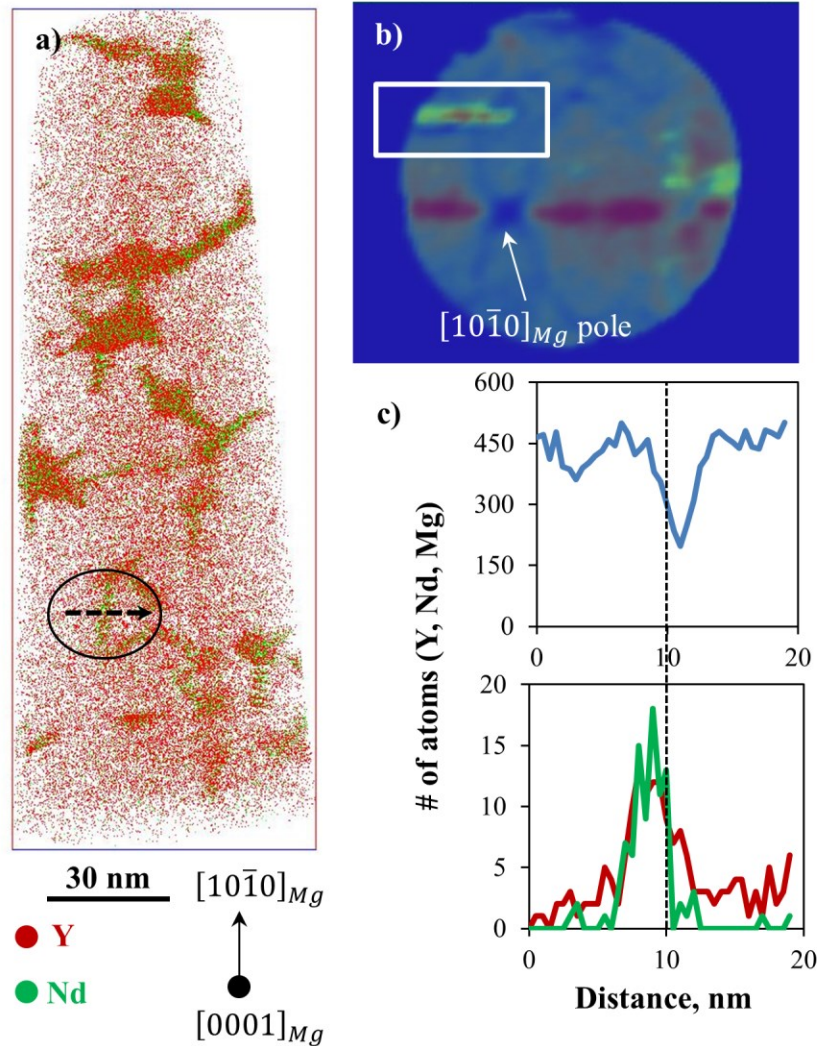
Figure 41: a) APT reconstruction showing only the Nd and Y atoms from the Mg-1.06Y-0.29Nd (at. %) alloy. b) 2D density contour plots for Nd and Mg overlapped on top of each other and c) density profiles for Mg (blue), Nd (green), and Y (red) across the platelet shown in a). The arrow in a) indicates the direction of the density profile in c).

Evaporation artifacts can be problematic when trying to quantify the size and composition of the precipitates because the interface between the precipitate and matrix is blurred. This is especially an issue for small precipitates where the entire precipitate could be affected by trajectory overlaps between matrix and precipitate. Therefore, quantification of the Nd:Y ratio for the β''' platelets was determined from profiles of the number of atoms (Y and Nd) versus the distance across the precipitate. The peaks of these curves were integrated to obtain the total number of RE atoms in the platelet β''' precipitates. The profiles across the plates were

measured parallel to the $\langle 11\bar{2}0 \rangle_{Mg}$-type directions (thickness dimension). It was assumed that the atoms measured under the peaks accounted for all of the atoms in the precipitates. Due to the size and shape of the globular β' particles, evaporation artifacts did not have as significant of an effect on the β' composition as compared to the platelets, allowing the composition in terms of Nd and Y content in atomic percent to be determined. The concentration profiles across the globular β' had clear plateau regions where the concentration of RE elements was measured by taking the average of the composition in these regions. The profiles across the globular β' particles were oriented so that the profile was cutting through as close to the middle of the particle as possible without touching any of the attached β''' platelets.

6.3 Results

6.3.1 Aging behavior of Mg-Y-Nd and WE43

The aging response of the Mg-1.06Y-0.29Nd (at. %) and WE43 alloys during isothermal aging at 200 ^{o}C (Mg-Y-Nd and WE43) and 250 ^{o}C (only WE43) are shown in **Figure 42**. When aged at 200 ^{o}C, both alloys experience similar aging behavior as their curves have the same shape and approximate magnitude. The hardness increases slowly until about 10 hours of aging and then sharply increases until about 400 hours where the alloys reach their peak hardness. Further aging results in the gradual decrease in hardness as the alloys are overaged. During aging at 250 ^{o}C, the hardness of WE43 increases initially up to 7 minutes where it reaches its first peak hardness. The hardness gradually decreases until 1 hour when the alloys undergo a second increase in hardness. The second peak in hardness is reached after 16 hours. The evolution of the precipitate microstructure and the chemistry of the precipitates and matrix when aged at 200 ^{o}C (for Mg-Y-Nd) and 250 ^{o}C (for WE43) were analyzed using APT and HAADF-STEM.

81
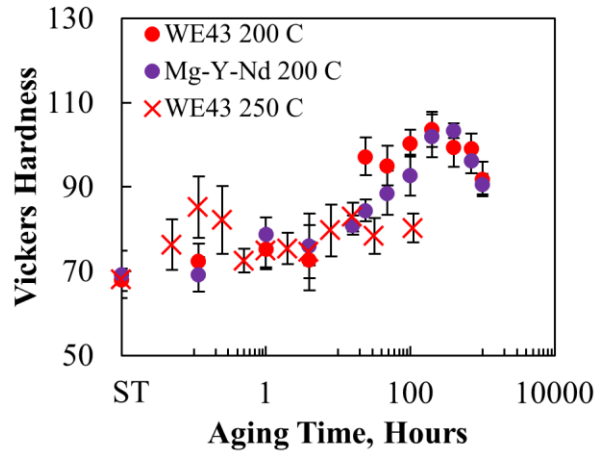
Figure 42: Hardness curves for the Mg-1.06Y-0.29Nd (at. %) alloy aged at 200 °C (reprinted from Ref. [70]) and the WE43 alloy aged at 200 °C and 250 °C. ST represents the solution treated condition.

The microstructure of the Mg-Y-Nd alloy after being aged for various times at 200 °C are shown in **Figure 43**. After 16 hours, the hardness increased due to the presence of GP zones, β', and β''' (**Figure 43a**). The precipitates are relatively isolated at this stage. By 100 hours of aging, the GP zones have completely dissolved and the microstructure is dominated by a high number density of β'-β''' clusters (**Figure 43b**), resulting in the significant increase in hardness. The microstructure after aging for 1000 hours contains long chains of β' and β''' precipitates connected in alternating order. Occasionally a $β_1$ platelet is observed connecting two β' precipitates in the chain, as illustrated in **Figure 43c**. The number density of precipitates at this stage has decreased as the precipitates in the chains have coarsened, resulting in the decrease in hardness.

The orientation of the β'-β''' clusters in the microstructure after aging for 100 hours at 200 °C varies within the analyzed grain. Near the grain bound the majority of the precipitates appear to be aligned along the same $\langle 1\bar{1}00 \rangle_{Mg}$-type direction (**Figure 44**) while there is a more even mix of all three orientation variants towards the middle of the grain (**Figure 43b**). This type of

82

preferential alignment has been reported to occur in Mg-Gd-Zr alloys during creep testing and in Mg-Nd alloys aged under stress that is discussed in **Appendix I**; however, no external stress was applied in the case of the Mg-Y-Nd alloy. It is possible that thermal stresses were introduced during processing and caused the precipitates to be preferentially aligned.
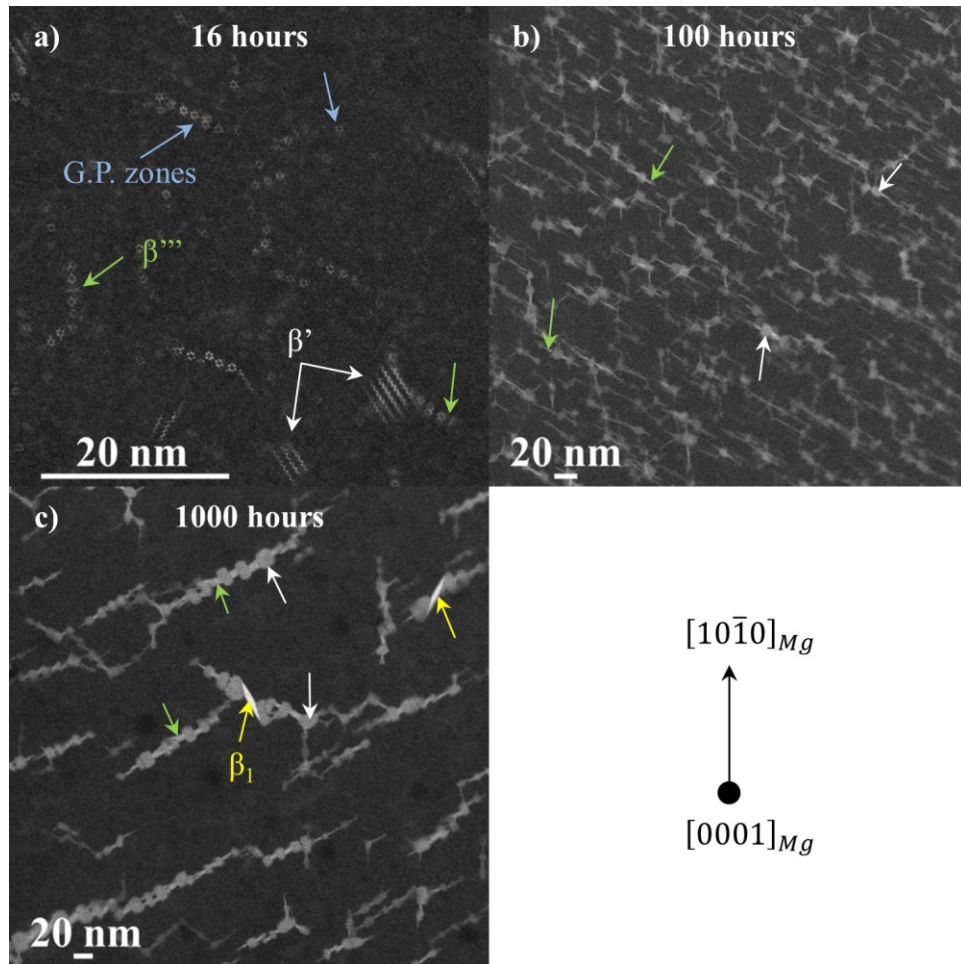
Figure 43: HAADF-STEM images of the Mg-1.06Y-0.29Nd (at. %) alloy after being aged for a) 16, b) 100, and c) 1000 hours at 200 ^{o}C. The incident beam is parallel to the [0001]$_{Mg}$ zone axis.
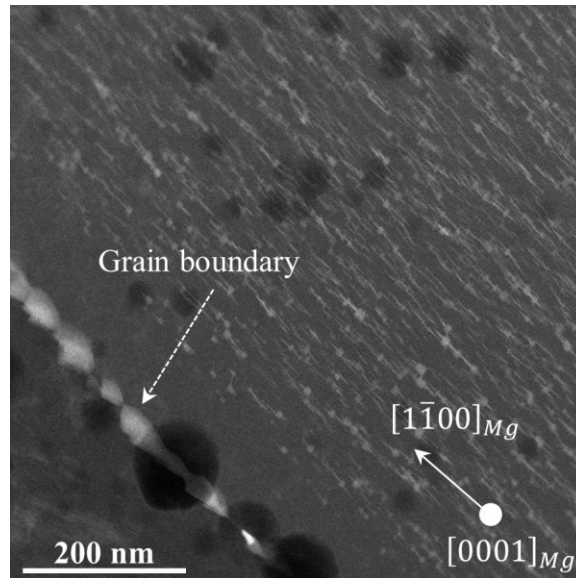
Figure 44: HAADF-STEM image of the Mg-1.06Y-0.29Nd (at. %) alloy aged for 100 hours at 200 $^{\circ}$C taken with the incident parallel to the [0001]$_{Mg}$ zone axis. The dark circles are very thin regions or holes in the TEM sample created during electropolishing

Images showing the microstructure of WE43 aged at 250 $^{\circ}$C are presented in **Figure 45**. When aged for 15 minutes, the hardness initially increased due to the formation of small solute clusters, GP zones, and β''' (**Figure 45a**). At 2 hours, the microstructure contains a sparse distribution of β' and β''' clusters, as shown in **Figure 45b**. By 16 hours the microstructure contains several phases, which are the β', β''', β_1, and β phases, as indicated with arrows in **Figure 45c**. Since the β phase forms by an in situ transformation of the β_1 phase [5], some of the dark platelets in **Figure 45c** are β.
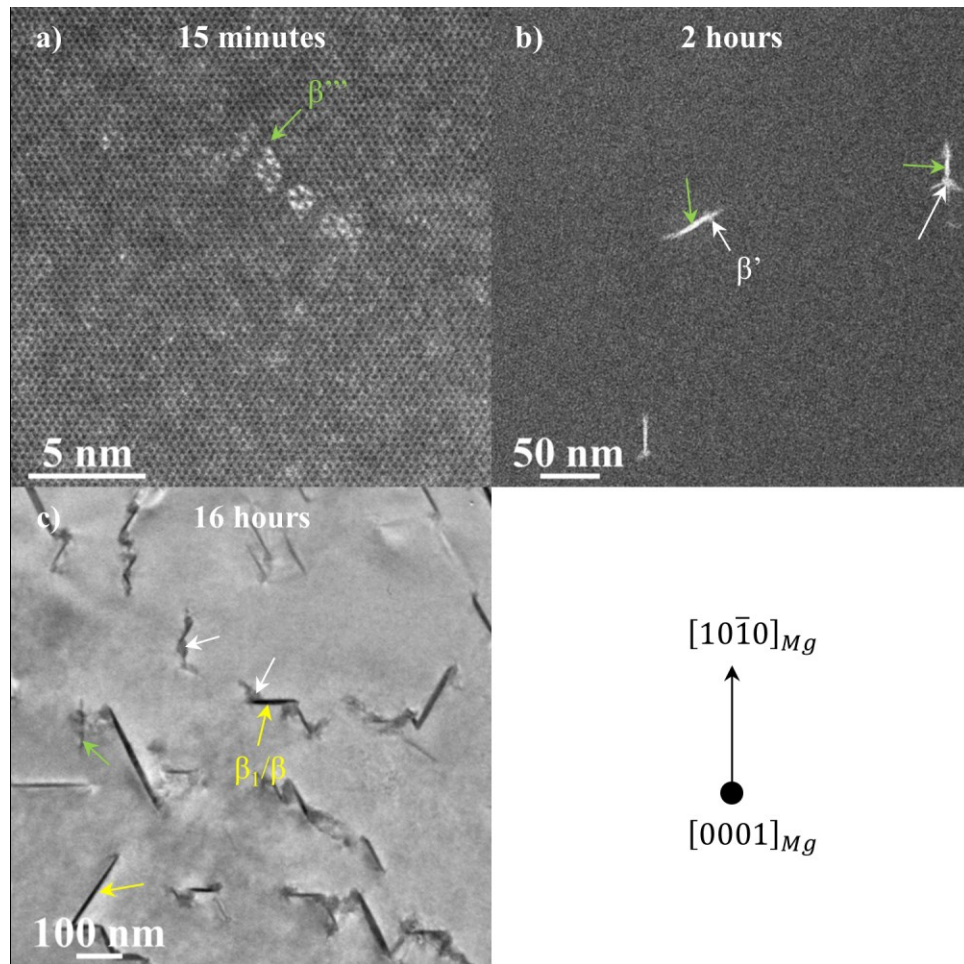
Figure 45: a) & b) HAADF-STEM and c) BF images of the WE43 alloy aged for a) 15 minutes, b) 2 hours, and c) 16 hours at 250 °C. The incident beam is parallel to the $[0001]_{Mg}$ zone axis.

The precipitates in the aged Mg-Y-Nd and WE43 alloys have similar structures to those that form in the binary Mg-Y and Mg-Nd alloys. The GP zones consist of RE-rich columns arranged on the Mg lattice sites in either a hexagonal ring pattern or single zigzag monolayers lying parallel to $\{10\bar{1}0\}_{Mg}$ planes. The V- and S-shaped GP chains that were reported in Mg-Nd alloys [22, 24] are not observed in the Mg-Y-Nd/WE43 alloys (**Figure 43** and **Figure 45**). The β' and β''' phases observed in the Mg-Y-Nd/WE43 alloys (**Figure 46**) are also similar to those in the binary alloys. The β''' phase forms as plates elongated along $\langle 1\bar{1}00\rangle_{Mg}$-type directions. These plates have a primitive orthorhombic crystal structure that consists of RE-rich columns

arranged into either rows of hexagonal rings or zigzag chains separated by four Mg lattice spacings along a $\langle 1\bar{1}00 \rangle_{Mg}$-type direction in the basal plane. Each platelet seems to vary in the amount and arrangement of rows of hexagonal rings and zigzag chains, similar to that observed for the β''' phase in Mg-Nd alloys [22, 26]. Therefore, the RE concentration is expected to vary locally within single precipitates and from precipitate to precipitate. The β' phase forms as equiaxed-shaped precipitates and has a base-centered orthorhombic crystal structure consisting of RE-rich columns arranged into zigzag chains, as described previously for the β' phase in Mg-Y alloys [45]. Finally, the $β_1$ phase in Mg-Y-Nd alloys forms as plates with habit planes lying parallel to the $\{1\bar{1}00\}_{Mg}$-type planes.
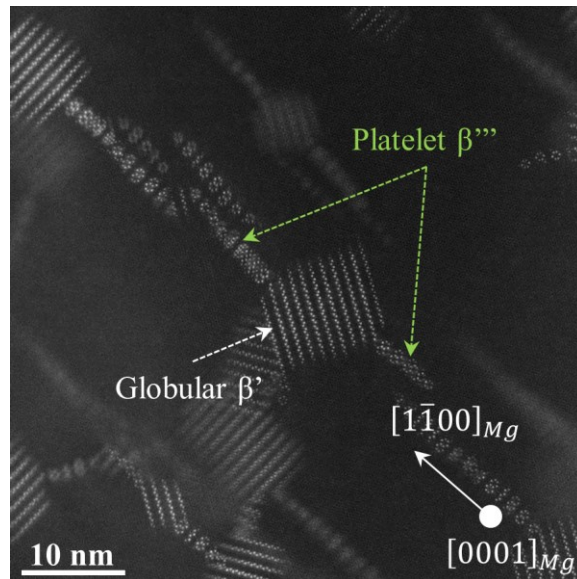
Figure 46: HAADF-STEM image of the Mg-1.06Y-0.29Nd (at. %) alloy aged at 200 ^{o}C for 100 hours taken with the incident beam is parallel to the $[0001]_{Mg}$ zone axis.

6.3.2 APT and EDS analysis of β''' and β' compositions

APT analysis was conducted on Mg-Y-Nd samples aged for 100 hours at 200 ^{o}C so that the microstructure contained primarily β''' and β' precipitates. The APT reconstruction in **Figure**

47 shows that both the β''' platelets and globular β' particles contain Nd and Y. The Nd:Y ratio for the β''' platelets and globular β' particles as well as the measured composition of the globular β' particles are presented in **Table 2**. According to APT the platelet β''' and globular β' phases have about twice as much Y as Nd on average. The matrix contains significantly more Y than Nd (**Table 2**) and likely causes the Y concentration in the β''' precipitates to appear higher than the actual value. The total concentration of RE elements in the globular β' is measured to be 11.7±0.76 at. % (Y+Nd), which is consistent with an atomic structure containing only zigzag chains.
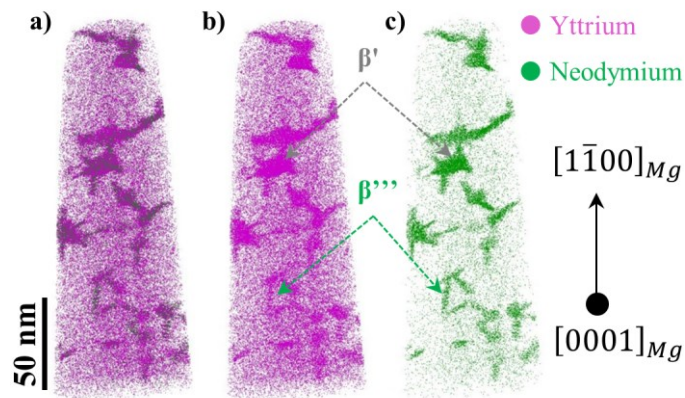
Figure 47: APT reconstruction showing the distribution of a) Y and Nd, b) only Y, and c) only Nd atoms in the Mg-1.06Y-0.29Nd (at. %) alloy aged for 100 hours at 200 °C when viewed along the [0001]$_{Mg}$ zone axis. The entire data set with 100% of the Y (purple) and Nd (green) atoms are being shown.

The relative amounts of Nd and Y in the β''' and β' precipitates were also measured using EDS on a Mg-Y-Nd alloy aged for 1000 hours at 200 °C and are presented in **Table 2**. The EDS spectra from all of the analyzed β''' plates and globular β' precipitates including the background correction are shown in **Figure 57** (**Appendix I**) and an EDS map of a representative precipitate chain of β''' and β' is shown in **Figure 48**. The YK and NdL peaks have high signal-to-noise ratios and were chosen for quantification (**Figure 57** in **Appendix I**). The precipitate compositions are quantified using the ratio of Nd to Y. The β' phase has an average of about

87

three times more Y than Nd whereas the plates on average have about equal amounts of Y and Nd. Considering the large sample thickness compared to the size of the precipitates, it is very likely that some matrix signal was included in the EDS spectra. Similarly to the APT results, the amount of Y in the precipitates may be overestimated. The plates have a wider distribution of measured Nd:Y ratio compared to the globular particles (**Figure 49**), suggesting that the globular β' precipitates are closer to a stoichiometric phase than the β''' platelets and is consistent with the atomic structures of the two phases.

Table 2: Composition (globular β') and Nd:Y ratios for precipitates in the Mg-1.06Y-0.29Nd (at. %) alloy aged at 200 °C for 100 hours (measured by APT) and 1000 hours (measured by EDS).

	APT				
	#	Nd:Y	Y at. %	Nd at. %	(Y+Nd) at. %
Globular β'	35	0.50±0.06	7.85±0.55	3.85±0.40	11.7±0.76
Platelet β'''	32	0.60±0.07	-	-	-
Matrix	9	0.08±0.02	0.56±0.03	0.04±0.01	0.60±0.03
	EDS				
	#	Nd:Y			
Globular β'	94	0.30±0.02			
Platelet β'''	70	0.90±0.07			
Matrix	23	0.06±0.01			

The number of precipitates analyzed is represented by #. The Nd:Y ratios and Nd and Y concentrations are averaged over the number of precipitates analyzed. Errors are equal to three times the standard error of the mean.
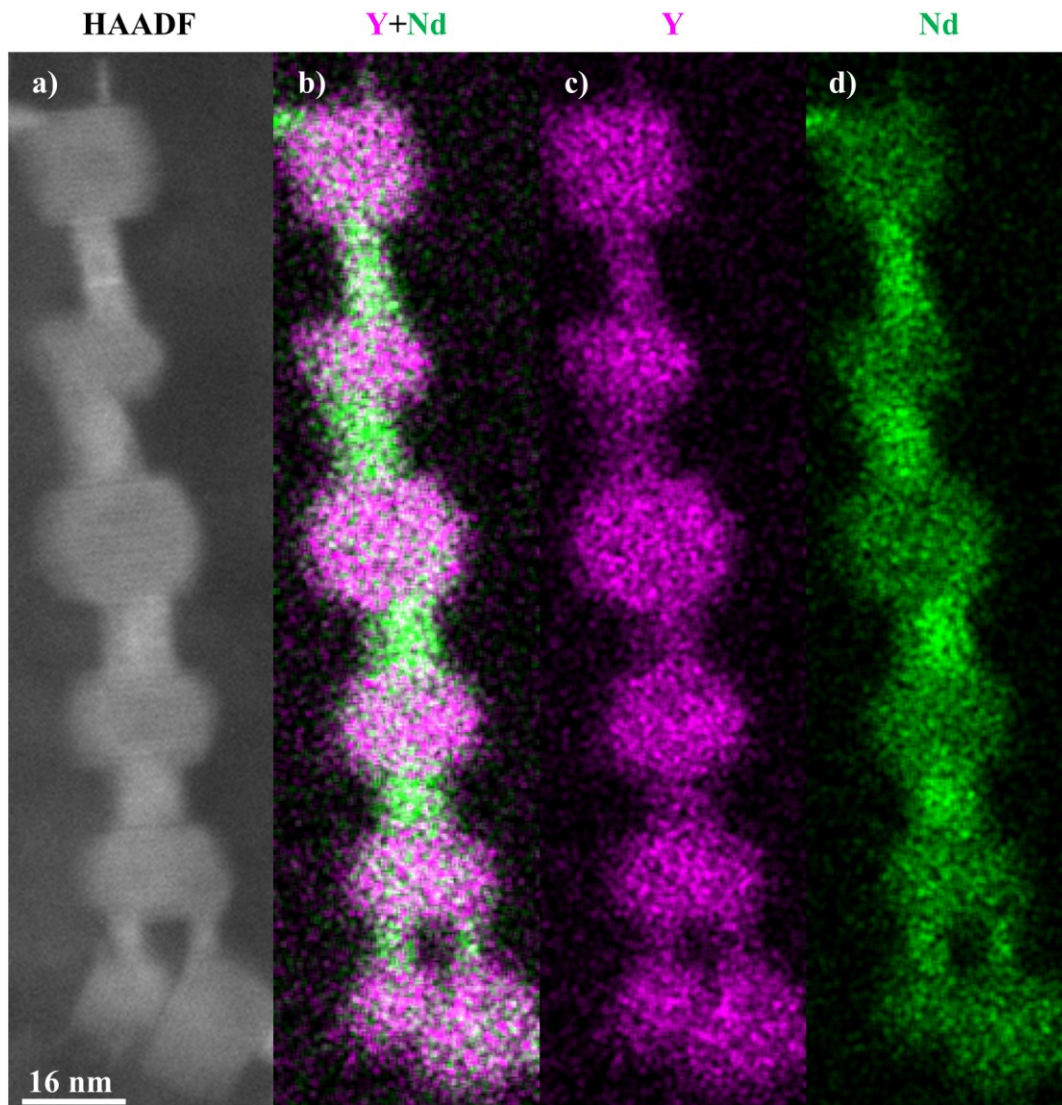
Figure 48: a) HAADF-STEM micrograph and b-d) EDS maps showing the spatial distribution of b) Y and Nd, c) only Y, and d) only Nd in the Mg-1.06Y-0.29Nd (at. %) alloy
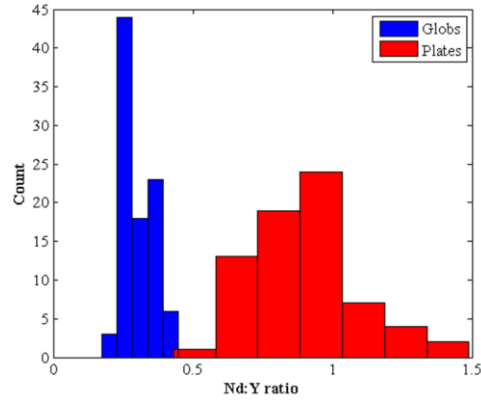
Figure 49: Distributions of the Nd:Y ratio for the globular β' (blue) and platelet β''' (red) precipitates

6.3.3 Evolution of matrix and precipitate composition in WE43

The chemistry of the β''' and β' precipitates and matrix in WE43 were analyzed after aging for 30 minutes, 2 hours, 4 hours, and 16 hours at 250 $^{\circ}$C and are presented in **Table 3**. These phases have the same shapes, atomic structures, precipitate arrangements (β'-β''' clusters), and orientations as those in the Mg-Y-Nd alloy. The composition of the matrix and globular β' phases are reported in atomic percent while the composition of the β''' platelets are shown as only the Nd to Y ratio. When aged, the matrix composition decreases (1.89±0.17 at. % RE at 30 minutes to 1.27±0.12 at. % RE at 16 hours), which is consistent with an increasing volume fraction of precipitates with aging. Both types of precipitates are shown to have approximately equal amounts of Nd and Y. Like the Mg-Y-Nd alloy, the total amount of RE (Y+Nd at. %) in the globular β' is 12.0±1.2 at. % on average, which is in agreement with the structure containing only zigzag chains. The Nd:Y ratio for the platelet β''' is higher than that reported for the β''' in Mg-Y-Nd and is attributed to the fact that the precipitates in WE43 are larger than those in Mg-Y-Nd, suggesting that evaporation artifacts have less of an effect on the larger precipitates.

90

Table 3: Composition (globular β') and Nd:Y ratios for the precipitates and matrix in WE43 after aging for various times at 250 °C measured by APT

	#	Nd:Y	Y at. %	Nd at. %	(Y+Nd) at. %
30 minutes					
Matrix	3	0.28±0.03	1.48±0.14	0.41±0.04	1.89±0.17
2 hours					
Globular β'	4	1.00±0.27	5.29±1.49	5.37±2.55	10.7±3.97
Platelet β'''	5	0.97±0.74	-	-	-
Matrix	4	0.30±0.07	1.27±0.18	0.38±0.13	1.65±0.30
4 hours					
Globular β'	4	0.92±0.22	6.83±1.15	6.22±0.90	13.0±1.39
Platelet β'''	4	1.29±0.15	-	-	-
Matrix	2	0.23±0.11	1.12±0.24	0.26±0.18	1.39±0.43
16 hours					
Globular β'	8	0.69±0.12	7.22±0.55	4.91±0.59	12.1±0.60
Platelet β'''	10	1.10±0.17	-	-	-
Matrix	4	0.10±0.01	1.16±0.11	0.11±0.01	1.27±0.12

The number of precipitates analyzed is represented by #. The Nd:Y ratios and Nd and Y concentrations are averaged over the number of precipitates/matrix regions analyzed. Errors are equal to three times the standard error of the mean.

6.4 Discussion

Although the β''' and β' precipitates in the Mg-Y-Nd and WE43 alloys have different compositions and spatial arrangements, their unique behavior can be explained using observations of the binary Mg-Nd and Mg-Y alloys in Chapters 3 and 4. The β''' phase forms as plates elongated along $\langle 1\bar{1}00 \rangle_{Mg}$ -type directions and has a primitive orthorhombic crystal structure containing varying amounts of rows of hexagonal rings and zigzag chains, similar to the β''' plates in Mg-Nd [22]. The β' phase has a base-centered orthorhombic crystal structure with an equiaxed shape in the basal plane that is synonymous to the β' phase in Mg-Y alloys [45]. The coexistence of the two phases (β''' and the β') suggest that the ternary alloy is in a three-phase equilibrium region.

The similarity between the structure and morphologies of the β''' and β' phases in the ternary and binary alloys suggests that elastic strain energy continues to dominate in the ternary system. Moreover, the alternating sequence of long chains of platelet β''' and globular β' precipitates is also consistent with elastic strain energy minimization. Similar observations were made in Mg-Gd alloys [15]. This strain-induced patterning of precipitates was also observed in Mg-Y alloys, as described in Chapter 4, where the β' precipitates and/or thin strands connect into cell structures as a result of the highly strained matrix at the corners of the square-shaped precipitates.

In Mg-Y alloys, thin strand-like features were observed attached to the corners and $\{1\bar{1}00\}_{Mg}$ planar edges of the β' phase (see **Section 4.3.1**). Instead, in the Mg-Y-Nd alloy, β''' platelets are attached to the β' phase either at the corners or at any of the four edges, as illustrated in **Figure 46**. The presence of connected β''' and β' precipitates early on in the aging process could be an indication that β''' precipitates nucleate heterogeneously on the β' particles. Clusters of β''' and β' were also observed in WE43 when aged at 250 °C; however instead of forming the long chain structures the microstructure contains a relatively fine distribution of β_1 platelets (**Figure 45c**). The more rapid formation of β_1 at this higher temperature depletes much of the solute from the matrix and prevents the chain structure from forming.

The β''' and β' phases in the Mg-Y-Nd alloy contain different amounts of Nd and Y, however there are some discrepancies between the measurements from the two analysis techniques due to the artifacts and limitations of the analysis techniques. The Nd:Y ratio for the globular β' phase is on average 0.50±0.06 using APT or 0.30±0.02 using EDS **Table 2**. As mentioned earlier, the EDS measurements are affected by the surrounding matrix, which can cause the Y content to appear artificially high in the precipitate. Although the precipitates in APT also experience

artifacts such as preferential evaporation of the matrix atoms, the β' phase is less affected by the evaporation effects. The total concentration of Y and Nd (11.7±0.76 at. %) in the globular β' is in agreement with the atomic structure containing only zigzag chains and does not vary significantly between precipitates (**Figure 49**), therefore, the composition can be written as $Mg_{14}Y_{1.33}Nd_{0.67}$, which has a higher Y to Nd ratio than reported in the literature ($Mg_{12}YNd$ [3, 4] and $Mg_{24}Y_2Nd_3$ [57]). The composition of the β''' and β' phases in WE43 are similar to those in Mg-Y-Nd and were only measured using APT. The average total RE concentration of all the measured globular β' precipitates is 12.0±1.2 at. % (Y+Nd), suggesting that it also has a stoichiometry of $Mg_{14}Y_{1.33}Nd_{0.67}$. Since the composition of the precipitates does not appear to change with aging, the decreasing Y and Nd concentrations in the matrix is consistent with an increase in the volume fraction of precipitates.

The aging kinetics of the Mg-Y-Nd alloy is intermediate to the binary alloys such that it reaches peak hardness at an aging time later than Mg-Nd (**Figure 9**) and earlier than Mg-Y (**Figure 27**). Pinpointing to a specific reason is beyond the scope of this work as it is likely a complex synergy between thermodynamics and kinetics. Recent DFT calculations [89, 90] suggested that the diffusion of Y and Nd in Mg should be equivalent, indicating that thermodynamics is controlling not only phases, but also their nucleation mechanisms and kinetics. One would need to consider the details of the thermodynamic driving force for precipitation of each of the phases involved in all three alloys, the energy barrier for nucleation in the case of homogeneous or heterogeneous nucleation, the existing nucleation sites, and the amount of solute (different in each alloy).

6.5 Conclusions

The evolution of the precipitate microstructures in Mg-Y-Nd/WE43 alloys were examined using HAADF-STEM; and the compositions of the matrix and β''' and β' precipitates in Mg-Y-Nd/WE43 alloys were measured using EDS and APT. Both alloys formed the same precipitate phases with aging: GP zones, β''', β', and β_1. Each of these phases have identical crystal structures to those reported in the binary Mg-Nd and Mg-Y alloys, however the V- and S- shaped units reported in Mg-Nd alloys were not observed in the Mg-Y-Nd/WE43 alloys. DFT can be used to calculate the stability of the V- and S- units in Mg-Y-Nd and show why they do not form in alloys containing both Nd and Y. The main conclusions of this work are presented below.

- The arrangement of β''' and β' clusters and long chains are driven by minimizing elastic strain energy

- The globular β' has more Y than Nd while the β''' plates have more Nd on average

- The β' composition is consistent with a stoichiometric configuration and the β''' phase has a varying composition as a result of the amount of rows of hexagonal rings and zigzag chains. The differences in composition between β''' and β' in Mg-Y-Nd/WE43 suggest that the alloys have a three phase equilibrium region consisting of matrix, β''' and β' phases in the metastable phase diagram.

- The β' and β''' precipitate compositions in WE43 do not change with aging, while the decrease in matrix composition indicates an increase in precipitate volume fraction with aging.

CHAPTER 7:

Perspectives

A significant amount of work on precipitation in Mg-RE alloys focused on complex alloys containing several alloying elements, which makes it difficult to understand the individual effects of each alloying element on precipitation. In addition, much of the work on simpler binary and ternary alloys had only presented snapshots of the microstructure at single aging conditions and do not examine the evolution of the precipitate phases, despite the need for kinetic information on precipitation. In this thesis, the evolution of the precipitate shape, atomic structure, arrangement, and composition in Mg-RE alloys were examined using HAADF-STEM and APT to identify the role of alloying element on the precipitation behavior in Mg alloys containing Nd and Y. In addition, hardness curves were used as an indirect method for determining the effect of aging on alloy strength.

This study of metastable phases in Mg-Nd, Mg-Y, and Mg-Nd-Y highlighted the common mechanisms by which precipitation occurs in Mg-RE alloys. Elastic strain energy controls precipitate structure with different row and ring structures in Mg-Nd and Mg-Y, morphology with platelets in Mg-Nd and needles in Mg-Y, and spatial arrangement such as the striking cellular structure in Mg-Y. Therefore elastic strains provide a handle on alloy microstructure optimization by selecting alloying elements and phases with appropriate elastic properties. At this stage and taking into account existing literature on Mg-Gd alloys, further experimental work on Mg-RE alloys may not be necessary to determine precipitate phases and shapes. A recent

computational study predicted the β' and β''' structures to form in all of the first-row binary Mg-RE alloys using first-principles calculations [75]. A holistic approach based on these initial first principle calculations, phase field simulations, and machine learning could also offer efficient screening and predictability. See for instance Ref. [91]. A number of non-RE elements, e.g. Ca, Zn, Sn, have also been shown to form nanoscale metastable precipitates [92-96], and further work is warranted to clarify precipitation mechanisms and possible synergy in complex alloys.

Tailoring precipitation serves to design optimum properties. However, the present work only focused on hardness measurements that are not directly interpretable in terms of yield strength and combine flow properties. While hardness has been shown to be approximately three times the yield strength value for aluminum alloys [97], this relationship does not necessarily apply to Mg alloys that have highly anisotropic properties. A more direct comparison between precipitate microstructure and alloy strength and flow behavior would be achieved using tensile testing. With the combination of dislocation dynamic simulations, precipitate/dislocation interactions, and experimental testing, the key parameters describing precipitate microstructures could be clarified and lead to efficient design criteria for tensile behavior, similarly to the approach suggested above for microstructural design. In addition, a number of observations made during the course of this dissertation led to additional scientific questions that could not be addressed due to time, material, or equipment limitations. The following few points describe each of the topics and provide ideas for answering these open questions.

7.1 Effect of stress on precipitate orientation in Mg-Nd alloys

As shown in Chapter 6, β''' precipitates near the grain boundary in a solution treated and aged Mg-1.06Y-0.29Nd at. % alloy showed preferential alignment along one of the $\langle 1\bar{1}00\rangle_{Mg}$-type

directions. I hypothesize that residual stresses may have caused the suppression of one or two of the variants resulting in an apparent alignment of the precipitates. In order to test this hypothesis, the effect of stress on precipitation of β''' was investigated on a Mg-0.40 at. % Nd alloy that had been aged under stress. The details of this study can be found in **Appendix I**. The analysis showed that the formation of a certain β''' variant depends on the orientation of the variant with respect to the stress axis and that it is possible to suppress the formation of certain variants. However, this analysis alone is not enough to determine the magnitude of stress required to affect the formation of certain variants and does not identify the stage at which precipitation is affected by the stress (i.e. nucleation and/or growth). Detailed experimental work would be required to determine the effect of an applied external stress on the nucleation and growth behavior of β''' precipitates in Mg-Nd and to identify the extent to which residual stresses can have such a selective effect. A combination of 3D orientation imaging combined with phase field modeling to determine the distribution of internal stresses could answer these questions. The impact of stress on variant selection is not a simple curiosity as it could significantly affect the mechanical response through inhomogeneity in the distribution and strength of dislocation obstacles.

7.2 Nature and origin of an additional phase in Mg-Y alloys

As mentioned in Chapter 4, the microstructure of the Mg-2.16 at. % Y alloy aged between 200 and 5000 hours of aging at 200 $^\circ$C contained a phase that had not been previously reported for this alloy system. This phase forms as thin plates lying parallel to the basal plane as shown in **Figure 50**. Thin planar features lying parallel to the basal plane have been reported in Mg-Y and Mg-Gd alloys containing Zn [51, 98-101] and have been attributed to the improved mechanical

properties compared to alloys that do not form the basal features [51]. When viewed along the $[0001]_{Mg}$ zone axis, the basal plates in the Mg-2.16 at. % Y alloy appear scattered throughout the microstructure and appear as white patches indicating that they contain a heavier element than Mg (**Figure 50a** and **b**). The plates are only three atomic layers thick (**Figure 50c** and **b**) along the c-axis. EDS maps of the plates along a $\langle 11\bar{2}0 \rangle_{Mg}$ zone axis show that the plates are rich in Y (**Figure 51**). However it is also possible that they might involve impurity elements such as Zn, that were not detected. Further analysis using APT is suggested to determine whether the phase contains impurity elements and to elucidate its structure using HAADF-STEM. If no impurity elements are present, then Mg-Y alloys are unique amongst other Mg-RE alloys because they form both prismatic and basal plane precipitates. Having both prismatic precipitates that arrange into a fine cell structure in addition to basal plane precipitates suggests that Mg-Y alloys form better barriers to moving dislocations.
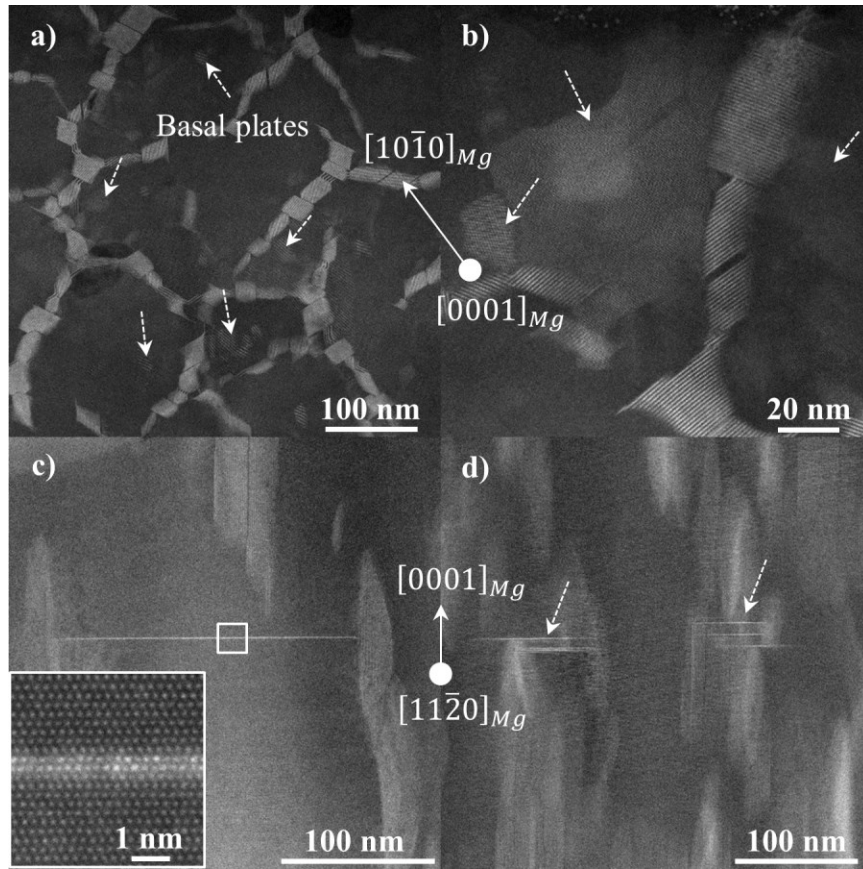
Figure 50: HAADF-STEM images showing the basal plates of the Mg-2.16 at. % Y alloy when viewed along a) and b) $[0001]_{Mg}$ and c) and d) $<11\bar{2}0>_{Mg}$ zones axes. The inset in c) is a high magnification view of the feature enclosed in the white box.
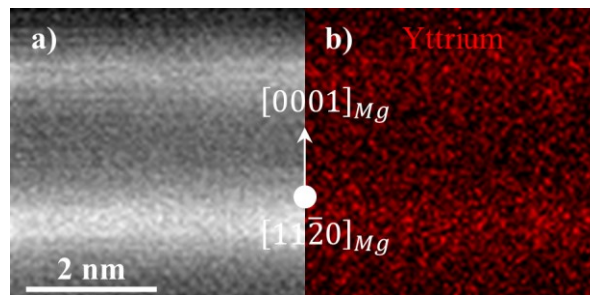
Figure 51: a) HAADF-STEM image showing a region of two basal plates analyzed with EDS. b) EDS map of the region in a). The plates are viewed along a $<11\bar{2}0>_{Mg}$ zones axis.

7.3 Atomic structure of the β' phase in Mg-Y alloys

The structure of the β' phase consists of zigzag chains of Y-rich columns arranged on Mg lattice

positions. It has been assumed up to now that the columns are equidistant from each other.

However, some β' precipitates contain zigzag chains that are slightly distorted such that columns lie at the corners of scalene triangles where the length between each Y-rich column is different (**Figure 52**). In **Figure 52b**, the columns located at the apex of the zigzag chains labeled "A" are shifted slightly to the left whereas the columns in the chains labeled "B" are shifted to the right. For this particular precipitate, the arrangement of zigzag chains with columns shifted right/left is such that two "A" chains are separated by two "B" chains. This shift causes the zigzag chains to be slightly misaligned along $\langle 1\bar{1}00 \rangle_{Mg}$-type directions with respect to the adjacent chains, causing the b-axis to deviate from the $\{11\bar{2}0\}_{Mg}$-type planes. The same shifted structure seen in the zigzag chains of the β' phase is also observed in the strands, as shown in **Figure 52c**. The individual chains of the strands contain triangular arrangements of RE-rich columns where the atoms are shifted along their length ($\langle 1\bar{1}00 \rangle_{Mg}$), resulting in triangles of unequal side lengths. I hypothesize that the shifted structure is a result of strain accommodation within the precipitate itself. In the future, quantification of the stability of the distorted structure in terms of strain energy may be determined using a combination of HAADF-STEM analysis and DFT computation.
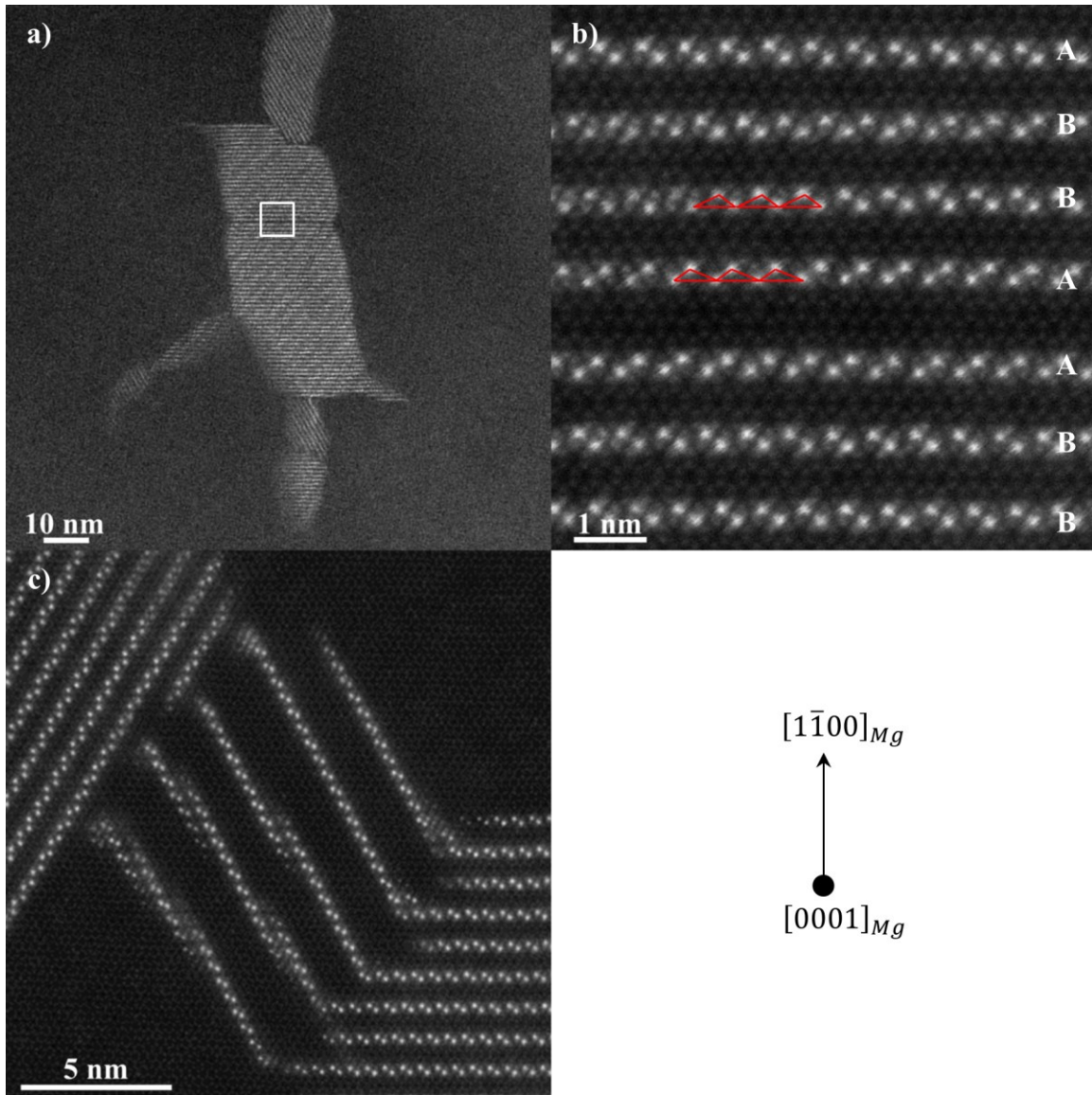
Figure 52: a)-c) HAADF-STEM images of the Mg-2.16 at. % Y alloy aged for 5000 hours at 200 ^{o}C showing the atomic structure of b) the β' phase and c) the strands. b) is a high magnification image of the region enclose in the white box in a). The incident beam is parallel to the [0001]$_{Mg}$ zone axis.

7.4 Evolution and coarsening of β' in Mg-Y alloys

It was shown in Chapter 4 that β' precipitates form a unique microstructure with their arrangement into a cellular network of connected precipitates, driven by elastic strain minimization. Further analysis of the microstructure at longer aging times in addition to phase field modeling of the precipitate evolution are necessary to confirm this hypothesis and to

identify whether the β' precipitates eventually coarsen, dissolve into the matrix, or transform to another phase. In addition, I hypothesize that this cell structure is presumably associated with an increased hardness (**Figure 27**).

In addition to the cell structures in Mg-Y alloys, other Mg-RE alloys have been shown to form connected networks of precipitates [11, 14, 17, 102, 103]. All of these networks have been characterized in two dimensions, leaving to question how these phases interact and behave in 3D. There are several techniques that would allow the 3D structure to be quantified experimentally; however there are limitations on how much detail can be acquired due to the size of the individual precipitates. X-ray tomography can be used to visualize how the chains connect and to quantify the cell size, while 3D tomography using a combination of STEM and APT would provide high resolution information about how the individual precipitates are connected. Further simulating these 3D structures using phase field computation would provide a complete quantitative analysis of the cell structure behavior.

7.5 Quantifying the strengthening behavior of precipitates

Previous studies claimed that the β_1 phase is the strengthening phase in WE alloys [10, 73], yet how this phase forms and evolves with aging is not understood, which limits our ability to control its formation in the microstructure. In addition, there is a lack of experimental work quantifying the strengthening behavior of the precipitate microstructure in Mg-RE alloys. The current study identified the strengthening mechanisms of the β''' and β' phases in Mg-Nd and Mg-Y alloys, while the strengthening mechanism of β_1 has not been shown experimentally. Therefore, there is an opportunity to identify the precipitation and strengthening mechanism of

the β_1 phase, which would allow further quantification of the overall strengthening behavior of Mg-RE alloys.

APPENDICES

APPENDIX I:

Effect of stress on the orientation of β''' in Mg-Nd

I.1 Background

Mg-RE alloys have excellent creep properties [104-106] due to the formation of precipitates with habit planes lying parallel to the prismatic planes; however most of the studies on precipitation in these alloys have focused on aging without applying an external stress. Only a few recent reports on Mg-Nd [36] and Mg-Gd [107, 108] alloys have examined precipitation during creep. Microstructural examination using HAADF-STEM and phase field models after creep of Mg-Gd-Zr alloys showed that the chains of β''' and β' precipitates align perpendicular to the tensile stress axis [107, 108], which was rationalized in terms of the minimization of the strain field generated by the applied stress and dislocations. This type of defect-assisted nucleation was also observed in Mg-Nd alloys where β_1 plates formed at dislocations with orientations aligned preferentially along a specific $\{1\bar{1}00\}_{Mg}$-type plane [36]. They also reported accelerated formation of the β' phase during creep, yet they did not specify whether a certain β' formed preferentially and it is difficult to discern this alignment from their images. To answer this question, this work investigates the effect of stress on the formation of β''' in Mg-Nd alloys by analyzing the microstructure of a Mg-0.4 at. % Nd alloy after creep testing.

I.2 Experimental

The alloy examined in this work was provided by Magnesium Elektron North America Inc. The composition was measured by inductively coupled plasma mass spectrometry and found to be Mg-2.35 wt. % Nd (Mg-0.40 at. % Nd). The cast alloy was encapsulated in quartz tubes in an argon atmosphere and solution treated at 560 $^{\circ}$C for 24 hours followed by water quenching. Rectangular-shaped samples with dimensions 4x4x8 mm were prepared from the solution treated material by electrical discharge machining (EDM). Compression tests using a SATEC testing machine were performed with an applied stress of 20 MPa at 250 $^{\circ}$C for 2 hours followed by water quenching. The crept sample was mounted and ground/polished to mirror finish then etched using a solution of 50 mL methanol, 6 mL hydrochloric acid, and 4 mL nitric acid. Electron backscatter diffraction was used to select a grain oriented such that one of the $\langle 11\bar{2}0 \rangle_{Mg}$ directions was parallel to the compression axis. A TEM sample from this grain was prepared using a liftout method and focused-ion beam (FIB) milling. STEM images were taken using a JEOL 3100R05 microscope operated at 300 kV with a collection angle of 74 mrad.

I.3 Results

When aged at 250 $^{\circ}$C for 2 hours with no applied stress the microstructure contains β''' and β_1 precipitates (**Figure 11d**). The β''' phase forms as plates elongated along $\langle 1\bar{1}00 \rangle_{Mg}$ directions and has a primitive orthorhombic crystal structure that is coherent with the matrix, as discussed in Chapter 3. Three variants of the β''' are observed, as shown in **Figure 11d**. The β_1 phase has a platelet morphology and habit plane lying parallel to the $\{1\bar{1}00\}_{Mg}$ planes (see Chapter 2).
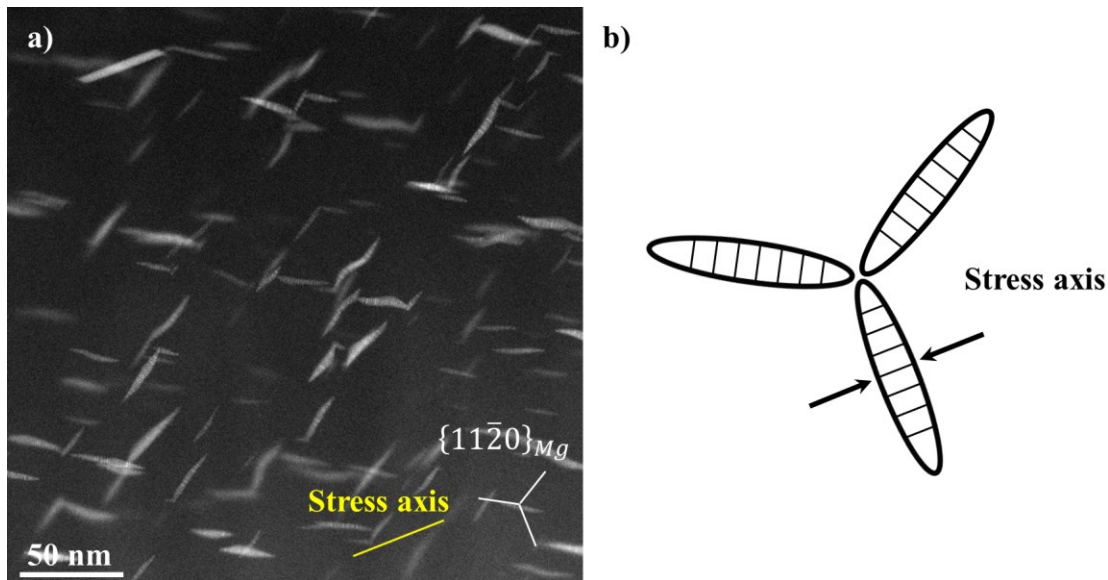
Figure 53: a) HAADF-STEM image of the Mg-0.40 at. % Nd alloy aged for 2 hours at 250 °C while being compressed along the direction labeled in yellow. Crystallographic planes are labeled in white. b) Schematic showing the orientation of the β''' precipitates with respect to the applied stress

The microstructure after creep testing at 250 °C for 2 hours is presented in **Figure 53a**. Only two β''' variants are identified in the microstructure. Aside from a few small β''' precipitates of the third variant, the formation of the third variant appears to have been suppressed. The thickness dimension ($\langle 11\bar{2}0 \rangle_{Mg}$) of the third variant is oriented parallel to the compression axis.

I.4 Discussion

The aging behavior of a Mg-Nd alloy under an applied stress is similar to previously studied Mg-Gd-Zr alloys. Both alloys form microstructures containing β''' variants whose misfit strain acts to minimize the strain energy introduced by the external stress. The formation of a β''' variant depends on the magnitude and orientation of the external stress with respect to the thickness dimension ($\langle 11\bar{2}0 \rangle_{Mg}$) of the β''' platelets.

Previous misfit calculations report the misfit strain to be highest along $\langle 11\bar{2}0 \rangle_{Mg}$-type directions and lowest along $\langle 1\bar{1}00 \rangle_{Mg}$-type and $[0001]_{Mg}$ directions. The third variant in **Figure 53a** is oriented such that the compression axis impinges on the thickness dimension ($\langle 11\bar{2}0 \rangle_{Mg}$) of the third variant β''' platelets, as shown schematically in **Figure 53b**. It seems that the external stress prevents the third variant β''' from forming by straining the matrix in the opposite direction as the misfit strain along the thickness of the third variant precipitates. Therefore, the external stress increases the misfit strain needed in order to form the third variant. This is consistent with previous studies on Mg-Gd-Zr alloys that showed microstructures containing only β''' variants with $\{010\}_{\beta'''}$ zigzag chains oriented parallel to the stress axis after tensile creep [107, 108].

I.5 Conclusions

The microstructure of a Mg-0.40 at. % Nd alloy aged under a compressive stress was analyzed using HAADF-STEM. The formation of one of the β''' variants in Mg-Nd was suppressed. The applied stress introduced a lattice strain that is opposite in direction to the misfit strain needed to form the missing variant.

APPENDIX II:

EDS and APT spectra

The following figures include APT reconstructions and spectra obtained from EDS and APT from the Mg-Y-Nd and WE43 alloys examined in Chapter 6. The spectra are representative of all the samples analyzed in Chapter 6. The APT spectra from both alloys contain Mg and Y hydrides (**Figure 54** and **Figure 55**). Due to the difference in evaporation field between the matrix and precipitates, the hydrides tend to be associated with the precipitates, as illustrated in **Figure 56**. In addition to Y and Nd, WE43 also contains other rare earth elements such as Pr, Gd, Dy, and Er (**Figure 55**). The YK (at 14.932 keV) and NdL (at 5.225 keV) peaks in the EDS spectra were used for quantifying the Nd:Y ratio for the precipitates and matrix in the Mg-Y-Nd alloy.
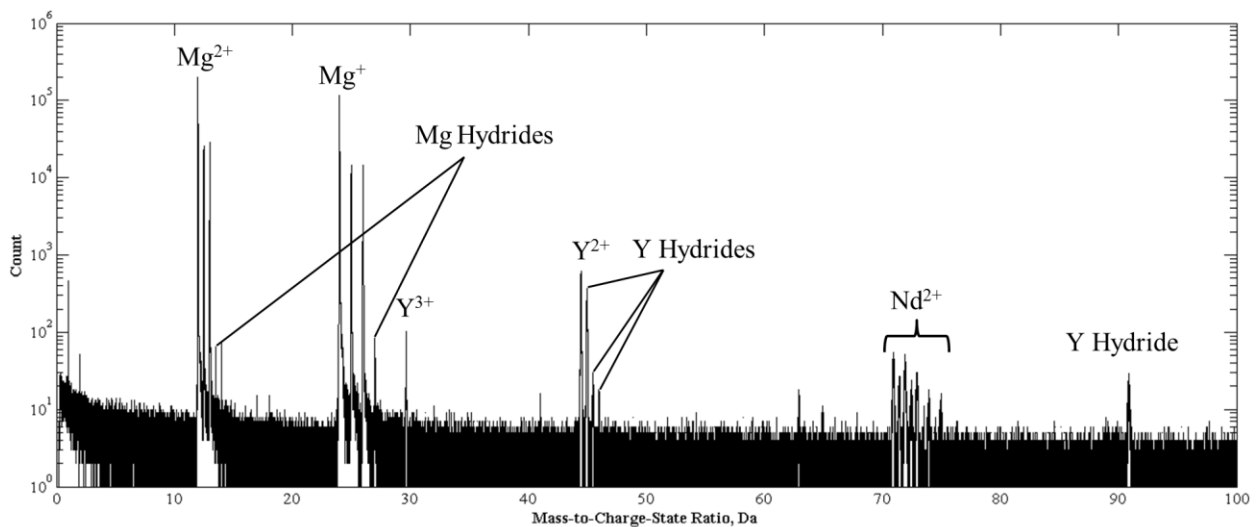
Figure 54: APT mass spectrum from the reconstructed data of the Mg-1.06Y-0.29Nd at. % alloy shown in Figure 41
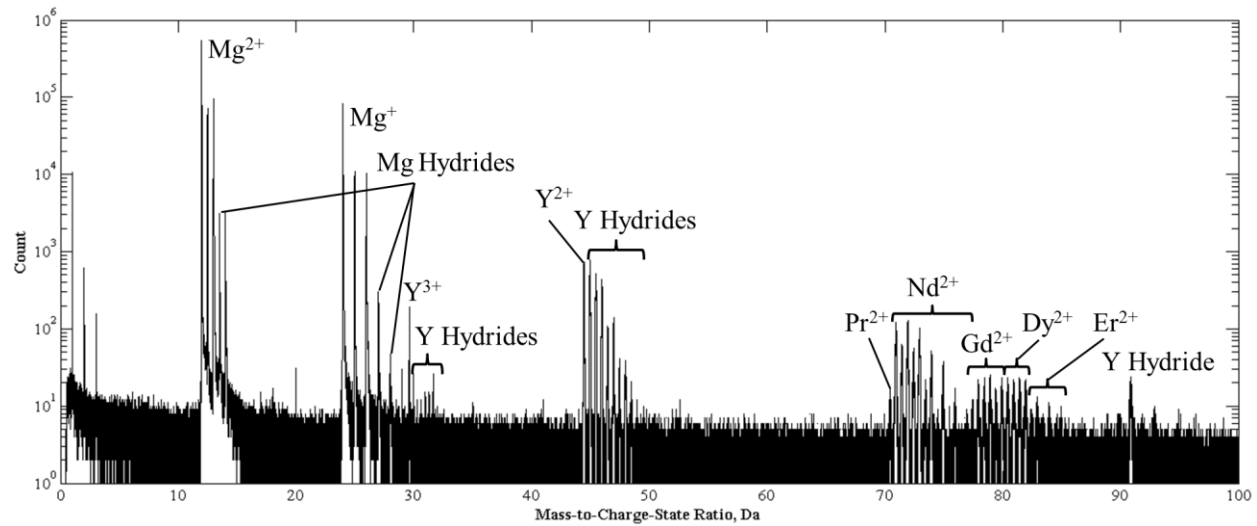
Figure 55: APT mass spectrum from a reconstructed dataset of the WE43 alloy
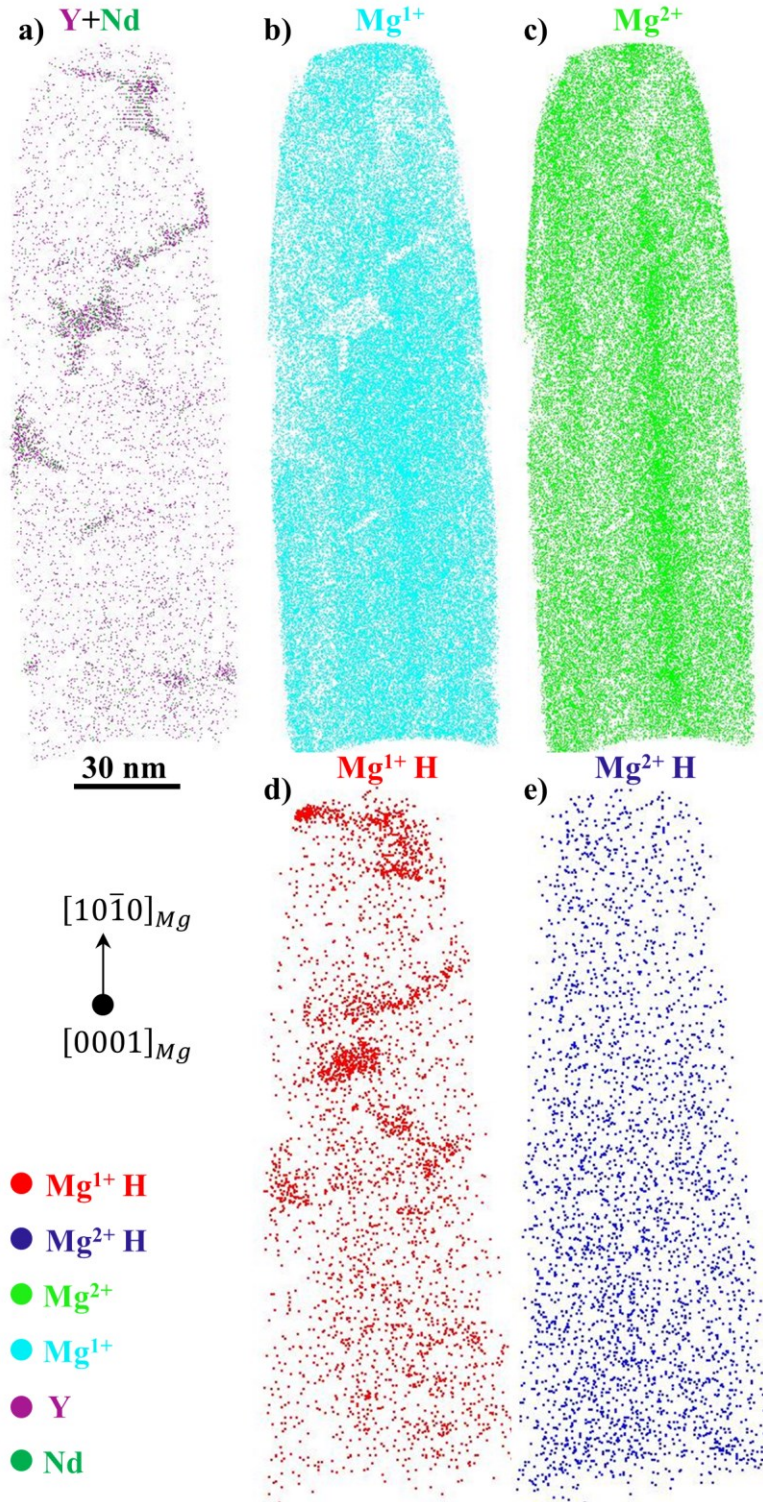
Figure 56: APT reconstructions showing the distribution of a) Y and Nd (showing 100% of Y and Nd), b) Mg^{1+} (showing 25% of ions), c) Mg^{2+} (showing 25% of ions), d) Mg^{1+} hydrides (showing 100% of ions), and e) Mg^{2+} hydrides (showing 100% of ions). a-c) are 3 nm thick slices of the same region (ion radius=1)and d-e) are showing the entire dataset (ion radius=2).

110
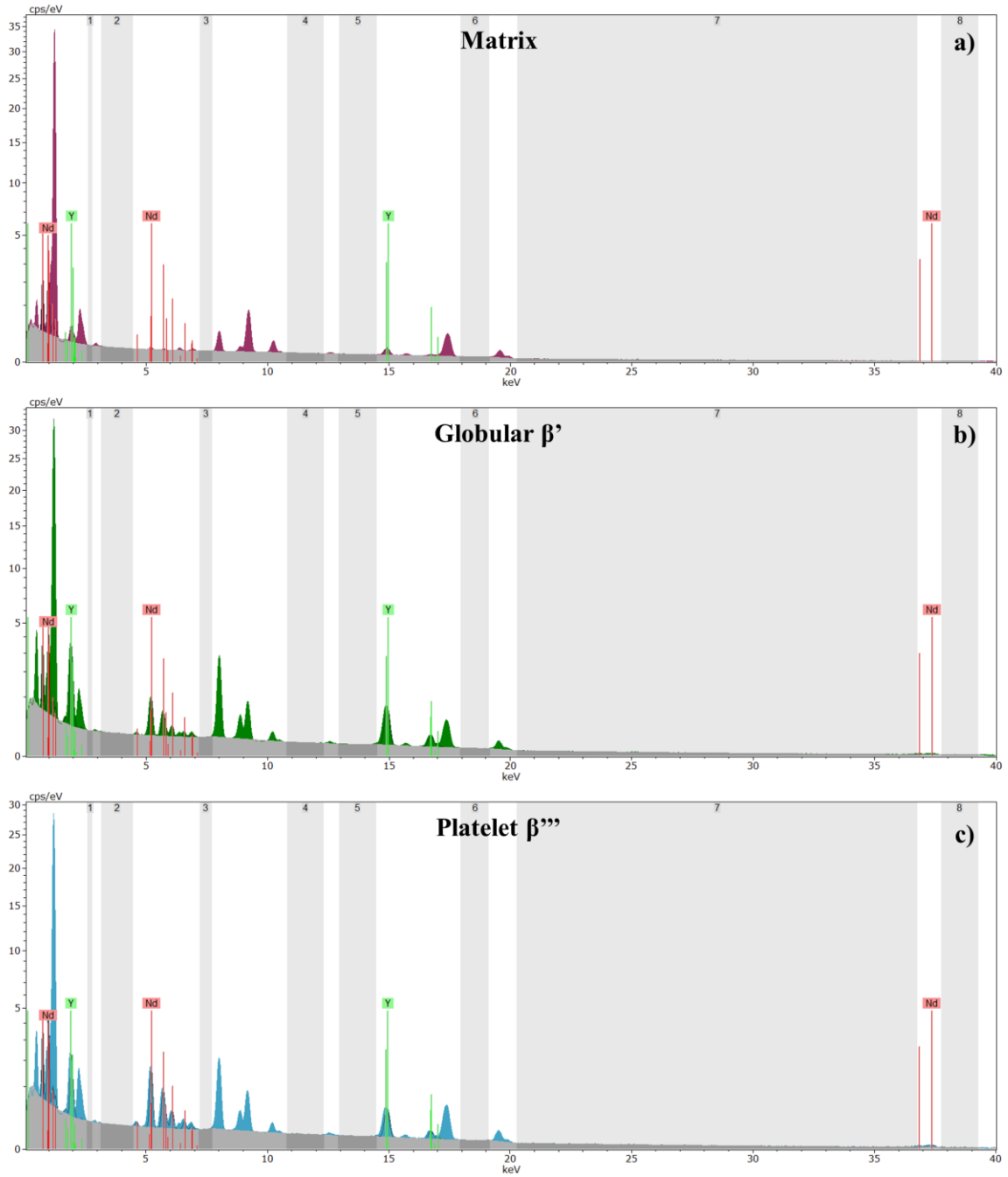
Figure 57: EDS spectra from all of the analyzed regions in the a) matrix, b) globular β', and c) platelet β'''

REFERENCES

[1] J.F. Nie, "Effects of precipitate shape and orientation on dispersion strengthening in magnesium alloys", *Scripta Materialia*, 48 (2003) 1009-1015.

[2] H. Karimzadeh, *PhD Thesis*, University of Manchester (1985).

[3] M. Ahmed, G.W. Lorimer, P. Lyon, R. Pilkington, "The effect of heat treatment and composition on the microstructure and properties of cast Mg-Y-RE alloys", *Proceedings of the International Conference on Magnesium Alloys and Their Applications*, (1992) 301-308.

[4] G. Lorimer, R. Azari-Khosroshahi, M. and Ahmed, "Precipitation reactions in two magnesium alloys containing rare earths", *Japan Institute of Metals Proceedings of the International Conference on Solid-Solid Phase Transformations*, 12 (1999) 185-192.

[5] J.F. Nie, B.C. and Muddle, "Precipitation in magnesium alloy WE54 during isothermal ageing at 250 ^{o}C", *Scripta Materialia*, 40 (1999) 1089-1094.

[6] J.F. Nie, B.C. Muddle, "Characterisation of strengthening precipitate phases in a Mg–Y–Nd alloy", *Acta Materialia*, 48 (2000) 1691-1703.

[7] C. Antion, P. Donnadieu, F. Perrard, A. Deschamps, C. Tassin, A. and Pisch, "Hardening precipitation in a Mg–4Y–3RE alloy", *Acta Materialia*, 51 (2003) 5335-5348.

[8] G. Riontino, D. Lussana, M. and Massazza, "A calorimetric study of phase evolution in a WE43 Mg alloy", *Journal of Thermal Analysis and Calorimetry,* 83 (2006) 643-647.

[9] D. Lussana, M. Massazza, G. Riontino, "A DSC study of precipitation hardening in a WE43 Mg alloy", *Journal of Thermal Analysis and Calorimetry*, 92 (2008) 223-225.

[10] P. Mengucci, G. Barucca, G. Riontino, D. Lussana, M. Massazza, R. Ferragut, E. Hassan Aly, "Structure evolution of a WE43 Mg alloy submitted to different thermal treatments", *Materials Science and Engineering A*, 479 (2008) 37-44.

[11] Z. Xu, M. Weyland, J.F. Nie, "On the strain accomodation of β_1 precipitates in magnesium alloy WE54", *Acta Materialia*, 75 (2014) 122-133.

[12] Z. Xu, M. Weyland, J.F. Nie, "Shear transformation of coupled β_1/β' precipitates in Mg-RE alloys: A quantitative study by aberration corrected STEM", *Acta Materialia*, 81 (2014) 58-70.

[13] Z. Xu, *PhD Thesis*, Monash University (2013).

[14] M. Nishijima, K. Hiraga, M. Yamasaki, Y. and Kawamura, "Characterization of β′ phase precipitates in an Mg-5 at%Gd alloy aged in a peak hardness condition, studied by high-angle annular detector dark-field scanning transmission electron microscopy", *Materials Transactions*, 47 (2006) 2109-2112.

[15] H. Liu, W.F. Xu, N.C. Wilson, L.M. Peng, J.F. Nie, "Formation of and interaction between β'$_F$ and β' phases in a Mg-Gd alloy", *Journal of Alloys and Compounds*, 712 (2017) 334-344.

[16] K. Saito, A. Yasuhara, M. Nishijima, K. Hiraga, "Structural changes of precipitates by aging of an Mg-4 at%Dy solid solution studied by atomic-scaled transmission electron microscopy", *Materials Transactions*, 52 (2011) 1009-1015.

[17] M. Nishijima, K. Hiraga, M. Yamasaki, Y. Kawamura, "Characterization of precipitates in Mg-Sm alloy aged at 200 ^{o}C, studied by high-resolution transmission electron microscopy and high-angle annular detector dark-field scanning transmission electron microscopy", *Materials Transactions*, 50 (2009) 1747-1752.

[18] B. Li, J. Dong, Z. Zhang, J.F. Nie, L. Bourgeois, L. Peng, "On the strengthening precipitate phases and phase transformation of β"/β' in a Mg-Sm-Zr alloy", *Materials and Design*, 116 (2017) 419-426.

[19] S. Gorsse, C.R. Hutchinson, B. Chevalier, J.F. Nie, "A thermodynamic assessment of the Mg–Nd binary system using random solution and associate models for the liquid phase", *Journal of Alloys and Compounds*, 392 (2005) 253-262.

[20] T.J. Pike, B. Noble, "The formation and structure of precipitates in a dilute magnesium-neodymium alloy", *Journal of Less-Common Metals*, 30 (1973) 63-74.

[21] M. Hisa, J.C. Barry, G.L. Dunlop, "New type of precipitate in Mg-rare-earth alloys", *Philosophical Magazine A*, 82 (2002) 497-510.

[22] K. Saito, K. and Hiraga, "The structures of precipitates in an Mg-0.5 at%Nd age-hardened alloy studied by HAADF-STEM technique", *Materials Transactions*, 52 (2011) 1860-1867.

[23] J.O. Andersson, T. Helander, L. Hoglund, P.F. Shi, B. Sundman, "Thermo-calc and DICTRA, computational tools for materials science", *CALPHAD*, 26 (2002) 273-312.

[24] J.F. Nie, N.C. Wilson, Y.M. Zhu, Z. Xu, "Solute clusters and GP zones in binary Mg-RE alloys", *Acta Materialia*, 106 (2016) 260-271.

[25] K. Momma, F. Izumi, "VESTA 3 for three-dimensional visualization of crystal, volumetric and morphology data", *Journal of Applied Crystallography*, 44 (2011).

[26] W. Lefebvre, V. Kopp, C. Pareige, "Nano-precipitates made of atomic pillars revealed by single atom detection in a Mg-Nd alloy", *Applied Physics Letters*, 100 (2012) 1-5.

[27] H. Liu, Y.M. Zhu, N.C. Wilson, J.F. Nie, "On the structure and role of β'$_F$ in β$_1$ precipitation in Mg-Nd alloys", *Acta Materialia*, 133 (2017) 408-426.

[28] Y.Z. Ji, A. Issa, T.W. Heo, J.E. Saal, C. Wolverton, L.-Q. Chen, "Predicting β' precipitate morphology and evolution in Mg-RE alloys using a combination of first-principles calculations and phase-field modeling", *Acta Materialia*, 76 (2014) 259-271.

[29] Y.M. Zhu, H. Liu, Z. Xu, Y. Wang, J.F. Nie, "Linear-chain configuration of precipitates in Mg-Nd alloys", *Acta Materialia*, 83 (2015) 239-247.

[30] V.I. Evdokimenko, P.I. Kripyakevich, "The crystal structures of magnesium-rich compounds in the systems La-Mg, Ce-Mg and Nd-Mg", *Crystallography*, 8 (1963) 135-141.

[31] K.J. Gradwell, *PhD Thesis*, The University of Manchester (1972).

[32] L.Y. Wei, G.L. Dunlop, H. Westengen, "Age hardening and precipitation in a cast magnesium rare-earth alloy", *Journal of Materials Science*, 31 (1996) 387-397.

[33] S. Delfino, A. Saccone, R. Ferro, "Phase relationships in the neodymium-magnesium alloy system", *Metallurgical Transactions A*, 21 (1990) 2109-2114.

[34] M.A. Easton, M.A. Gibson, D. Qiu, S.M. Zhu, J. Grobner, R. Schmid-Fetzer, J.F. Nie, M.X. Zhang, "The role of crystallography and thermodynamics on phase selection in binary magnesium-rare earth (Ce or Nd) alloys", *Acta Materialia*, 60 (2012) 4420-4430.

[35] R. Wilson, C.J. Bettles, B.C. Muddle, J.F. Nie, "Precipitation hardening in Mg-3 wt%Nd(-Zn) casting alloys", *Materials Science Forum*, 419-422 (2003) 267-272.

[36] D. Choudhuri, N. Dendge, S. Nag, M.A. Gibson, R. Banerjee, "Role of applied uniaxial stress during creep testing on precipitation in Mg-Nd alloys", *Materials Science and Engineering A*, 612 (2014) 140-152.

[37] Y.I. Bourezg, H. Azzeddine, L. Hennet, D. Thiaudiere, Y. Huang, D. Bradai, T. Langdon, "The sequence and kinetics of pre-precipitation in Mg-Nd alloys after HPT processing: A synchrotron and DSC study", *Journal of Alloys and Compounds*, 719 (2017) 236-241.

[38] Q. Ran, H.L. Lukas, G. Effenberg, G. Petzow, "Thermodynamic optimization of the Mg-Y system", *CALPHAD*, 12 (1988) 375-381.

[39] H. Okamoto, "Mg-Y", *Journal of Phase Equilibria*, 13 (1992) 105-106.

[40] H. Okamoto, "Mg-Y", *Journal of Phase Equilibria and Diffusion*, 27 (2006) 431.

[41] H. Okamoto, "Mg-Y (Magnesium-Yttrium)", *Journal of Phase Equilibria and Diffusion*, 31 (2010) 199.

[42] O.B. Fabrichnaya, H.L. Lukas, G. Effenberg, F. Aldinger, "Thermodynamic optimization in the Mg-Y system", *Intermetallics*, 11 (2003) 1183-1188.

[43] J.F. Smith, D.M. Bailey, D.B. Novotny, J.E. Davison, "Thermodynamics of formation of yttrium-magnesium intermediate phases", *Acta Metallurgica*, 13 (1965) 889-895.

[44] M.X. Zhang, P.M. Kelly, "Morphology and crystallography of $Mg_{24}Y_5$ precipitate in Mg-Y alloy", *Scripta Materialia*, 48 (2003) 379-384.

[45] M. Nishijima, K. Yubuta, K. and Hiraga, "Characterization of β′ precipitate phase in Mg-2 at%Y alloy aged to peak hardness condition by high-angle annular detector dark-field scanning transmission electron microscopy (HAADF-STEM)", *Materials Transactions*, 48 (2007) 84-87.

[46] H. Liu, Y. Gao, J.Z. Liu, Y.M. Zhu, Y. Wang, J.F. Nie, "A simulation study of the shape of β' precipitates in Mg-Y and Mg-Gd alloys", *Acta Materialia*, 61 (2013) 453-466.

[47] K. Matsubara, H. Kimizuka, S. Ogata, "Long-range intercluster interactions of solute nanoprecipitates in Mg-Y alloys: A first-principles study", *Journal of Alloys and Compounds*, 657 (2016) 662-670.

[48] J.F. Nie, "Precipitation and hardening in magnesium alloys", *Metallurgical and Materials Transactions A*, 43A (2012) 3891-3939.

[49] T. Sato, I. Takahashi, H. Tezuka, A. Kamio, "Precipitation Structures of Mg-Y Alloys", *Journal of Japan Institute of Light Metals*, 42 (1992) 804-809.

[50] S. Sandlobes, M. Friak, S. Zaefferer, A. Dick, S. Yi, D. Letzig, Z. Pei, L.-F. Zhu, J. Neugebauer, D. Raabe, "The relation between ductility and stacking fault energies in Mg and Mg-Y alloys", *Acta Materialia*, 60 (2012) 3011-3021.

[51] M. Suzuki, T. Kimura, J. Koike, K. Maruyama, "Strengthening effect of Zn in heat resistant Mg-Y-Zn solid solution alloys", *Scripta Materialia*, 48 (2003) 997-1002.

[52] S. Sandlobes, S. Zaefferer, I. Schestakow, S. Yi, R. Gonzalez-Martinez, "On the role of non-basal deformation mechanisms for the ductility of Mg and Mg-Y alloys", *Acta Materialia*, 59 (2011) 429-439.

[53] M.H. Yoo, "Slip, twinning, and fracture in hexagonal close-packed metals", *Metallurgical Transactions A*, 12A (1981) 409-418.

[54] R. von Mises, *Z. Angew. Math. Mech.*, 6 (1928) 161-185.

[55] G.W. Groves, A. Kelly, "Independent slip systems in crystals", *Philosophical Magazine*, 8 (1963) 877-887.

[56] F.G. Meng, J. Wang, L.B. Liu, H.S. Liu, Z.P. Jin, "Experimental investigation and thermodynamic calculation of phase relations in the Mg–Nd–Y ternary system", *Materials Science and Engineering A*, 454-455 (2007) 266-273.

[57] R. Azari-Khosroshahi, *PhD Thesis*, Manchester University (1997).

[58] P.J. Apps, H. Karimzadeh, J.F. King, G.W. Lorimer, "Precipitation reactions in magnesium-rare earth alloys containing yttrium, gadolinium or dysprosium", *Scripta Materialia*, 48 (2003) 1023-1028.

[59] G.W. Lorimer, "Structure-property relationships in cast magnesium alloys", *Proceedings of London Conference, The Institute of Metals, Magnesium Techonology*, (1987) 47-53.

[60] D. Choudhuri, S. Meher, S. Nag, N. Dendge, J.Y. Hwang, R. and Banerjee, "Evolution of a honeycomb network of precipitates in a hot-rolled commercial Mg-Y-Nd-Zr alloy", *Philosophical Magazine Letters*, 93 (2013) 395-404.

[61] M. Zhang, W.Z. Zhang, "Interpretation of the orientation relationship and habit plane orientation of the equilibrium β-phase in an Mg-Y-Nd alloy", *Scripta Materialia*, 59 (2008) 706-709.

[62] M. Vlach, B. Smola, H. Cisarova, I. Stulíková, "Precipitation Processes in Mg-Y-Nd Alloys", *Defect and Diffusion Forum*, 334-335 (2013) 155-160.

[63] S. Kandalam, P. Agrawal, G.S. Avadhani, A. Kumar, S. Suwas, "Precipitation response of the magnesium alloy WE43 in strained and unstrained conditions", *Journal of Alloys and Compounds*, 623 (2015) 317-323.

[64] J.D. Robson, N. Stanford, M.R. Barnett, "Effect of precipitate shape on slip and twinning in magnesium alloys", *Acta Materialia*, 59 (2011) 1945-1956.

[65] F. Wang, J.J. Bhattacharyya, S.R. Agnew, "Effect of precipitate shape and orientation on Orowan strengthening of non-basal slip modes in hexagonal crystals, application to magnesium alloys", *Materials Science and Engineering A*, 666 (2016) 114-122.

[66] A.R. Natarajan, E.L.S. Solomon, B. Puchala, E.A. Marquis, A. Van der Ven, "On the early stages of precipitation in dilute Mg-Nd alloys", *Acta Materialia*, 108 (2016) 367-379.

[67] T.T. Tsong, "Field ion image formation", *Surface Science*, 70 (1978) p. 211.

[68] V.J. Araullo-Peters, A. Breen, A.V. Ceguerra, B. Gault, S.P. Ringer, J.M. Cairney, "A new systematic framework for crystallographic analysis of atom probe data", *Ultramicroscopy*, 154 (2015) 7-14.

[69] E.L.S. Solomon, E.A. Marquis, "The structure of β" and β' in an aged Mg-Nd alloy", *Magnesium Technology, TMS*, (2016).

[70] E.L.S. Solomon, T. Chan, A. Chen, B. Uttal-Veroff, E.A. Marquis, "Aging behavior of Mg alloys containing Nd and Y", *Magnesium Technology, TMS*, (2017).

[71] S. DeWitt, E.L.S. Solomon, A.R. Natarajan, V. Araullo-Peters, S. Rudraraju, L. Aagesen, B. Puchala, E.A. Marquis, A. Van der Ven, K. Thornton, J.E. Allison, "Misfit-driven β''' precipitate composition and morphology in Mg-Nd alloys", *Acta Materialia*, 136 (2017) 378-389.

[72] E.L.S. Solomon, V.J. Araullo-Peters, J.E. Allison, E.A. Marquis, "Early precipitate morphologies in Mg-Nd-(Zr) alloys", *Scripta Materialia*, 128 (2017) 14-17.

[73] J.F. Nie, "Precipitation and strengthening in selected magnesium alloys", *Magnesium Technology, TMS*, (2002).

[74] L. Gao, R.S. Chen, E.H. Han, "Solid solution strengthening behaviors in binary Mg-Y single phase alloys", *Journal of Alloys and Compounds*, 472 (2009) 234-240.

[75] A.R. Natarajan, A. Van der Ven, "A unified description of ordering in HCP Mg-RE alloys", *Acta Materialia*, 124 (2017) 620-632.

[76] C.A. Schneider, W.S. Rasband, K.W. Eliceiri, "NIH Image to ImageJ: 25 years of image analysis", *Nature Methods*, 9 (2012) 671-675.

[77] Comsol, in, COMSOL Multiphyics: Version 5.2a, 2016.

[78] "ASTM E112-13 Standard Test Methods for Determining Average Grain Size", *ASTM E112-13 Standard Test Methods for Determining Average Grain Size, ASTM International, West Conshohocken, PA, (2013) https://doi.org/10.1520/E0112*.

[79] Y. Wang, A. Khachaturyan, "Microstructural evolution during the precipitation of ordered intermetallics in multiparticle coherent systems", *Philosophical Magazine A*, 72 (1995) 1161-1171.

[80] Y. Wang, A.G. Khachaturyan, "Shape instability during precipitate growth in coherent solids", *Acta Metallurgica et Materialia*, 43 (1995) 1837-1857.

[81] H. Liu, Y. Gao, J.Z. Liu, Y.M. Zhu, Y. Wang, J.F. Nie, "A simulation study of the shape of β' precipitates in Mg-Y and Mg-Gd alloys", *Acta Materialia*, 61 (2013) 453-466.

[82] D. Mizer, B.C. Peters, "A study of precipitation at elevated temperatures in a Mg-8.7 pct Y alloy", *Metallurgical Transactions*, 3 (1972) 3262-3264.

[83] S.R. Agnew, M.H. Yoo, C.N. Tome, "Application of texture simulation to understanding mechanical behavior of Mg and solid solution alloys containing Li or Y", *Acta Materialia*, 49 (2001) 4277-4289.

[84] M. Nishijima, K. Hiraga, "Structural changes of precipitates in an Mg-5 at%Gd alloy studied by transmission electron microscopy", *Materials Transactions*, 48 (2007) 10-15.

[85] M.K. Miller, M.G. Hetherington, "Local magnifcation effects in the atom probe", *Surface Science*, 246 (1991) 442-449.

[86] E.A. Marquis, F. Vurpillot, "Chromatic Abberations in the Field Evaporation Behavior of Small Precipitates", *Microscopy and Microanalysis*, 14 (2008) 561-570.

[87] F. Vurpillot, A. Bostel, D. Blavette, "Trajectory overlaps and local magnification in three-dimensional atom probe", *Applied Physics Letters*, 76 (2000) 3127-3129.

[88] F. Vurpillot, A. Bostel, A. Menand, D. Blavette, "Trajectories of field emitted ions in 3D atom-probe", *The European Physical Journal Applied Physics*, 6 (1999) 217-221.

[89] B.C. Zhou, S.L. Shang, Y. Wang, Z.K. Liu, "Diffusion coefficients of alloying elements in dilute Mg alloys: A comprehensive first-principles study", *Acta Materialia*, 103 (2016) 573-586.

[90] L. Huber, I. Elfimov, J. Rottler, M. Militzer, "Ab initio calculations of rare-earth diffusion in magnesium", *Physical Review B*, 85 (2012) 1-7.

[91] G. Teichert, *PhD Thesis*, University of Michigan (2017).

[92] J.F. Nie, B.C. Muddle, "Precipitation hardening of Mg-Ca(-Zn) alloys", *Scripta Materialia*, 37 (1997) 1475-1481.

[93] T. Bhattacharjee, C.L. Mendis, K. Oh-ishi, T. Ohkubo, K. Hono, "The effect of Ag and Ca additions on the age hardening response of Mg-Zn alloys", *Materials Science and Engineering A*, 575 (2013) 231-240.

[94] T.T. Sasaki, K. Oh-ishi, T. Ohkubo, K. Hono, "Enhanced age hardening response by the addition of Zn in Mg-Sn alloys", *Scripta Materialia*, 55 (2006) 251-254.

[95] C.L. Mendis, C.J. Bettles, M.A. Gibson, S. Gorsse, C.R. Hutchinson, "Refinement of precipitate distributions in an age-hardenable Mg-Sn alloy through microalloying", *Philosophical Magazine Letters*, 86 (2006) 443-456.

[96] X. Gao, J.F. Nie, "Characterization of strengthening precipitate phases in a Mg-Zn alloy", *Scripta Materialia*, 56 (2007) 645-648.

[97] J.R. Cahoon, W.H. Broughton, A.R. Kutzak, "The determination of yield strength from hardness measurements", *Metallurgical Transactions*, 2 (1971) 1979-1983.

[98] Y.M. Zhu, A.J. Morton, M. Weyland, J.F. Nie, "Characterization of planar features in Mg-Y-Zn alloys", *Acta Materialia*, 58 (2010) 464-475.

[99] J.F. Nie, K. Oh-ishi, X. Gao, K. Hono, "Solute segregation and precipitation in a creep-resistant Mg–Gd–Zn alloy", *Acta Materialia*, 56 (2008) 6061-6076.

[100] M. Nishijima, K. Hiraga, M. Yamasaki, Y. Kawamura, "The structure of Guinier-Preston zones in an Mg-2 at%Gd-1 at%Zn alloy studied by transmission electron microscopy", *Materials Transactions*, 49 (2008) 227-229.

[101] K. Saito, A. Yasuhara, K. Hiraga, "Microstructural changes of Guinier–Preston zones in an Mg–1.5 at% Gd–1 at% Zn alloy studied by HAADF-STEM technique", *Journal of Alloys and Compounds*, 509 (2011) 2031-2038.

[102] X. Gao, S.M. He, X.Q. Zeng, L.M. Peng, W.J. Ding, J.F. Nie, "Microstructure evolution in a Mg-15Gd-0.5Zr (wt. %) alloy during isothermal aging at 250 ^{o}C", *Materials Science and Engineering A*, 431 (2006) 322-327.

[103] K.Y. Zheng, J. Dong, X.Q. Zeng, W.J. Ding, "Precipitation and its effect on the mechanical properties of a cast Mg–Gd–Nd–Zr alloy", *Materials Science and Engineering A*, 489 (2008) 44-54.

[104] B.L. Mordike, "Creep-Resistant Magnesium Alloys", *Materials Science and Engineering A*, 324 (2002) 103-112.

[105] B.L. Mordike, T. Ebert, "Magnesium: Properties-applications-potential", *Materials Science and Engineering A*, 302 (2001) 37-45.

[106] K. Maruyama, M. Suzuki, H. Sato, "Creep strength of magnesium-based alloys", *Metallurgical and Materials Transactions A*, 33A (2002) 875-882.

[107] H. Liu, W.F. Xu, L.M. Peng, W.J. Ding, J.F. Nie, "A simulation study of the distribution of β' precipitates in a crept Mg-Gd-Zr alloy", *Computational Materials Science*, 130 (2017) 152-164.

[108] W.F. Xu, Y. Zhang, L.M. Peng, W.J. Ding, J.F. Nie, "Linear precipitate chains in Mg-2.4Gd-0.1Zr alloy after creep", *Materials Letters*, 137 (2014) 417-420.